6-30-2017

Artificial Antennas: Thermodynamics of Protein-DNA, Protein-Solid, and Protein-Dye Interactions for Light Harvesting Applications

Clive Baveghems
University of Connecticut, clive.baveghems@uconn.edu

Artificial Antennas: Thermodynamics of Protein-DNA, Protein-Solid, and Protein-Dye Interactions for Light Harvesting Applications

Clive Leon Baveghems

University of Connecticut, 2017

Abstract

The thermodynamics of protein-DNA and protein-solid interactions have been investigated here. Protein-DNA interactions play fundamental roles in biological systems and disease. Therefore, studies that help explain the mechanisms of these interactions will contribute to the development of much needed drug therapies. Protein-solid interactions have been optimized for applications in drug delivery and biomedical devices. Additionally, protein-DNA and protein-solid interactions have been optimized as matrices for artificial light harvesting antennas with the goal of utilizing sunlight for energy conversion. In this thesis, glucose oxidase/DNA (GOx/DNA) was used as a model system to study the role of protein surface charge in the thermodynamics of protein-DNA interactions. Synthesis of differentially charged GOx analogs facilitated control of its net charge and revealed a protein/DNA switching mechanism where binding is switched on at a GOx charge of +30. Another goal of this thesis was to study the contribution of protein surface charge to the thermodynamics of protein/solid interactions using a GOx/zirconium phosphate (GOx/α-ZrP) model system. Negatively charged GOx analogs associated weakly with α-ZrP but positively charged analogs associated with high affinity and there was a significant linear relationship between GOx net charge and GOx/α-ZrP binding affinity. In a third study, another protein, bovine serum albumin (BSA) was incorporated into a BSA/DNA matrix. A biodegradable BSA/DNA/dyes antenna that harvested light in the broad range from 350 nm to 590 nm was

synthesized by self-assembly. Cascade energy transfer that shuttled photons to a terminal acceptor emitting red light for the potential catalysis of solar cells was characterized.

Artificial Antennas: Thermodynamics of Protein-DNA, Protein-Solid, and Protein-Dye Interactions for Light Harvesting Applications

Clive Leon Baveghems

B.Sc., University of Maryland, College Park **[2002]**

A Dissertation

Submitted in Partial Fulfillment of the

Requirements for the Degree of

Doctor of Philosophy

at the

University of Connecticut

[2017]

APPROVAL PAGE

Doctor of Philosophy Dissertation

Artificial Antennas: Thermodynamics of Protein-DNA, Protein-Solid, and Protein-Dye Interactions for Light Harvesting Applications

Presented by
Clive Leon Baveghems, B.Sc.

Major Advisor

_____
Dr. Challa V. Kumar

Associate Advisor

_____
Dr. Rajeswari Kasi

Associate Advisor

_____
Dr. Alfredo Angeles-Boza

Associate Advisor

_____
Dr. Jayesh Bokria

Associate Advisor

_____
Dr. Joseph DePasquale

University of Connecticut
[2017]

Acknowledgement

I am thankful to my thesis advisor, Dr. Challa V. Kumar for his exceptional guidance and support throughout my graduate student career. His availability and ability to analyze problems are unmatchable. His grasp and thorough understanding of thermodynamics has been a real gift to me as I navigated the projects. I wish to thank Dr. Rajeswari Kasi for her explanation of problems and her ability to predict possible pitfalls. I would like to thank Dr. Alfredo Angeles-Boza for career guidance and taking the time to analyze specific situations and suggest the best way forward. Dr. Jayesh Bokria was very helpful in developing my knowledge of solar cells, photochemistry, and the job market. Dr. Joseph DePasquale has been my teaching advisor for four years and he has been instrumental in helping me improve my teaching skills.

I am grateful for all the support from lab members including Ajith and Omkar who kept the coffee club alive. I am grateful to lab members, Bobbi, Ananta, Cat, Kyle, Megan, Melissa, Jingwen, and our new addition Mansi for their collaborative efforts and support. To past lab members, Vindya and Inoka, I am indebted to them for the knowledge they passed on. I thank Murali for his excellent SPR analysis. I thank all undergraduates who have worked with me, especially Eric, Kevin, and Jill.

I am grateful to my wife, Mary, my son, Camden, my parents and siblings, and my wife's family for their unwavering support and I thank my Aunts Allison, Faye, and Minette who supported me financially during my undergraduate years.

Table of Contents

List of Schemes

List of Figures

Figure 2.11. Circular dichroism and activity of GOx(n)/α-ZrP. (A) The effect on structure retention due to GOx(n) complex formation with α-ZrP (GOx(n)/α-ZrP) was assessed over a range of GOx(n) charges from +20 to +65. There was no significnant loss in protein structure when compared to pristine GOx (blue curve). However, randomness in peak intensity was observed at the 220 nm minimum when compared to GOx (blue bar). GOx/α-ZrP (brown curve) and GOx(+65)/α-ZrP (green curve) showed comparable intensities, but GOx(+20)/α-ZrP (black curve), GOx(+45)/α-ZrP (red curve), and GOx(+60)/α-ZrP (orange curve) showed variably reduced intensities at the 220 minimum when compared to pristine GOx. (B) Plot of absorbance values showing activity of GOx(n) bound to α-ZrP. Unmodified GOx bound to α-ZrP (blue-gray line) showed initial activity comparable to unbound GOx and the initial activities of bound GOx(n) were comparable to the corresponding unbound GOx(n) although there was variable loss in activity when compared to unmodified GOx. Samples were analyzed in NaPIPES buffer at pH 7.0. A solution of D-glucose (4 μM) was added to a mixture of GOx (1 μM), horseradish peroxidase (HRP, 0.4 μM) in 10 mM NaPIPES buffer pH 7.2 and guaiacol (o-methoxyphenol) (800 μM) dissolved in DI water. Oxidation of the substrate, guaiacol to a dimeric product that has an

List of Tables

List of Abbreviations

GOx	Glucose oxidase
GOx-TETA or cGO	Cationized glucose oxidase
DNA	Deoxyribonucleic acid
α-ZrP	Layered zirconium phosphate
TBA	Tetrabutylammonium Hydoxide
UV/Vis	UV/Visible spectroscopy
SPR	Surface plasmon resonance
CD	Circular dichroism
ITC	Isothermal titration calorimetry
TEM	Transmission electron microscopy
SEM	Scanning electron microscopy
XRD	Xray diffraction
EDX	Energy-dispersive Xray spectroscopy
Hb	hemoglobin
Mb	myoglobin
Lys	lysozyme
HRP	Horseradish peroxidase
BSA	Bovine serum albumin
b-Lact	Beta lactoglobulin
oval	ovalbumin
PASC	Phosphoric acid swollen cellulose

CMC	carboxymethylcellulose
EDC	1-Ethyl-3-(3-dimethylaminopropyl) carbodiimide
TETA	triethylenetetramine
FRET	Förster Resonance Energy Transfer
ICPB	Ion coupled proton binding
FAD	Flavin adenine dinucleotide
H	Hoechst 33258
C	Coumarin 540a
F	Fluorescein
RhB	Rhodamine B

Chapter 1: Designer Histone Complexes: Controlling Protein-DNA Interactions With Protein Charge as 'All-Or-None' Digital Switch

1.1. Abstract

An artificial histone is synthesized which functions as a DNA-protein digital switch, where DNA binding is all or none, controlled by a sharp threshold of protein charge. A non-DNA binding protein, glucose oxidase (GOx), was chemically modified by attaching increasing numbers of triethylenetetramine (TETA) side chains to its glutamate/aspartate groups to obtain a small library of covalently modified GOx(n) derivatives. The n is the net charge on the protein at pH 7, which was increased from -62 (pristine GOx) to +75 by attaching increasing numbers of TETA residues to the protein. All GOx(n) derivatives retained their secondary structure to a good extent, as monitored by UV circular dichroism spectroscopy, and they also retained oxidase activities to a significant extent. The interaction of the GOx(n) with calf thymus DNA was examined by isothermal titration calorimetry. Pristine GOx of -62 charge at pH 7 in 10 mM TrisHCl, 50 mM NaCl buffer had no affinity for the negatively charged DNA helix and GOx(n) with $n < +30$ had no affinity for DNA either. However, binding has been turned on abruptly when $n \geq +30$ with binding constants (K_b) ranging from $(1.5 \pm 0.7) \times 10^7$ M^{-1} to $(7.3 \pm 2.8) \times 10^7$ M^{-1} for n values of +30 and +75 respectively, and this kind of 'all-or-none' binding based on protein charge is intriguing. Further thermodynamic analysis of the titration data revealed that binding is entirely entropy driven with ΔS ranging from 0.09 ± 0.007 kcal/mol.K to 0.19 ± 0.008 kcal/mol.K with enthalpic penalties of 17.0 ± 2.3 kcal/mol to 46.1 ± 2.1 kcal/mol, respectively. The binding had intrinsic propensities (ΔG) of -9.8 ± 0.14 kcal/mol to -10.7 ± 0.25 kcal/mol independent of n. DNA binding distorted protein/DNA secondary structure, as evidenced by circular dichroism spectroscopy, but oxidase activity of GOx(n)/DNA complexes has been

unaffected. This is the very first example of an artificial histone (GOx(n)) where the protein charge functioned as a DNA binding switch. Protein charge is in turn under complete chemical control while preserving the biological activity of the protein. The new insights gained here could be useful in the design of novel 'on-off' protein switches.

1.2. Introduction

Artificial histones are synthesized *in vitro* by chemical modification of an ordinary enzyme, glucose oxidase (GOx) to yield GOx(n) derivatives with increasing net charge, and DNA binding was switched on only when the net charge of GOx(n) exceeded +30. This is similar to the binding of the histone octamer to the DNA helix *in vivo* which is controlled by octamer charge, and charge in turn is controlled by protein acetylation-deacetylation. [1,2,3,4] Thermodynamic details that help explain the mechanism of DNA-protein interactions, in this context, including DNA looping/unwinding have been studied extensively[5,6] but a charge threshold for protein binding to DNA has not been hypothesized.[7]

The critical role of electrostatics and H-bonding at the DNA/protein interface has been well characterized.[8,9,10,11] In fact, DNA-binding sites on proteins are large patches of positive electrostatic potential[12] and electrostatic interactions drive interfacial dynamics.[13] Furthermore, the electrostatic component accounts for the majority of interfacial Gibbs free energy and is entropically driven.[14] Studying the role of histone octamer charge in DNA-octamer interaction revealed that one unit decrease in charge is associated with significant dissociation of DNA from the histone core, suggesting a meaningful role of electrostatic interactions in the binding event.[15] Previously, we reported the binding of moderately negatively charged hemoglobin, myoglobin and horseradish peroxidase (pH 7.2) to DNA[16] where the protein surface groups and cations

played a major role in DNA binding, even when electrostatic interactions are not favorable. Here, we show that these innate interactions can be chemically manipulated to construct a functional DNA binding switch.

We decided to test if protein charge variation by chemical manipulation can be used to control protein binding to DNA in a predictable manner. Our hypothesis is that binding free energy should be a continuous function of charge, and increase quadratically with positive charge on the protein. A non-DNA binding enzyme, GOx (charge of -62 at pH 7) [17,18] with no intrinsic affinity for DNA was chosen for these studies, and carboxyl groups of GOx were chemically modified with increasing numbers of triethylenetetramine (TETA) side chains via EDC chemistry[19] to obtain a small library of GOx-TETA derivatives with increasing positive charge (n) (**Scheme 1**). Binding of the resulting GOx(n) derivatives to DNA was analyzed as a function of n by isothermal titration calorimetry. The central hypothesis tested here is that strongly negatively charged proteins do not bind to DNA due to unfavorable electrostatic interactions but binding will turn on at a minimum positive charge on the protein, where the favorable electrostatic interactions replace unfavorable charge-charge repulsions. We tested this hypothesis by systematically increasing the net negative charge on GOx from -62 to +75, and this strategy provided a general, facile, predictable approach to

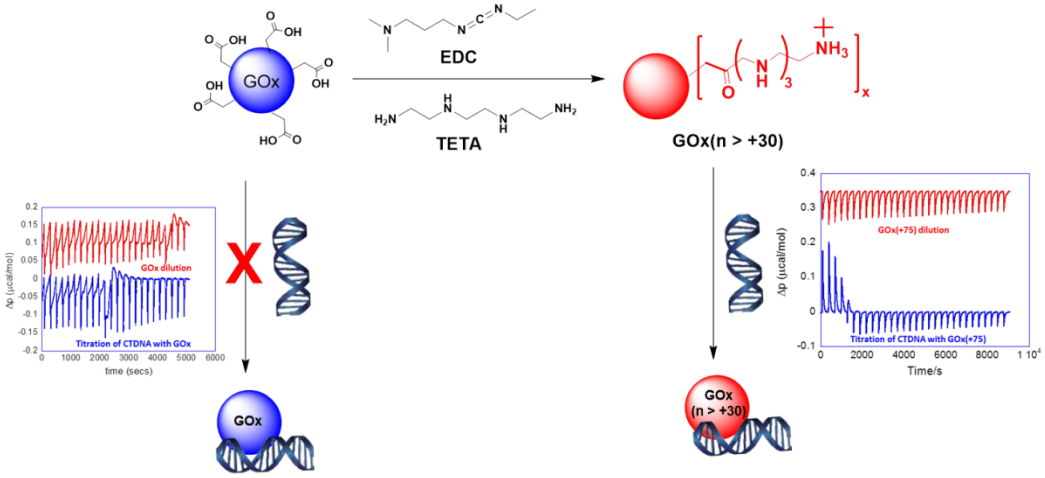

Scheme 1.1. Cationization of anionic GOx (blue sphere) with polyamines is predicted to promote it's binding to the anionic DNA helix when net charge on the protein is increased due to favorable charge-charge interactions. Carboxyl groups of GOx are activated by carbodiimide and reacted with increased loadings of TETA to continuously increase the net charge (n) on GOx(n). DNA binds to GOx(n) (red sphere) when n > +30 but DNA did not bind to unmodified GOx or GOx(n) when n < +30.

control DNA-protein interactions on a rational basis. This served as an alternative to traditional recombinant molecular biology approaches to modify protein charge and still control DNA binding. However, we found that DNA binding of the strongly anionic GOx required a minimum positive charge and below this threshold, there was essentially no binding.

1.3. Materials and Methods

Glucose oxidase (GOx, 60 000 MW) was purchased from Calzyme Laboratories, Inc. (Tulelake, CA). Calf thymus DNA (CTDNA), 1-ethyl-3-(3-dimethylaminopropyl)-carbodiimide hydrochloride (EDC), triethylenetetramine (TETA) were purchased from Sigma-Aldrich (St. Louis, MO). Solutions were prepared using 10 mM TrisHCl and 50 mM NaCl (pH 7).

1.3.1 ***Chemical modification of glucose oxidase***: Surface carboxyl groups on glucose oxidase were modified by activation with EDC and reaction with TETA by adopting reported methods.[20] GOx (10mg/mL) in deionized water (DI) was stirred with TETA (pH adjusted to 4 or 5) for an h followed by the addition of EDC (10 - 100 mM). The mixture was stirred for 4 h at room temperature and the unreacted EDC, TETA, and byproducts were removed by dialysis against TrisHCl. The degree of chemical modification was carefully controlled by adjusting TETA and EDC concentrations such that GOx(n) charge was varied gradually from net negative to net positive.

1.3.2. ***Agarose gel electrophoresis:*** Agarose gel electrophoresis was performed using a horizontal gel electrophoresis apparatus (Gibco model 200, Life Technologies Inc, MD) and agarose (0.5 % w/w) in Tris acetate (40 mM) buffer. Modified enzymes were loaded with 50% loading buffer (50% v/v glycerol and 0.01% w/w bromophenol blue). The running buffer used for all samples was Tris acetate (40 mM). Samples were spotted into wells placed at the middle of the gel so that GOx(n) could migrate to the negative or positive electrode based on its net

charge that was determined by the extent of modification, type of modification, and the pH of the running buffer. A voltage of 100 V was applied for 30 minutes. Gels were stained overnight with 10% v/v acetic acid, 0.02% w/w Coomassie blue, followed by destaining in 10 % v/v acetic acid overnight.

1.3.3. ***Mass Spectrometry:*** MALDI-TOF mass spectral analysis was done by Bruker Daltonics Inc., Billerica, MA. Briefly, the matrix 2,6-dihydroxyacetophenone (DHAP) solution was prepared by dissolving 7.6 mg of DHAP in a mixed solvent of 375 µL ethanol and 125 µL of aqueous diammonium hydrogen citrate (DAHC) solution (18 mg/ml). One part of the sample solution (~100 pmol/µL protein) was mixed with one part of 2 % trifluoroacetic acid (TFA) and one part of DHAP solution. Approximately 1 to 2 µL were spotted on a stainless steel MALDI target when the crystallization started and the formerly clear mixture turned opaque. The intact protein mass spectra were acquired on an UltrafleXtreme MALDI-TOF/TOF mass spectrometer in linear mode after the spotted target was air-dried.

1.3.4. ***Isothermal Titration Calorimetry (ITC):*** Energetics associated with GOx(n) binding to CTDNA were measured using a nanocalorimeter (VP-ITC from Microcal Inc., Piscataway, NJ). GOx or GOx(n) solution was prepared by dissolving 10 mg/mL in distilled water and CTDNA solution was prepared by dissolving 1 mg/mL in 10 mM TrisHCl, 50 mM NaCl buffer (pH 7). The TrisHCl was used for the dialysis of GOx(n). Subsequent dialysis of GOx(n) and CTDNA separately in the same TrisHCl buffer equilibrated the two solutions at pH 7. The calorimeter was thermally equilibrated for 1 hour before dialyzed CTDNA was loaded into the calorimetric cell (1.4167 mL) and GOx(n) solution loaded in the automated syringe. During the experiment 8 µL aliquots of GOx(n) solution were added in successive injections to CTDNA (50 µM) using 300 s intervals. Heat absorbed or released with each injection was recorded.

The resulting thermograms were analyzed by Origin software (v. 5.0, Microcal Inc., Piscataway, NJ). The heats of dilution of GOx(n) and CTDNA were measured separately and subtracted from the titration data. The heat released or absorbed (Q) during the titration is related to the molar heat of GOx(n) binding (ΔH), the volume of the sample cell (V_o), the initial concentration of the ligand (X_t), CTDNA concentration (M_t), the binding constant (K_b), and the number of binding sites (n) by equation 1. The data were fitted to a single set of

$$Q = \frac{nM_t \Delta H V_o}{2}\left[1 + \frac{X_t}{nM_t} + \frac{1}{nK_b M_t} - \sqrt{\left(1 + \frac{X_t}{nM_t} + \frac{1}{nK_b M_t}\right)^2 - \frac{4X_t}{nM_t}}\right]$$

(Equation 1)

indistinguishable, non-cooperative binding sites model and K_b, n, ΔH and ΔS were obtained. Fits were performed multiple times with different initial values of K_b, n and ΔH to ensure that the global minimum was obtained. ΔS and ΔG were calculated from standard equations of thermodynamics.

1.3.5. ***Glucose oxidase activity assay:*** A solution of D-glucose (4 μM) was added to a mixture of GOx(n) (1 μM), horseradish peroxidase (HRP, 0.4 μM) in 10 mM TrisHcl 50 mM NaCl buffer pH 7 and guaiacol (*o*-methoxyphenol) (800 μM) dissolved in DI water. Oxidation of the substrate, guaiacol to a dimeric product that has an absorption maximum at 470 nm was monitored as a function of time at room temperature (25 ˚C).

1.3.6. ***Transmission Electron Microscopy (TEM):*** Structure and morphology of modified glucose oxidase and DNA was evaluated by use of TEM. Tecnai T12 TEM was used to acquire TEM micrographs. All images were obtained at an accelerating voltage of 120 kV. GOx(+40) concentration was 9.98 nM with a DNA concentration of 28.5 nM. The resulting solution was drop cast onto a Formvar film on copper grid. Excess solution was then blotted away using filter

paper and left to dry for 20 min. The samples were then stained using uranyl acetate for 30 min and images were recorded.

1.3.7. ***Circular Dichroism Studies:*** Circular Dichroism (CD) spectroscopy was used to monitor any structural changes of GOx(+50) due complex formation of GOx(+50)/DNA. A scan range of 200 nm - 350 nm was used to monitor the change in GOx(+50) secondary structure as well as DNA maximum and minimum. Change in ellipticity was recorded by a JASCO 710 spectropolarimeter. The buffer spectrum was used as a comparison to sample spectra. Step resolution was kept at 0.2 nm/data point. Bandwidth and sensitivity were 1 nm and 20 mdeg respectively. Three scans were averaged using a scan speed of 20 nm/min. Spectra were obtained in a 1 mm quartz cuvette and the data were normalized to millimolar concentration of the DNA or protein per unit path length.

1.4. Results

Electrostatic interactions are known to contribute to protein-DNA interactions but the existence of a threshold of positive charge on the protein has not been observed or hypothesized. By choosing a strongly negatively charged protein, we systematically examined the influence of increasing protein charge on DNA binding. We synthesized a small library of GOx(n) derivatives where the COOH groups of GOx were amidated with increasing numbers of TETA groups by carbodiimide chemistry (**Scheme 1**). Each TETA chain provides several protonation sites, and hence a net positive charge, and the amine groups could also contribute to favorable hydrogen bonding interactions for binding to DNA. The chemically modified protein samples were characterized by a number of physical and biochemical methods and their binding to the DNA helix has been examined by isothermal titration calorimetry (ITC). Our results are described below.

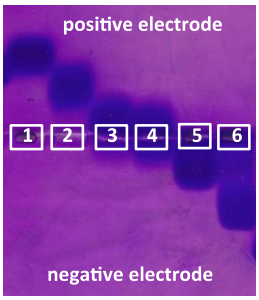

Figure 1.1. Agarose gel of GOx and GOx(n). GOx (lane 1) and GOx(n) conjugates (lanes 2-6) in Tris acetate buffer, pH 7. The samples have been spotted at the center of the gel, and migrated either to the positive or to the negative electrode depending on their net charge.

1.4.1. ***Agarose gel electrophoresis****:* The charge ladder of GOx(n) derivatives was produced by covalent attachment of the amine groups of TETA to the carboxyl groups of lysine side chains on GOx **(Scheme 1)**. Progress of GOx modification was monitored by agarose gel electrophoresis (pH 7, **Figures 1 and 2**) where the covalent modification decreased protein mobility toward the positive electrode (**Figure 1**, Lanes 2-4) and increased mobility toward the negative electrode (**Figure** 1, Lanes 5 and 6), depending on net protein charge. GOx(n) charges were assigned relative to GOx (**Figure 1**, Lane 1) that has a known charge of -62 at pH 7.0.[17] A GOx/TETA mixture (**Figure 2A**, lane 2) showed comparable migration to unmodified GOx, confirming the EDC driven mechanism required for conjugation. Samples with various charges (-35, -15, -10, +30, +50, +55, +60 and +75) were synthesized depending on the reaction conditions required for conjugation (**Figure 2**).

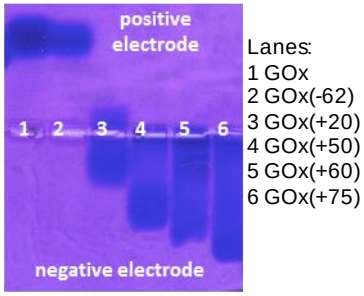

Lanes:
1 GOx
2 GOx(-62)
3 GOx(+20)
4 GOx(+50)
5 GOx(+60)
6 GOx(+75)

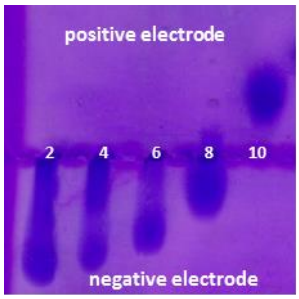

Lanes:
2 GOx(+75)
4 GOx(+60)
6 GOx(+50)
8 GOx(+20)
10 GOx(-40)

A **B**

Figure 1.2. Agarose gel of GOx and GOx(n) conjugates with sample migration on each gel determined relative to unmodified GOx. (A) GOx(n) charges range from -62 to +75 (B) GOx(n) charges range from -40 to +75. Samples were spotted at the center of the gel and migrated to each electrode depending on charge. The net charge of each conjugate is shown in parenthesis. Electrophoresis was done at pH 7.0 in 40 mM Tris-acetate buffer.

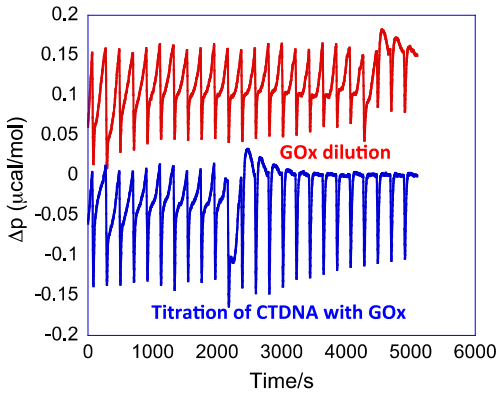
GOx dilution
Titration of CTDNA with GOx
Δp (μcal/mol)
Time/s

A

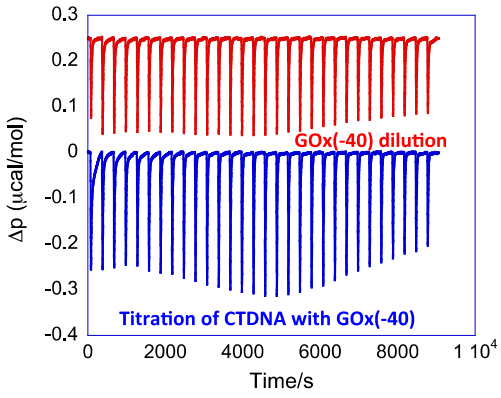
GOx(-40) dilution
Titration of CTDNA with GOx(-40)
Δp (μcal/mol)
Time/s

B

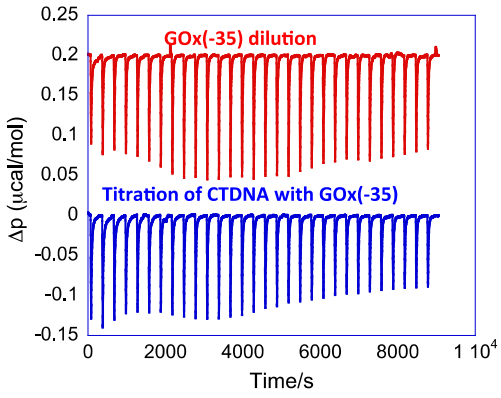
GOx(-35) dilution
Titration of CTDNA with GOx(-35)
Δp (μcal/mol)
Time/s

C

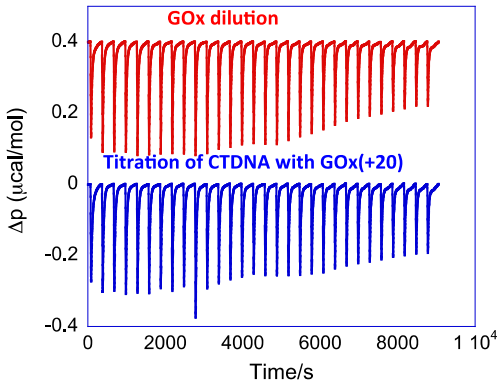
GOx dilution
Titration of CTDNA with GOx(+20)
Δp (μcal/mol)
Time/s

D

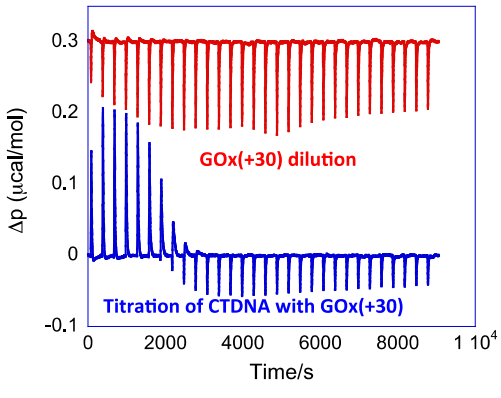
GOx(+30) dilution
Titration of CTDNA with GOx(+30)
Δp (μcal/mol)
Time/s

E

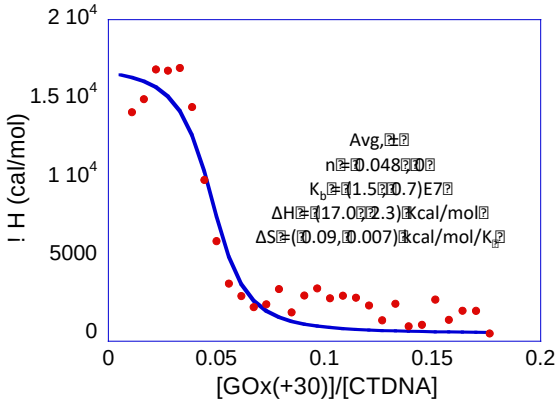
! H (cal/mol)
[GOx(+30)]/[CTDNA]

F

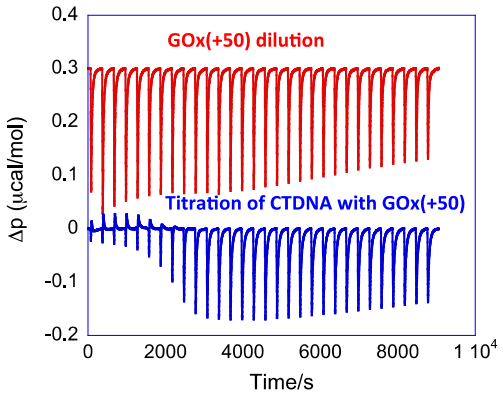
GOx(+50) dilution
Titration of CTDNA with GOx(+50)
Δp (μcal/mol)
Time/s

G

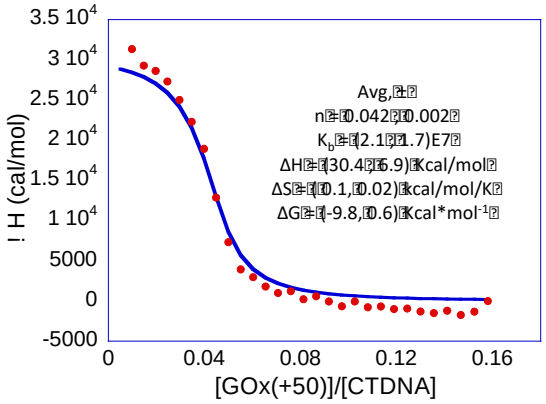
Avg,±
n=0.042±0.002
Kb=(2.1±1.7)E7
ΔH=(30.4±6.9)Kcal/mol
ΔS=(0.1,0.02)Kcal/mol/K
ΔG=(-9.8,0.6)Kcal*mol-1
! H (cal/mol)
[GOx(+50)]/[CTDNA]

H

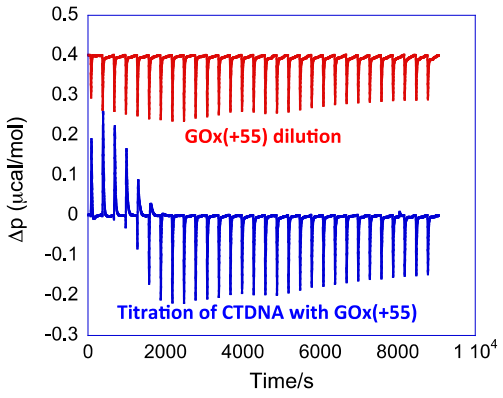
GOx(+55) dilution
Titration of CTDNA with GOx(+55)
Δp (μcal/mol)
Time/s

I

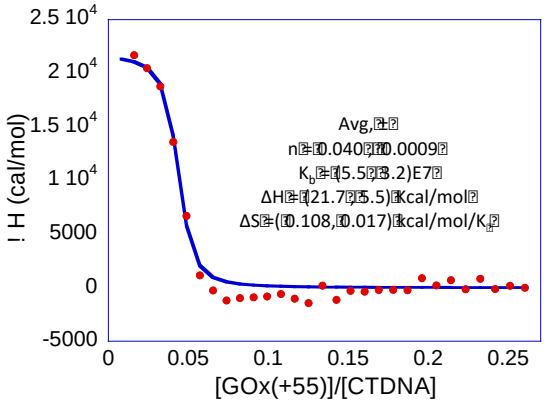
Avg,±
n=0.040±0.0009
Kb=(5.5±3.2)E7
ΔH=(21.7±5.5)Kcal/mol
ΔS=(0.108,0.017)Kcal/mol/K
! H (cal/mol)
[GOx(+55)]/[CTDNA]

J

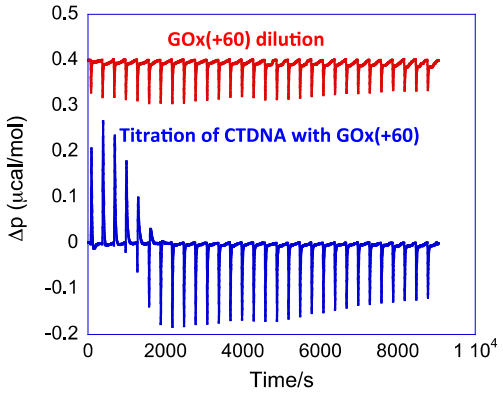
GOx(+60) dilution
Titration of CTDNA with GOx(+60)
Δp (μcal/mol)
Time/s

K

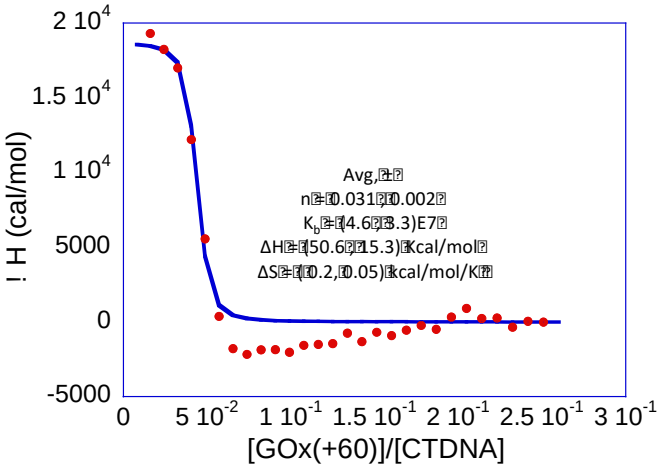
Avg,±
n=0.031±0.002
Kb=(4.6±3.3)E7
ΔH=(50.6±15.3)Kcal/mol
ΔS=(0.2,0.05)Kcal/mol/K
! H (cal/mol)
[GOx(+60)]/[CTDNA]

L

Figure 1.3. Isothermal titration calorimetry data for the titration of CTDNA (50 μM) with GOx (A) and GOx(n) (B through L) in 10 mM TrisHCl, 50 mM NaCl buffer at pH 7. Binding was not observed when CTDNA was titrated with unmodified GOx or GOx(n) for n values from -62 to +20. A minimum net charge of +30 was required for binding to CTDNA. Binding isotherms were obtained by the addition of protein solution to CTDNA (blue curves E, G, I, and K). The dilution data (red curves) are off set from the titration curves. Change in enthalpy with increasing [GOx(n)] is observed for charges +30 to +75 (F, H, J, and L). The blue line is the best fit to the data according to the single, identical, non-interacting binding site model. Data are shown as an average of triplicate measurements.

The number of TETA attachments in GOx(n) was examined by mass spectrometry analysis of GOx(+75) that confirmed a total number of 44 TETAs (MW 146.23) conjugated to GOx (**Figure 4**). An increased m/z from 142,896.3 Da (pristine GOx**, Figure 4A**) to 149,344.3 Da (GOx(+75), **Figure 4B**) was observed. Each TETA is expected to contribute a charge of +2 due to protonation of two nitrogens of TETA with pKa values of 9.20 and 9.92,[21] and the fourth nitrogen has pKa less than 7. One of the four nitrogens is used to form the amide bond consuming a negatively charged carboxyl group. Thus, GOx(+75) with 44 TETAs should have +88 units charge added due to 44 TETA chains, and would lose -44 units of charge due to amide formation, hence modifying its charge from -62 to (-62 + 88 - (-44)) = +70. This is in good agreement with the net charge of +75 observed using agarose gel measurements.

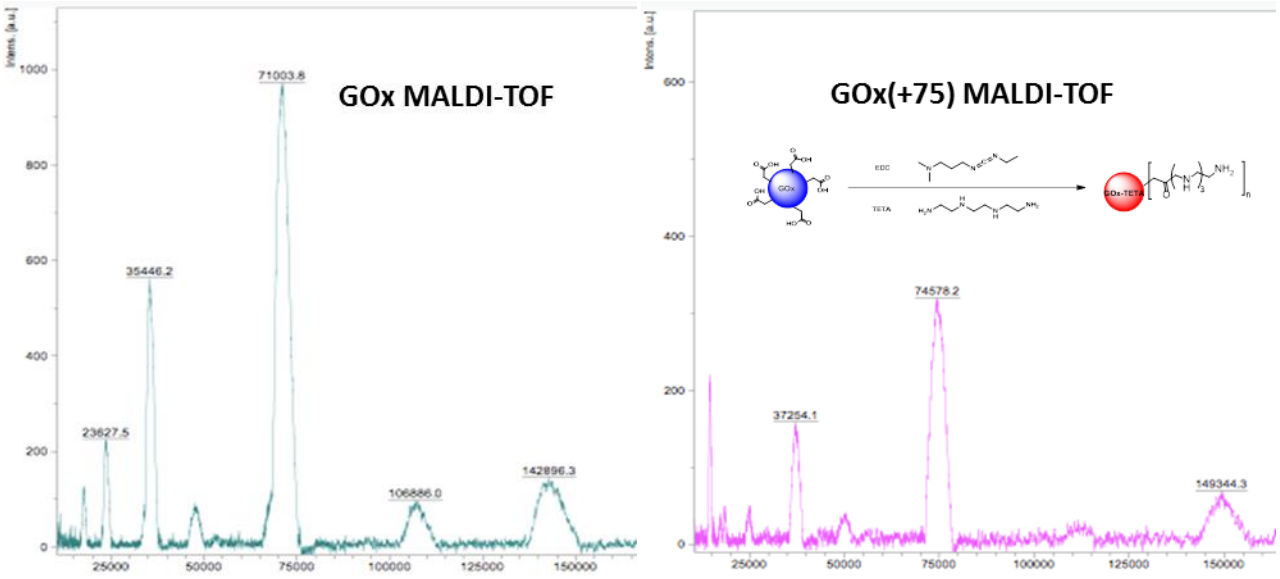

A **B**

Figure 1.4. MALDI-TOF mass spectra of (A) GOx and (B) GOx(+75). Increased m/z values in the case of GOx(+75) supported the attachment of TETA chains to GOx.

1.4.2. ***Isothermal Titration Calorimetry:*** The binding thermodynamics of GOx(n) to DNA has been quantified by isothermal titration calorimetry and the binding constants, stoichiometries, binding enthalpies and entropies were extracted (**Table 1**). Samples with charges -40, -35, +20, +30, +50, +55, +60 and +75 (**Figure 3**) were loaded into the automated calorimeter syringe. A solution of calf thymus DNA (CTDNA) was loaded into the calorimetric cell with successive injections of GOx(n) aliquots from the syringe and data acquired. The highest charge of n = +75 is shown in **Figure 5A**, as an example of the ITC titration, and the heat was absorbed (blue curve) with the addition of GOx(+75) (46 μM) to CTDNA (50 μM), where both samples are pH matched in 10 mM TrisHCl, pH 7.0, exactly. A control experiment of GOx(n) titration into the buffer was done to obtain the heat of dilution (**Figure 5A**, red curve), under otherwise identical conditions and used for subtractions.

The peaks were integrated and the enthalpy change corresponding to each addition of GOx(n) was plotted as a function of the ratio of concentration of GOx(n) to that of the DNA (**Figure 5B**, red dots). These binding data were fitted to a single set of indistinguishable, non-cooperative binding sites model (**Figure 4B**, blue curve), using equation 1, by methods established in our laboratory.[22] The best-fit to the data (**Figure 5B**) indicated K_b, ΔG, ΔH, and $T\Delta S$ values of $(7.3 \pm 2.8) \times 10^7$ M^{-1}, -10.7 ± 0.25, 46.1 ± 2.1 and 56.6 ± 2.4 kcal/mol, respectively for the n = +75 sample. The binding of GOx(n) to CTDNA is dependent on the value of n as discussed below.

1.4.3. ***Charge dependence of GOx(n) binding to DNA***: A charge ladder of GOx(n) from n = -62 to n = +75 was synthesized as above. No binding was observed with pristine GOx, or GOx(n) ($n < +30$) in the ITC titrations (**Figure 3**, A-D, ΔH, ΔS, and $\Delta G = 0$), but GOx(n)/DNA binding was switched on at $n \geq +30$. (**Figure 3**, E-L). ITC titrations, therefore, indicated all or no binding depending on the value of n (**Table 1**), where DNA binding was observed for n values of +30,

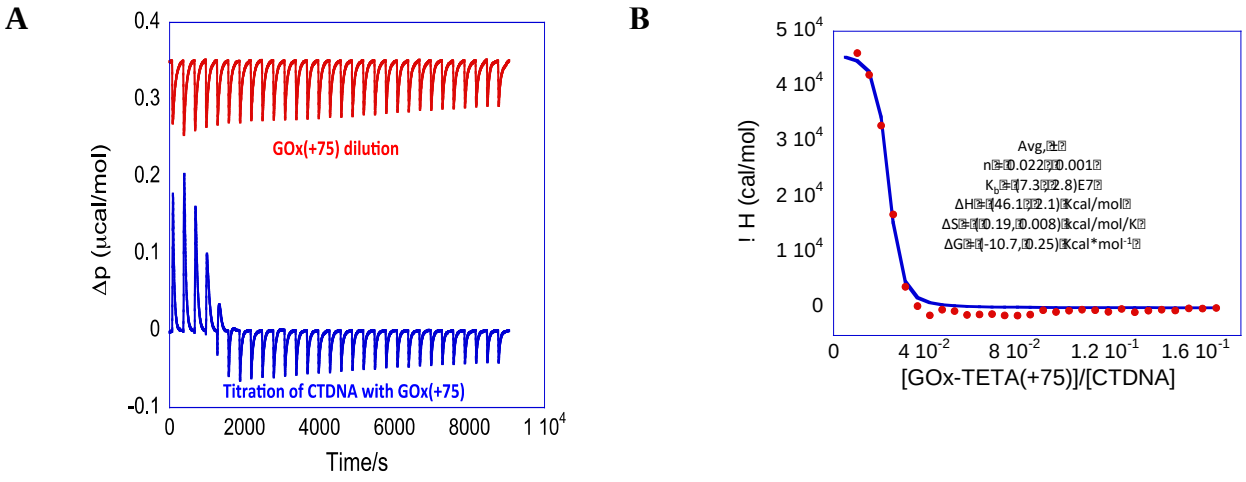

Figure 1.5. Titration of GOx(+75) into calf thymus DNA (CTDNA). (A) The thermogram obtained by the addition of GOx(n) solution to the CTDNA solution (blue curve), and the dilution data (red curve), off set for clarity. (B) The integrated heat as a function of [GOx(+75)]/[CTDNA], while the blue line is the best fit to the data using a non-interacting, independent, identical binding site model. The binding data were averaged from three separate measurements.

Table 1.1. Summary of thermodynamic parameters for GOx(n) binding to CTDNA

Charge ± 5 (n)	ΔH (kcal/mol)	TΔS (kcal/mol)	ΔG (kcal/mol)	K_b x 10^7 (M^{-1})
30	17.0 ± 2.3	26.8 ± 2.1	-9.75 ± 0.14	1.5 ± 0.7
50	30.4 ± 6.9	38.7 ± 6.0	-9.80 ± 0.6	2.0 ± 1.7
55	21.7 ± 5.5	32.1 ± 5.1	-10.3 ± 0.6	5.5 ± 3.2
60	50.6 ± 15.3	59.6 ± 14.9	-9.50 ± 1.2	4.6 ± 3.3
75	46.1 ± 2.1	56.6 ± 2.4	-10.7 ± 0.25	7.3 ± 2.8

+50, +55, +60, and +75 but not for n values of -62, -35, -40, and +20. The corresponding thermograms and best-fits to the data for ΔH as a function of [GOx(n)]/[CTDNA] for n values -62 to +75 are shown in **Figure 6**. The binding is entirely entropy driven with an enthalpic penalty and endothermic binding has been noted when the binding has occurred. Protein modification was done in batches, resulting in the specific values of n reported here.

The ΔH (red curve) and ΔG (blue curve) values plotted as a function of n clearly illustrate that binding is suddenly switched on at $n \geq +30$ (**Figure 6**), and that the sharp, step function observed in both plots is unique, not seen before, and indicated an on or off switch, as in a digital device. The step-transition could be due to the strongly acidic nature of pristine GOx which has 59 COOH groups that will have charge-charge repulsion from the negatively charged DNA phosphate backbone, unless neutralized. Conjugation with TETA reduces the number of these anionic groups as well as the net negative charge. We find that a minimum number of conjugated TETAs on the protein is required to overcome these unfavorable repulsive forces to create a favorable Gibbs free energy change, and switch on the DNA/protein binding interaction. DNA/protein interactions are complex[23] and may require a threshold number of favorable Coulombic contacts. The step binding observed here is unique to DNA because similar studies using protein/solid[19] or protein/poly(acrylic acid) resulted in a linear relationship between thermodynamic parameters of complex formation and protein charge.

Transmission Electron Microscopy (TEM) of GOx(+40)/DNA (**Figure 6B**) using 10 nM GOx(+40) and 28.5 nM CTDNA suggests DNA wraps or loops around GOx(+40). The dark areas measure about 15 to 20 nm in diameter and may represent dimers of GOx(+40) since pristine GOx has a monomeric diameter of approximately 5.5 nm.[24] The white strands may

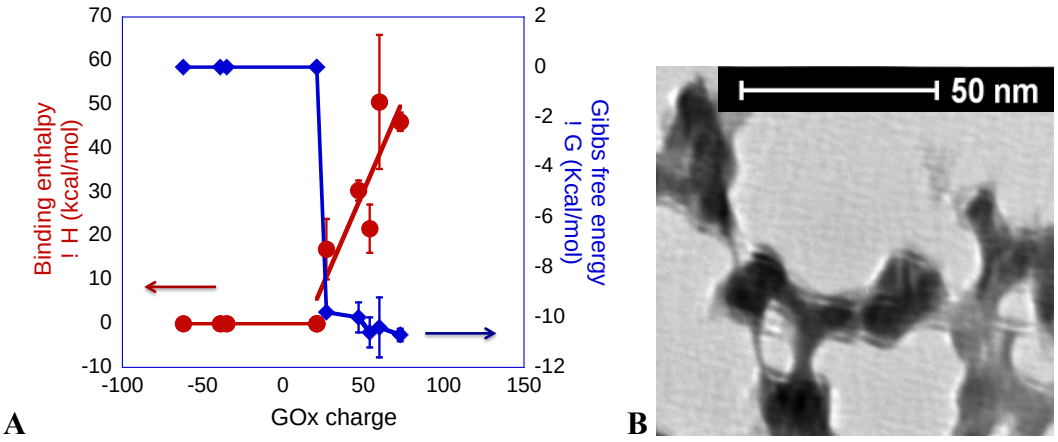

Figure 1.6. (A) The binding enthalpies (red dots) and Gibbs free energies (blue dots) for the interaction of GOx(n) with CTDNA. A threshold charge of +30 is required for GOx(n) interaction with DNA. At or above n = +30 a favorable ΔG (blue curve) and enthalpic penalty (unfavorable ΔH) (red curve) are observed, and GOx(n)/DNA interaction is entirely entropy driven against the enthalpic penalty. Each data point represents an average of 3 trials. In some cases, the error bars are too small to be visible. (B) TEM image of GOx(+40)/DNA.

represent DNA wrapping or looping around GOx(+40). No visible structures were observed when GOx(-40)/DNA (**Figure 7A**) or GOx(+20)/DNA (**Figure 7B**) was imaged.

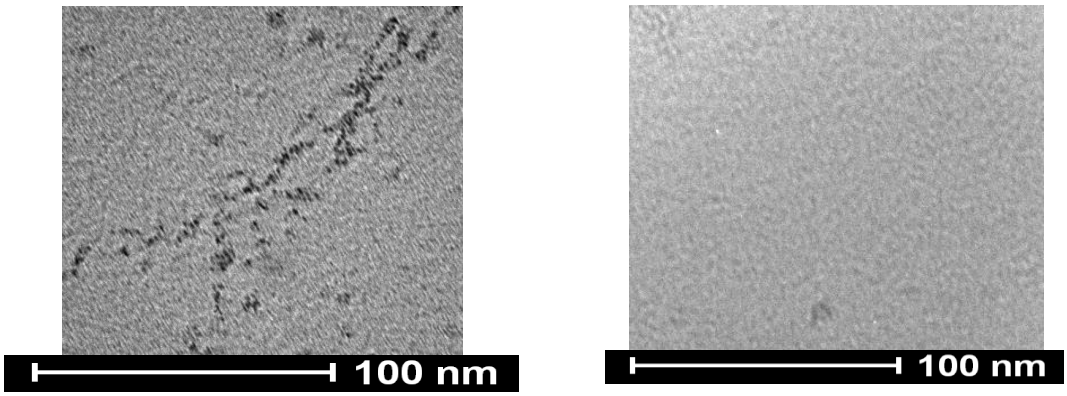

A **B**

Figure 1.7. TEM images of (A) GOx(-40)/DNA and (B) GOx(+20)/DNA suggest GOx(n) does not bind DNA when n = -40 or +20.

We examined structural changes of both the protein and DNA due to binding interactions by circular dichroism (CD) spectroscopy, which indicated structure retention of GOx after amidation to yield GOx(n) analogues (**Figure 8A**) over a wide range of n values from -20 to +95 in 10 mM TrisHCl and 50 mM NaCl, pH 7 with GOx(n) concentrations in the range of 2 – 3 μM. Although substantial loss in intensity was observed possibly due to the randomness of GOx amidation sites, spectral shape and thus structure retention was not affected. Deconvolution of the CD spectra to examine DNA CD, after protein CD was subtracted from the observed spectrum of DNA/protein mixture in 10 mM TrisHCl and 50 mM NaCl, pH 7 (**Figure 8B**) revealed a correlative reduction of DNA signal as GOx(+50) concentration has been increased from 0.3 to 0.9 μM. The influence GOx(n) charge (**Figure 8C**, [GOx(n)] = 0.9 μM, [DNA] = 100 μM) on DNA CD revealed a slight peak shift and loss in intensity in the far UV of GOx(+20)/DNA and GOx(+50)/DNA CD when compared to that of GOx(-10)/DNA or that of DNA. These may be due to changes in DNA structure when positively charged GOx(n) interacts with the double helix. In fact, CD studies have demonstrated that histone proteins condense DNA on binding to the helix, hence a reduction in DNA CD signal intensity was observed due to histone/DNA complex formation.[25,26]

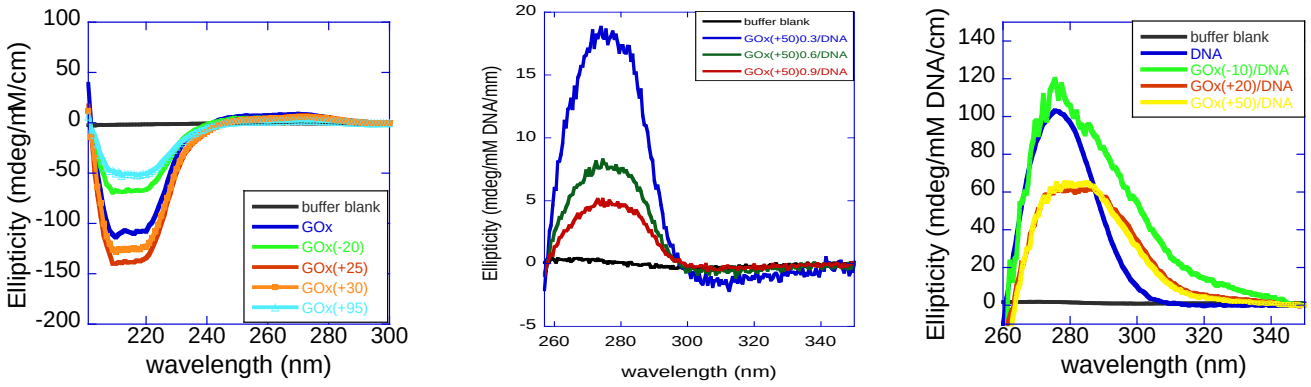

A **B** **C**

Figure 1.8. Circular Dichroism (CD) spectra of GOx(n) and GOx(n)/DNA. (A) Structure retention of GOx(n) when compared to unmodified GOx (blue curve) was observed over a wide range of charges (n) from -20 to +95 while substantial loss in intensity has been noted in some cases, as marked. GOx(n) concentration was in the range of 2 – 3 μM in 10 mM TrisHCl, 50 mM NaCl buffer. (B) Normalized CD spectra of GOx(+50) in the TrisHCl buffer mentioned above with respect to DNA concentration after subtracting the CD spectrum of GOx(+50) shows a corresponding decrease in DNA CD intensity with increased GOx(+50) concentration. (C) When GOx(n) and DNA concentrations are held constant at 0.9 μM and 100 μM respectively, a loss in DNA CD intensity was observed when n = +20 and +50 (red and yellow curves respectively) when compared to DNA (blue curve) or GOx(-20)/DNA (green curve).

We also examined the influence of DNA on modulating the oxidase activities of GOx(n) as a function of n (**Figure 9**). Glucose was used as the substrate, and the reduction of ambient oxygen to form hydrogen peroxide was assayed by horseradish peroxidase (0.4 μM) and its substrate guaiacol (*o*-methoxyphenol) (800 μM), which yield a dimeric product with an absorption maximum at 470 nm. GOx(n) solutions (n = -62, 20, 50, 60, and 75), 1 μM enzyme, and 4 μM glucose in 10 mM TrisHCl 50 mM NaCl buffer, pH 7 in the absence or presence of 50 μM DNA, were examined and all these retained nearly-full activities. The DNA double helix may influence GOx(n) activity upon complex formation as noted by the increases in activity of 5%, 21%, 10%, and 10% observed when GOx(n) associated with DNA for n = 20, 50, 60, or 75, respectively.

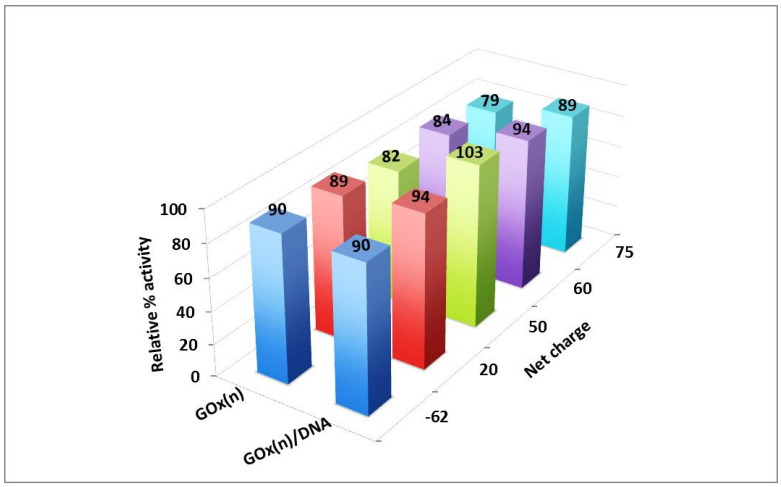

Figure 1.9. Oxidase activities of GOx(n) and GOx(n)/DNA complexes. Protein and DNA concentrations were 1 μM and 50 μM, respectively, in 10 mM TrisHCl, 50 mM NaCl buffer at pH 7. A solution of D-glucose (4 μM) was added to a mixture of GOx(n) (1 μM) and horseradish peroxidase (HRP, 0.4 μM) and guaiacol (*o*-methoxyphenol) (800 μM) dissolved in DI water. Initial specific activities relative to that of GOx under the same experimental conditions are reported. The GOx(n) activities are comparable to that of pristine GOx after cationization or upon complexing with DNA. All samples were completely soluble under all these conditions.

1.5. Discussion

The entropy driven binding observed here is comparable to the binding thermodynamics of histone/DNA complexes[27] and could be due to GOx(n) displacing DNA bound water molecules from the grooves. In that case, the data suggest that a minimum charge value (n = +30) is required for this kind of binding, and overcoming local charge repulsion contexts. The balance of these complex interactions could justify the step function observed here. Alternatively, certain types of DNA looping are entropy driven,[28] and hence, a minimum number of TETA contacts may be required for helix bending and looping around GOx(n).

There was no significant variation of the Gibbs free energy and binding constant as protein surface charge was increased. This is likely due to enthalpy-entropy compensation observed when protein is in solution,[29,30,31] whereby most of the entropic gain due to release of ions and water is offset by the enthalpic penalty for the formation of protein/DNA interfacial contacts. When conjugated to protein surface carboxyls and interacting at the protein/DNA interface, TETA chains afford the net favorable entropy observed here due to release of counterions and water. However, the enthalpic cost of bending and distorting DNA[32,33] may be enough to off-set much of the entropic gain such that ΔG is mostly unaffected. The protein/DNA interface is very dynamic and after binding is turned on, factors other than electrostatics may contribute to the energetics. Therefore, the error of +/- 5 charge units reported here is acceptable given that ΔG is unaffected by core protein surface charge increase after binding to DNA is turned on.

Protein modification has been used in this work to control protein/DNA interactions by tuning the protein charge. Manipulation of the protein surface functions by TETA amidation has been used to control protein/polymer interactions[34] when hemoglobin was conjugated with

TETA to yield Hb-TETA derivatives similar to the GOx(n) derivatives reported here. PEGylation of bovine serum albumin (BSA)[35] resulted in substantial changes in the protein structure when polyethylene glycol (PEG) was covalently attached to BSA and complex protein engineering procedures have been accomplished by *in vivo* manipulation of an organism's biosynthetic machinery.[36] Proteins have been site specifically tagged using complex synthetic methods or *in vivo* mutagenesis techniques[37,38] to produce libraries of labeled derivatives for imaging and other applications.

Mass spectrometry analysis provides accurate quantitation of protein modification events[39,40] but sample prep and method development could be time consuming, requiring a high level of expertise. All charge determinations in this work were done by agarose gel electrophoresis that is accurate, low cost, rapid, and requires comparatively minimal method development and expertise. In fact, agarose gel determinations were shown to be within reasonable error of ±5 charge units as discussed above.

Circular dichroism studies indicated variable signal intensity due to GOx amidation (**Figure 4A**) which could be due to the randomness of amidation chemistry, wherein TETA conjugation to any specific carboxyl is dependent on the local environment and solvent accessible carboxyls available for conjugation. However, GOx pristine structure was retained after amidation as observed by the similarity of GOx(n) CD spectra to that of GOx. The effect of increased GOx(n) concentration on DNA helicity indicated decreased DNA intensity. Previous work that studied the effect of increased protein concentration on DNA in histone/DNA complexes reported comparable decreased DNA CD intensity[25] or red shifting of the DNA far UV peak in addition to decreased DNA CD intensity.[26]

Here, DNA signal intensity was comparable to DNA alone when 0.3 μM GOx(+50) was complexed to DNA but DNA signal intensity decreased by approximately 40% when compared to DNA alone if 0.6 μM GOx(+50) was added and there was an additional 25% reduction in DNA intensity when 0.9 μM GOx(+50) was added, resulting in a total reduction of DNA CD intensity of about 65% (**Figure 4B**). The effect of charge was studied by variation of n in the GOx(n) derivatives. Comparison of the far UV CD of GOx(-10)/DNA, GOx(+20)/DNA, and GOx(+50)/DNA after subtraction of GOx(n) CD and normalization by DNA concentration revealed a trend comparable to the step binding observed between the binding thermodynamics of GOx(n)/DNA and n (**Figure 3A**). GOx(-20)/DNA far UV intensity was comparable to DNA alone (**Figure 4C**) but GOx(+20)/DNA and GOx(+50)/DNA far UV intensity decreased and showed some degree of red shifting with respect to DNA alone suggesting that a minimum number of electrostatic contacts are required to overcome repulsive forces at the GOx/DNA interface. Based on ITC studies, the minimum n required for binding was observed to be +30, therefore a GOx(n) charge of +20 may be optimal to initiate weak interactions with DNA, thus altering the DNA CD. Also, circular dichroism may be more sensitive to minor changes in DNA structure that occur due to weak association with GOx(n) molecules that are below the minimum charge threshold required for ITC detection.

GOx(n) activities were monitored and relative % activity was determined relative to pristine GOx activity. GOx conjugated to a low concentration of TETA (5 mM) using low concentration EDC (5 mM) yielded GOx(-62) with comparable net charge to pristine GOx. However, GOx(-62) relative % activity was 10% less than that of pristine GOx suggesting that even minimal amidation was enough to negatively affect the GOx active site. GOx(+20) was also about 10% less active than pristine GOx and as GOx amidation increased to yield GOx(+50),

GOx(+60), and GOx(+75) relative % activity was decreased by an average of 20% suggesting that the increased amidation had a negative impact on the GOx active site.

GOx(n) bound to DNA (GOx(n)/DNA) showed increased activity over unbound GOx(n) over a range of n values from +20 to +75 by 5% to 20% suggesting that DNA enhances GOx activity. In the case of GOx(+50)/DNA, relative % activity was increased 20% over GOx(+50) alone. In fact, GOx(+50)/DNA complex formation restored GOx(+50) activity comparable to that of pristine GOx. GOx(n)/DNA complex formation may enhance GOx(n) activity due to reduced protein mobility[41,42] or DNA enhancement of GOx(n) activity.[43] Indeed, DNA control of GOx activity has been reported.[44] Taken together these data suggest that DNA interacts with the GOx(n) active site either directly or indirectly to enhance GOx(n) activity.

The stoichiometry of twenty base pairs DNA interacting with one GOx(n) monomer observed here suggests wrapping of DNA around GOx(n) 1.5 turns if GOx monomeric diameter is 55 Å.[24] In the case of the nucleosome, DNA wraps around a histone core 1.75 turns[1] and gene regulation results from tightening and loosening of the wrapped DNA. The choice of GOx as the core protein in this study afforded control of electrostatics by tuning the core charge over a wide range from -62 to +75. These findings should impact the determination of unit charge requirements for specific histone modification events[45] and contribute to the thermodynamic understanding of histone/DNA interactions.

The entropy gain described here plays a crucial role in the binding energetics at the protein/DNA interface. We have used the Ion Coupled Protein Binding (ICPB) model[46,47] to demonstrate that counterion release at an enzyme-solid interface is entropically favorable when a cationic protein binds oppositely charged surfaces. This suggests that the entropy term will be further increased in the case of protein/DNA interaction due to the flexibility of the DNA double helix.

1.6. Conclusion

The step binding observed here between GOx(n) and DNA above a threshold charge supports the hypothesis that charge plays a vital role in binding but the step function is surprising. Similar situations may be operative in biological systems where specific histone modifications are required to wind/unwind DNA and impact gene regulation in particular ways. The hypothesis proposed was incorrect and could not account for the observed step function. For example, histone acetylation or deacetylation specifically alters the histone surface charge and influence of charge on DNA binding is an important factor. The GOx(n)/DNA model reported here can potentially be used to predict charge requirements for the design of artificial histone proteins or DNA-digital switches. This is the first study elucidating the thermodynamic details of a DNA digital switch.

1.7. References

(1) Fenley, A. T.; Adams, D. A.; Onufriev, A. V. Charge state of the globular histone core controls stability of the nucleosome. *Biophys. J.* **2010,** *99*, 1577-1585.

(2) Rea, S.; Eisenhaber, F.; O'Carroll, D.; Strahl, B. D.; Sun, Z.-W.; Schmid, M.; Opravil, S.; Mechtler, K.; Ponting, C. P.; Allis, C. D. Regulation of chromatin structure by site-specific histone H3 methyltransferases. *Nature* **2000,** *406*, 593-599.

(3) Sun, Z.-W.; Allis, C. D. Ubiquitination of histone H2B regulates H3 methylation and gene silencing in yeast. *Nature* **2002,** *418*, 104-108.

(4) Korolev, N.; Vorontsova, O. V.; Nordenskiöld, L. Physicochemical analysis of electrostatic foundation for DNA–protein interactions in chromatin transformations. *Prog. Biophys. Mol. Biol.* **2007,** *95* (1), 23-49.

(5) Privalov, P. L.; Dragan, A. I.; Crane-Robinson, C.; Breslauer, K. J.; Remeta, D. P.; Minetti, C. A. What drives proteins into the major or minor grooves of DNA? *J. Mol. Biol.* **2007,** *365*, 1-9.

(6) Saecker, R. M.; Record Jr, M. T. Protein surface salt bridges and paths for DNA wrapping. *Curr. Opin. Struct. Biol.* **2002,** *12*, 311-319.

(7) Levene, S. D., Giovan, S. M., Hanke, A., and Shoura, M. J. The thermodynamics of DNA loop formation, from J to Z. *Biochem. Soc., Trans.*, **2013**, *41*, 513-518.

(8) Esadze, A.; Chen, C.; Zandarashvili, L.; Roy, S.; Pettitt, B. M.; Iwahara, J. Changes in conformational dynamics of basic side chains upon protein–DNA association. *Nucleic Acids Res.* **2016**, 44 (14), 6961-6970.

(9) de Graff, A. M.; Hazoglou, M. J.; Dill, K. A. Highly Charged Proteins: The Achilles' Heel of Aging Proteomes. *Structure* **2016,** *24* (2), 329-336.

(10) Jayaram, B.; McConnell, K.; Dixit, S. B.; Das, A.; Beveridge, D. L. Free-energy component analysis of 40 protein–DNA complexes: a consensus view on the thermodynamics of binding at the molecular level. *J. Comput. Chem.* **2002,** *23* (1), 1-14.

(11) Zhang, W.; Bond, J. P.; Anderson, C. F.; Lohman, T. M.; Record, M. T. Large electrostatic differences in the binding thermodynamics of a cationic peptide to oligomeric and polymeric DNA. *Proc. Natl. Acad. Sci. U.S.A.* **1996,** *93* (6), 2511-2516.

(12) Jones, S.; Shanahan, H. P.; Berman, H. M.; Thornton, J. M. Using electrostatic potentials to predict DNA-binding sites on DNA-binding proteins. *Nucleic Acids Res.* **2003,** *31* (24), 7189-7198.

(13) Chen, C.; Esadze, A.; Zandarashvili, L.; Nguyen, D.; Pettitt, B. M.; Iwahara, J. Dynamic equilibria of short-range electrostatic interactions at molecular interfaces of protein–DNA complexes. *The J. Phys. Chem. Lett* **2015,** *6* (14), 2733-2737.

(14) Privalov, P. L.; Dragan, A. I.; Crane-Robinson, C. Interpreting protein/DNA interactions: distinguishing specific from non-specific and electrostatic from non-electrostatic components. *Nucleic Acids Res.* **2010**, gkq984.

(15) Mack, A. H.; Schlingman, D. J.; Ilagan, R. P.; Regan, L.; Mochrie, S. G. J. Kinetics and thermodynamics of phenotype: Unwinding and rewinding the nucleosome. *J. Mol. Biol.* **2012**, 423, 687-701.

(16) Tan, W. B.; Cheng, W.; Webber, A.; Bhambhani, A.; Duff, M. R.; Kumar, C. V.; McLendon, G. L. Endonuclease-like activity of heme proteins. *J Biol Inorg Chem* **2005,** *10*, 790-799.

(17) Pazur, J. H.; Kleppe, K. The Oxidation of Glucose and Related Compounds by Glucose Oxidase from Aspergillus niger. Biochemistry **1964**, 3, 578-583.

(18) Hodak, J.; Etchenique, R.; Calvo, E. J.; Singhal, K.; Bartlett, P. N. Layer-by-layer self-assembly of glucose oxidase with a poly (allylamine) ferrocene redox mediator. *Langmuir* **1997,** *13*, 3008-3016.

(19) Chowdhury, R.; Stromer, B.; Pokharel, B.; Kumar, C. V. Control of Enzyme-Solid Interactions via Chemical Modification. *Langmuir* **2012,** *28*, 11881-11889.

(20) Hoare, D. G.; Koshland, D. E. A method for the quantitative modification and estimation of carboxylic acid groups in proteins. *J. Biol. Chem.* **1967,** *242*, 2447-2453.

(21) Nishimura, M.; Hayashi, M.; Hayakawa, K.; Miyazaki, M. Ion Chromatographic Study of Sulfate-Complexes in Aqueous Solution. *Anal. Sci.* **1994,** *10*, 321.

(22) Kumar, C. V.; Duff Jr, M. R. DNA-Based Supramolecular Artificial Light Harvesting Complexes. *J. Am. Chem. Soc.* **2009,** *131*, 16024-16026.

(23) Levy, Y.; Onuchic, J. N.; Wolynes, P. G. Fly-casting in protein-DNA binding: frustration between protein folding and electrostatics facilitates target recognition. *J. Am. Chem. Soc.* **2007,** *129* (4), 738-739.

(24) Kumar, C. V.; Chaudhari, A. Proteins immobilized at the galleries of layered α-Zirconium phosphate: Structure and activity studies. *J. Am. Chem. Soc.* **2000,** *122* (5), 830-837.

(25) Moraán, F.; Montero, F.; Azorín, F.; Suau, P. Condensation of DNA by the C-terminal domain of histone H1 A circular dichroism study. *Biophys. Chem.* **1985,** *22* (1-2), 125-129.

(26) Fasman, G. D.; Schaffhausen, B.; Goldsmith, L.; Adler, A. J. Conformational changes associated with f-1 histone-deoxyribonucleic acid complexes. Circular dichroism studies. *Biochemistry* **1970,** *9* (14), 2814-2822.

(27) Machha, V.; Jones, S.; Waddle, J.; Le, V.; Wellman, S.; Lewis, E. Exploring the energetics of histone H1. 1 and H1. 4 duplex DNA interactions. *Biophys. Chem.* **2014,** *185*, 32-38.

(28) Levene, S. D.; Giovan, S. M.; Hanke, A.; Shoura, M. J. The thermodynamics of DNA loop formation: from J to Z. *Biochem. Soc. Trans* **2013,** *41*, 513-518.

(29) Lumry, R.; Rajender, S. Enthalpy-Entropy compensation phenomena in water solutions of proteins and small molecules: a ubiquitous properly of water. *Biopolymers* **1970**, 9, 1125-1227.

(30) Liu, L.; Yang, C.; Guo, Q.-X. A study on the enthalpy-entropy compensation in protein unfolding. *Biophys. Chem.* **2000**, 84, 239-251.

(31) Tzeng, S.-R.; Kalodimos, C. G. Dynamic activation of an allosteric regulatory protein. *Nature* **2009,** 462, 368-372.

(32) Dragan, A. I.; Read, C. M.; Makeyeva, E. N.; Milgotina, E. I.; Churchill, M. E. A.; Crane-Robinson, C.; Privalov, P. L. DNA binding and bending by HMG boxes: energetic determinants of specificity. *J. Mol. Biol.* **2004,** *343*, 371-393.

(33) Peters, W. B.; Edmondson, S. P.; Shriver, J. W. Thermodynamics of DNA binding and distortion by the hyperthermophile chromatin protein Sac7d. *J. Mol. Biol.* **2004,** *343*, 339-60.

(34) Thilakarathne, V. K.; Briand, V. A.; Kasi, R. M.; Kumar, C. V. Tuning Hemoglobin-Poly (acrylic acid) Interactions by Controlled Chemical Modification with Triethylenetetramine. *The J. Phys. Chem. B.* **2012,** *116*, 12783-12792.

(35) Abuchowski, A.; Van Es, T.; Palczuk, N.; Davis, F. Alteration of immunological properties of bovine serum albumin by covalent attachment of polyethylene glycol. *J. Biol. Chem.* **1977,** *252* (11), 3578-3581.

(36) Kiick, K. L.; Saxon, E.; Tirrell, D. A.; Bertozzi, C. R. Incorporation of azides into recombinant proteins for chemoselective modification by the Staudinger ligation. *Proc. Natl. Acad. Sci. U.S.A.* **2002,** *99* (1), 19-24.

(37) Hou, Y.; Yuan, J.; Zhou, Y.; Yu, J.; Lu, H. A Concise Approach to Site-Specific Topological Protein-Poly (Amino Acid) Conjugates Enabled by In-situ Generated Functionalities. *J. Am. Chem. Soc.* **2016**, 138 (34), 10995-11000.

(38) Glasgow, J. E.; Salit, M. L.; Cochran, J. R. In Vivo Site-Specific Protein Tagging with Diverse Amines Using an Engineered Sortase Variant. *J. Am. Chem. Soc.* **2016**, 138 (24), 7496-7499.

(39) Batalha, I. L.; Zhou, H.; Lilley, K.; Lowe, C. R.; Roque, A. C. Mimicking nature: Phosphopeptide enrichment using combinatorial libraries of affinity ligands. *J. Chromatogr. A* **2016**, 1457, 29, 76-87.

(40) Haller, E.; Lindner, W.; Lämmerhofer, M. Gold nanoparticle–antibody conjugates for specific extraction and subsequent analysis by liquid chromatography–tandem mass spectrometry of malondialdehyde-modified low density lipoprotein as biomarker for cardiovascular risk. *Anal. Chim. Acta* **2015,** *857*, 53-63.

(41) Zhang, Y.; Ge, J.; Liu, Z. Enhanced activity of immobilized or chemically modified enzymes. *ACS Catalysis* **2015,** *5* (8), 4503-4513.

(42) Abbasi, M.; Amiri, R.; Bordbar, A.-K.; Ranjbakhsh, E.; Khosropour, A.-R. Improvement of the stability and activity of immobilized glucose oxidase on modified iron oxide magnetic nanoparticles. *Appl. Surf. Sci.* **2016,** *364*, 752-757.

(43) Nguyen, K. V.; Holade, Y.; Minteer, S. D. DNA redox hydrogels: Improving mediated enzymatic bioelectrocatalysis. *ACS Catalysis* **2016,** *6* (4), 2603-2607.

(44) Engelen, W.; Janssen, B.; Merkx, M. DNA-based control of protein activity. *Chem. Commun*. **2016,** *52* (18), 3598-3610.

(45) Tessarz, P.; Kouzarides, T. Histone core modifications regulating nucleosome structure and dynamics. *Nat Rev Mol Cell Biol* **2014,** *15* (11), 703-708.

(46) Duff Jr, M. R.; Kumar, C. V. Protein-Solid Interactions: Important Role of Solvent, Ions, Temperature, and Buffer in Protein Binding to α-Zr(IV) Phosphate. *Langmuir* **2009**, 25, 12635-12643.

(47) Duff Jr, M. R.; Kumar, C. V. Molecular Signatures of Enzyme-Solid Interactions: Thermodynamics of Protein Binding to α-Zr(IV) Phosphate Nanoplates. *J. Phys. Chem. B.* **2009**, 113, 15083-15089.

Chapter 2: Tuning Glucose Oxidase Interactions with α-$Zr(HPO_4)_2$ Nanoplates via Chemical Modification

2.1. Abstract

A simple method to control enzyme-solid interfacial interactions via chemical modification of the surface functions of glucose oxidase (GOx) with improved affinity for negatively charged α-Zr(IV)Phosphate nanoplates is demonstrated here. Understanding enzyme-solid interactions in terms of detailed specific molecular features and rationally controlling these interactions for better outcomes is of value from fundamental, as well as practical points of view. In this context, we systematically tuned GOx charge from -62 to +95 electrostatic units and examined its affinity for an anionic nanomaterial as a function of enzyme charge. Charge tuning was achieved via chemical modification of the accessible COOH groups on the enzyme by carbodiimide mediated coupling with triethylenetetramine (TETA) to produce GOx-TETA analogues (GOx(n)) where n represents enzyme charge after the chemical modification. Isothermal titration calorimetric study of GOx(n) binding to exfoliated nanoplates of α-Zr(IV)Phosphate in 20 mM 1,4-Piperazinediethanesulfonic acid (PIPES) buffer indicated ΔH and ΔS values of (-371.3 ± 52.8) kcal/mol and (-1.2 ± 0.2) kcal/molK respectively for GOx(-20) and there was no interaction between unmodified GOx and α-Zr(IV)Phosphate. Furthermore, TETA modification facilitated GOx affinity for the α-ZrP nanosheets with a binding constant (K_b) of (2.1 ± 0.6) x 10^6 M^{-1} for GOx(-20). Variation of net GOx charge from n = -62 to n = +30 yielded ΔH, ΔS, and ΔG values in the ranges of (0 to -427.2 ± 39.0) kcal/mol, (0 to -1.4 ± 0.1) kcal/molK, and (0 to -9.0 ± 2.8) kcal/mol respectively with linear independence. The role of TETA side chains and the net charge

on GOx(n) indicated specific physical insight into the nature of enzyme/solid interactions. This study provided a simple, predictable, chemical tool to control bio-inorganic interfaces at constant temperature, pH and ionic strength with particular advantages, and such approaches are important for biosensor and biocatalytic applications.

2.2. Introduction

Using glucose oxidase (GOx) as a model enzyme and α-Zr(IV) phosphate (α-ZrP) as a model nanomaterial, we report a simple method to control the enzyme-nanomaterial interactions in a systematic manner, with positive outcomes. Understanding the details of enzyme/nanomaterial interactions, for example, is of fundamental importance for the rational design of functional, stable and robust biosensors,[1] biocatalysts,[2] and biomedical devices.[3] Chemical control of these interactions is vital to enhance specific characteristics such as enzyme affinity for the nanomaterial, its activity, stability and other critical properties of the enzyme. Specifically, proteins[4,5,6] and peptides[7] have been intercalated into the galleries of α-Zr(IV) phosphate (α-ZrP) after exfoliation of α-ZrP with tetrabutylammonium hydroxide (TBA). Binding affinities of GOx is increased from that of the pristine enzyme by orders of magnitude by tuning its charge (**Scheme 1**). The COOH groups of GOx are modified with triethylenetetramine (TETA) via carbodiimide chemistry by attaching increasing numbers of TETA side chains (x) to GOx, where x_1, x_2, and x_3 represent increasing numbers of TETA groups.

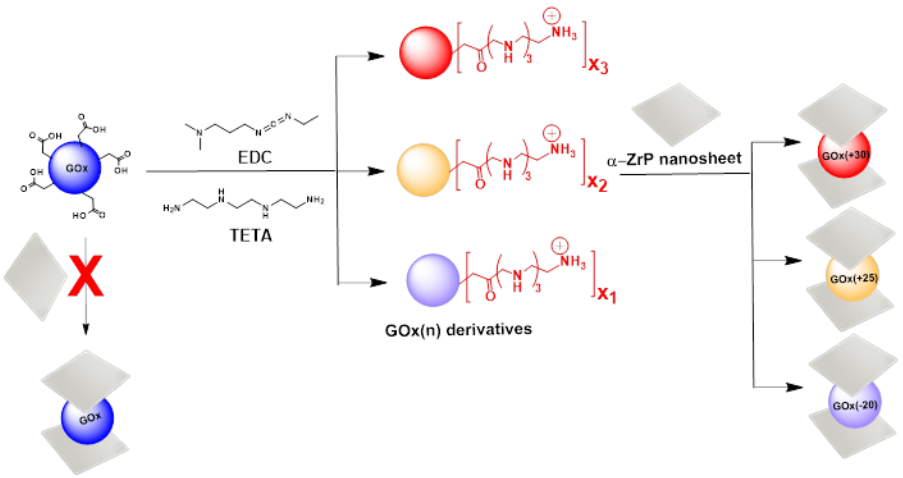

Scheme 2.1. GOx(n) binding to exfoliated α-ZrP nanosheets. The COOH groups of GOx, amidated with increasing numbers of TETA (x) using carbodiimide chemistry resulted in tuning of GOx surface charge (n) from negative (pristine GOx, dark blue sphere) to positive (red sphere). The negatively charged GOx (-62) does not bind to the negatively charged α-ZrP plates but charge reversal from negative to positive (light blue, yellow, and red spheres), triggered GOx binding.

Glucose oxidase has been bound to several supports including polymers,[8, 9] graphene nanocomposites,[10] and gold nanoparticle-zinc oxide nanostructures.[11] GOx was chosen for the current studies due to its promise as an anode catalyst in biofuel cells, [12, 13] its use in glucose sensors[14, 15, 16, 17] and its ability to use oxygen for oxidations. GOx, for example, oxidizes glucose to gluconic acid while reducing oxygen to hydrogen peroxide,[18, 19] and this reaction has a wide range of applications.[20, 21] The thermodynamic details of GOx binding to well-defined nanosolids are not well understood and these details could be important for building better sensors, biocatalysts or enzyme-electrodes for practical applications.[22]

Zirconium phosphate ($Zr(HPO_4)_2$) nanoparticles have been used for drug delivery,[23] to stabilize metal organic frameworks for improved catalysis[24] and for enhanced ion exchange.[25] Also, enzyme nanocomposites with $Zr(HPO_4)_2$ show increased stability of proton conductivity.[26] GOx and α-ZrP biocomposites have been implicated in applications such as improved glucose sensing,[27] and increased GOx stability,[28] but thermodynamic quantification of GOx/α-ZrP binding interaction has not been well characterized.

We hypothesized that enzyme binding to charged nanosheets can be described by the ion-coupled protein-binding model (ICPB).[29] According to this model, cationic enzymes are surrounded by anionic counter ions as an enzyme approaches the negatively charged α-ZrP nanosheets that are surrounded by cationic counterions (**Scheme 2A**). Release of cations from the binding interface is necessary for the charge neutralization required to facilitate enzyme/solid affinity. This counter ion release is the basis of the entropy driven binding associated with the cationic protein/solid surface interaction. On the other hand, the binding of anionic proteins to anionic α-ZrP nanosheets requires sequestration of counter ions at the protein/solid interface to offset the buildup of excess negative charge (**Scheme 2B**). Thus, binding is driven by enthalpy

release and opposed by entropy decrease.[30] In support of the ICPB mechanism , it was reported that protein binding to α-ZrP is coupled to proton binding, buffer ion protonation, counter ion binding/release, and water release.[31] Furthermore, other factors such as protein conformational

Scheme 2.2. Demonstration of the ion coupled protein-binding (ICPB) model. (A) Binding of a cationic protein (red sphere) to anionic solid (blue rectangles) is associated with counterion release from the anionic surface to maintain charge neutrality at the binding interface. (B) Binding of an anionic protein (blue sphere) to anionic solid is associated with counterion sequestration from the solvent to the binding interface in order to maintain charge neutrality.

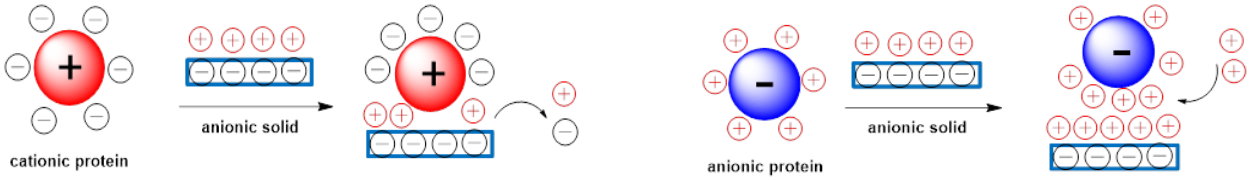

A **B**

changes, van der Waals interactions, hydrogen bonding, and the hydrophobic effect is expected to contribute to the overall change in Gibbs free energy during a binding event.

Along these lines, specific metal ions were successfully used to continuously tune the binding affinity of anionic GOx to the anionic α-ZrP nanosheets, [32] revealing that metal ions that have favorable interactions with the enzyme/solid increased the binding affinities the most. In another study, GOx modified with a polyamine with increasing charge has indicated enhanced affinities for graphene oxide but affinity decreased as the net charge on the enzyme increased beyond a threshold.[33] A similar strategy is used here to tune the affinities of GOx-TETA derivatives with increasing positive charge to yield GOx(n) analogues, where n is the net charge on the enzyme. Control of the enzyme surface charge in this way allows for control of GOx(n) affinity for the strongly negatively charged layered solid (α-ZrP, inset) (**Scheme 3**).

Scheme 2.3. Exfoliation of α-ZrP (gray sheets) using TBA affords the binding of cationized GOx (red spheres, GOx(n)) to the exfoliated nanosheets. An XRD signature of exfoliation (inset) confirms that a substantial portion of the α-ZrP stacks (2θ = 11.9 with a d spacing of 7.5 Å) has been exfoliated as evidenced by the increased d spacing (2θ = 6.1 with a d spacing of 14.5 Å).

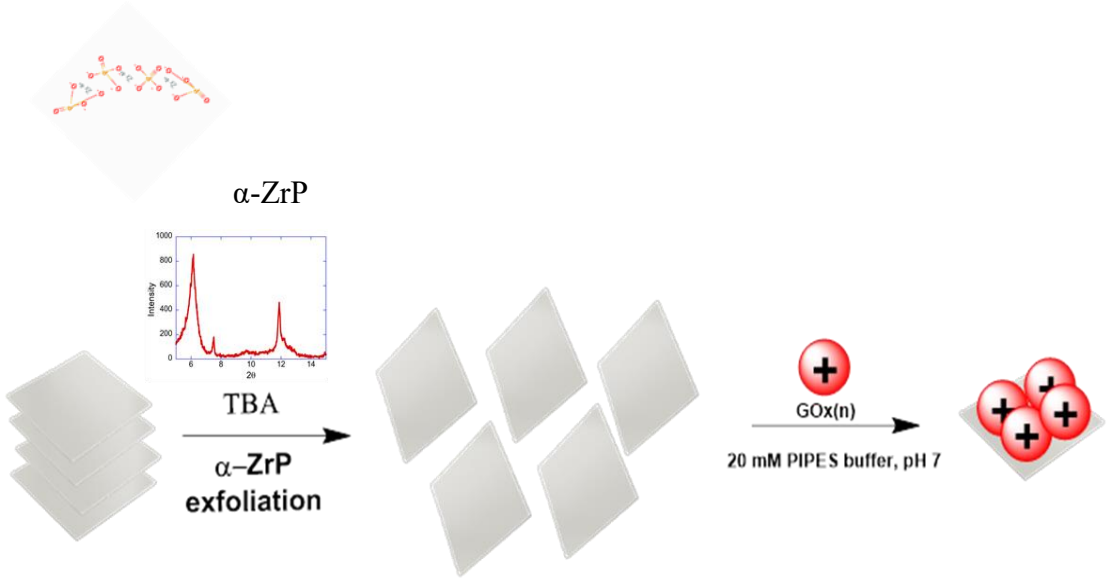

We report here, enhanced binding of GOx(n) to exfoliated α-ZrP (n > 0) and we used isothermal titration calorimetry to quantify GOx(n)/α-ZrP binding enthalpy (ΔH), entropy (ΔS), and free energy (ΔG) contributions. Our hypothesis is the same as in the previous chapter and that the binding free energy should smoothly vary with protein charge. Surface plasmon resonance (SPR) determined affinity of GOx(n)/α-ZrP yielded dissociation constants (K_D) values comparable to binding constants (K_b) values determined by ITC. Additionally, the rate of association (on rate, K_{on}) and rate of dissociation (off rate, K_{off}) of each GOx(n)/α-ZrP interaction was determined by SPR. Exfoliation of the α-ZrP nanosheets with tetrabutylammonium hydroxide (TBA) was confirmed by X-ray diffraction (XRD) (**Scheme 3**, inset), where the decreased peak intensity at 2θ = 11.9 with a d spacing of 7.5 Å between α-ZrP layers and the increased intensity at 2θ = 6.1 with an increased d spacing of 14.5 Å between layers was signature for exfoliation.

2.3. Materials and Methods

Glucose oxidase from *aspergillus niger* (GOx, 165,000 MW) was purchased from Calzyme Laboratories, Inc. (Tulelake, CA) and used without further purification. Triethylenetetramine (TETA) and 1-ethyl-3-(3-dimethylaminopropyl)-carbodiimide hydrochloride (EDC) were purchased from Sigma-Aldrich (St. Louis, MO). Solutions were prepared in 20 mM Piperazine-N,N´-bis(2-ethanesulfonic acid) sodium salt (NaPIPES) and 1 mM aqueous tetrabutyl ammonium hydroxide (TBA) (Sigma) pH adjusted to 7.0.

2.3.1 ***Synthesis and exfoliation of α-ZrP:*** The synthesis was carried out by following a method reported previously.[34] Briefly, 9 M phosphoric acid was heated to 90 ºC, and a solution of 10.1 g of $ZrOCl_2$ (0.031 mol, 10 mL of water) was added over a period of 1 h and allowed to reflux for 24 h. The reaction mixture was filtered, washed with water to remove excess acid, and then

washed with acetone. The solid was dried at 60 ºC overnight and characterized by powder X-ray diffraction (XRD) (**Scheme 3** inset) which matched with the literature report.[4] In the solid state, these nanoplatelets are stacked, but these are exfoliated with TBA.[35] A suspension of α-$Zr(HPO_4)_2 \cdot H_2O$ (0.1 g) in 20 mM NaPIPES buffer was sonicated for 5 min, 200 µL of TBA (40% w/w) was added, sonicated again for 20 min, and pH was adjusted to 7.0 by dilute HCl, followed by sonication for an additional 10 minutes. The enzyme was bound to the exfoliated ZrP nanosheets by methods described previously.[4]

Pristine GOx was replaced by chemically modified GOx(n) and binding has been assessed by ITC.[36] TETA and EDC concentrations were kept to a minimum to minimize precipitation of the modified GOx during dialysis in NaPIPES buffer.

2.3.2 ***Chemical modification:*** GOx was modified by adopting reported methods[37] with appropriate modifications. In a typical experiment, the GOx (10 mg/ml) dissolved in deionized water (DI) was stirred with TETA (pH adjusted to 4.5) for 30 minutes, followed by the addition increasing concentrations of EDC (10 - 100 mM). The reaction mixture was stirred for 4 h, and unreacted EDC, TETA and urea byproducts were removed by dialysis against NaPIPES buffer. Modified GOx (10 mL) was repeatedly dialyzed in buffer (1L) every h for a total of 2 h. This dialysis procedure was repeated for modified GOx and exfoliated α-ZrP together in the same buffer in order to equilibrate GOx and α-ZrP pH. The degree of chemical modification was carefully controlled by adjusting TETA and EDC concentrations (10 mM TETA with 5-100 mM EDC) such that GO-TETA charge is increased gradually, as evidenced from agarose gels of the reaction mixtures.

2.3.3. ***Agarose gel electrophoresis:*** Agarose gel electrophoresis was performed using horizontal gel electrophoresis apparatus (Gibco model 200, Life Technologies Inc, MD) and agarose (0.5 %

w/w) in 40 mM Tris acetate buffer at pH 7.0, as described before.[38] In a typical run, modified enzymes were loaded with 50% loading buffer (50% v/v glycerol and 0.01% w/w bromophenol blue). The running buffer used for all samples was Tris acetate (40 mM). Samples were spotted into wells placed at the middle of the gel, so that samples could migrate to the negative or positive electrode based on their charge. A voltage of 100 V was applied for 30 minutes. Gels were stained overnight with 10% v/v acetic acid, 0.02% w/w Coomassie blue, followed by destaining in 10 % v/v acetic acid overnight. Net charge of modified GOx was determined by imageJ software (NIH) based on migration distance of each of the GOx-TETA conjugates relative to GOx that has a known charge of -62 at pH 7.[39,40]

2.3.4. ***Isothermal Titration Calorimetry (ITC):*** Binding thermodynamics were measured by a nanocalorimeter (VP-ITC from Microcal Inc., Piscataway, NJ), as described before[41] In a typical titration run, GOx or GOx-TETA solutions (10 mg/mL) were prepared in 20 mM NaPIPES and α-ZrP solution was prepared by dissolving 6 mM α-ZrP in 20 mM NaPIPES and 1 mM aqueous TBA (pH 7.0). All the chemically modified proteins were purified in the working buffer by extensive dialysis. The calorimeter was thermally equilibrated for 1 h before the sample was loaded into the calorimeter (1.4167 mL) and protein solutions were loaded in the automated syringe. Aliquots of protein solutions (8 μL) were injected successively into α-ZrP suspension, at 300 s intervals. Heat absorbed or released with each injection was recorded and plotted automatically.

Heats of dilution were measured separately, under the same conditions, except that protein solution in the syringe was injected into the calorimeter cell that was filled with buffer solution and the dilution data was subtracted from the sample titration data. The resulting thermograms were analyzed by Origin software (v. 5.0, Microcal Inc., Piscataway, NJ). The heat released or

absorbed (Q) during the titration is related to the molar heat of GOx binding (ΔH), the volume of the sample cell (V_o), the initial concentration of the ligand (X_t), α-ZrP concentration (M_t), the binding constant (K_b), and the number of binding sites (n) by the following equation.[42,43]

$$Q = \frac{nM_t \Delta H V_o}{2}\left[1 + \frac{X_t}{nM_t} + \frac{1}{nK_b M_t} - \sqrt{\left(1 + \frac{X_t}{nM_t} + \frac{1}{nK_b M_t}\right)^2 - \frac{4X_t}{nM_t}}\right]$$

Equation 2.

The data were fitted to a single set of non-interacting, identical binding site model and K_b, n, ΔH and ΔS were obtained, as described previously.[36,44] Fits to data sets were performed multiple times with different initial values of K_b, n, and ΔH in order to check for reproducibility of the final values of these parameters. Values of ΔG were calculated from the standard equation of thermodynamics.

2.3.5. ***Surface Plasmon Resonance:***

Preparation and Characterization of Exfoliated α-ZrP Thin Films: Prior to spin coating, gold SPR sensors (from Reichert catalog #13206060) were cleaned with piranha (3:1 H_2SO_4/H_2O_2) for 15 minutes, followed by soaking in ethanol solution for 20 minutes and rinsing with excess distilled water. The already TBA exfoliated α-ZrP solution was spin cast (Laurel Technologies WS-400B-6NPP/LITE, North Wales, PA) at 3000 rpm for 1 minute. The exfoliated α-ZrP film was slowly dried at room temperature. Finally, the film was immersed in reaction buffer overnight then used for SPR experiments.

Atomic Force Microscopy (AFM), and SEM were used to characterize the α-ZrP films. Scanning with Asylum Research MFP-3D AFM (Santa Barbara, CA, USA) was used to assess substrate distribution in film, surface roughness, and topography. The scans were taken in non-

contact mode using Si_3N_4 tips with a force constant of 40N/m (according to the manufacturer) and a typical resonant frequency of 170 ± 20 kHz. Finally, Energy-dispersive X-ray spectroscopy (EDX) analysis of the SPR sensors after GOx(n) bound α-ZrP was used to measure the nitrogen weight percent.

SPR Experiment: In a typical SPR experiment, degassed buffer solution without enzyme was flowed into the SPR sensor chamber assembled with the α-ZrP coated SPR gold chip (sensors). Degassed buffer was continuously flowed into the SPR chamber for an hour to allow the α-ZrP film to fully swell and reach equilibrium, establishing a stable baseline. Following this, the enzyme (GOx(n)) solution was continuously introduced into the cell with a syringe pump at flow rate of 25 μL/min. In this study, all the SPR traces were recorded on an SR7000DC dual channel flow SPR spectrometer from Reichert Analytical Instruments (NY, USA) with a semi-automatic injection setup with 500 mL PEEK injection loop and Harvard Apparatus flow pump. The SPR data were collected at room temperature in 20mM PIPES, pH 7.0 buffer. For kinetic studies, a 100 μL sample loop was used for injection.

Binding Kinetics of GOx on Exfoliated α-ZrP: Exfoliated α-ZrP was spin coated at 3000 rpm onto the surface of SPR gold chips. Solutions of unmodified GOx, GOx(+20), GOx(+45), GOx(+60), and GOx(+65) ranging in concentrations from 31.25 nM to 500 nM were prepared in 20 mM PIPES, pH 7.0 buffer. Typically, enzyme solutions were injected into the SPR system at 25 μL min^{-1} for specific association and dissociation times. GOx samples were continuously flowed for 240 s. After adsorption of GOx (i.e system reaches equilibrium), the flow was switched to PIPES buffer with no enzyme.

Kinetic Models for Binding of GOx(n) to Exfoliated α-ZrP film: Kinetic traces of real time SPR data of GOx(n) on α-ZrP films corresponding to association and dissociation phases were

deconvoluted to yield the on and off rates. The nonlinear equations of 1:1 equilibrium binding model (Scrubber II built-in software, Biologic Software, Australia) was used to fit the various concentrations and charge dependent data for GOx(n). The association phase was fitted globally using Equation 2 and dissociation of protein was fitted using Equation 3. This nonlinear regression analysis finds the minimum sum of squares solution giving the best values of the association rate constant (k_a), dissociation rate constant (k_d), and maximum binding signal (R_{max}) where C = bulk enzyme concentration, R_t = response time, t = association and/or dissociation time. The on-rate (ka), and off-rate (k_d), constants were used to calculate apparent K_D from Equation 4.

$$R_t = Ck_aR_{max}[1 - \exp -((Ck_a + k_d)t)]/(Ck_a + k_d) \qquad \text{Equation 3.}$$

$$R_t = R_{max} \exp(-k_d t) \qquad \text{Equation 4.}$$

$$K_D = (k_d/k_a) \qquad \text{Equation 5.}$$

2.3.6. ***Zeta Potential Measurements:*** A Brookhaven Zeta Plus zeta potential analyzer (Brookhaven Instrument Corporation, Holtsville NY) was used for laser Doppler velocimetry studies to measure zeta potential, as described previously[32] In a typical run, the suspensions were prepared using 6 mM α-ZrP and protein concentrations in the range of 40 μM to 50 μM in 20 mM NaPIPES buffer at pH 7.0. Sample measurements were done in a 4 mL polystyrene cuvette after equilibrating the samples for 30 minutes at room temperature. The zeta potential values were obtained from electrophoretic motility of the suspension using Smoluchowski fit[45] using Brookhaven Instrument Particle Solution v 2.3 software provided by the manufacturer.

2.3.7. ***Glucose oxidase activity:*** Activities of GOx-TETA/α-ZrP, GOx-TETA and unmodified glucose oxidase (GOx) were determined by following a previously reported method.[46] A solution of D-glucose (4 μM) was added to a mixture of GOx (1 μM), horseradish peroxidase (HRP, 0.4

μM) in 10 mM NaPIPES buffer pH 7.2 and guaiacol (*o*-methoxyphenol) (800 μM) dissolved in DI water. Oxidation of the substrate, guaiacol to a dimeric product with absorption maximum at 470 nm was monitored as a function of time at room temperature (25 ˚C). A plot of time v/s absorption (**Figures 2B and 3**) was used to calculate the initial rates from the linear portion of the kinetic trace (first ~20 points).

2.3.8. ***Circular Dichroism Studies:*** Circular Dichroism (CD) spectroscopy was used to assess protein secondary structural changes, as described previously[47,48] Far-UV CD (190 nm - 260 nm) spectra of GOx, GOx(n), or samples bound to α-ZrP were recorded by a JASCO 710 spectropolarimeter (Jasco Inc, Easton MD) The baseline recorded with the buffer was nearly flat and has been subtracted from sample spectra with step resolution kept at 0.2 nm/data point while Bandwidth and sensitivity were 1 nm and 20 mdeg, respectively. Three scans were averaged using a scan speed of 50 nm/min and spectra were obtained with a path length of a 0.05 cm quartz cuvette and normalized to molar concentration of the protein per unit path length. While GOx(n):α-ZrP stoichiometry was the same as those used for ITC analysis, α-ZrP concentration was kept at a minimum to minimize light scattering.

2.4. Results

Variation of enzyme charge by modification of GOx with TETA that attach to COOH groups of Asp and Glu has facilitated the investigation of enhancement of GOx(n) affinity for α-ZrP. The effect of GOx(n) charge on GOx(n)/α-ZrP binding was thermodynamically quantified. Protonation of the free amine groups of TETA side chain contributes to the net charge on GOx(n) where increasing the number of TETA groups attached to the enzyme is associated with increase in enzyme charge. Attachment of TETA enables the interaction of these newly introduced amine functions with the negatively charged phosphate groups of the α-ZrP surface. Binding of TETA to α-ZrP was quantified by ITC, yielding large ΔH and ΔS values of (-6027 ±

98.6) kcal/mol and -20.2 kcal/molK respectively, and the binding constant was (2.5 ± 0.6) x 10^8 M^{-1} with a ΔG of -11.4 kcal/mol. Such a robust thermodynamic response may be driven by electrostatic as well as hydrogen bonding interactions between the amine groups of TETA and the phosphate groups of α-ZrP.[49,50] Therefore, we hypothesized that attachment of TETA chains to GOx could promote its binding to anionic α-ZrP. Thus, we quantified binding interactions between GOx(n) and α-ZrP nanosheets by ITC and then characterized the bound enzyme by spectroscopic and activity studies. These observations are reported here.

2.4.1. ***Chemical Modification of Glucose Oxidase:*** The net charge on GOx was gradually increased from -62 (pristine GOx at pH 7, pI 4.3)[39,40] to +65 by reacting the COOH groups of the enzyme with increasing amounts of TETA (10 mM – 30 mM), under specific conditions of pH, temperature, EDC concentration and reaction time (**Scheme 1**). Two of the four TETA nitrogens (pKa values = 9.20 and 9.92)[51] are expected to be protonated under these experimental conditions (pH = 7). One nitrogen will be neutralized to form the amide bond during GOx modification, and the pKa value of the fourth nitrogen is too low for protonation to occur. Therefore, a net unit charge gain of +2 is expected for every TETA that binds GOx, and this chemical modification reaction provided a strong chemical handle to control GOx(n) charge at a fixed pH. These GOx(n) samples, in turn, provided a simple method to study how enzyme charge influenced its interactions with α-ZrP nanosheets at a fixed pH. The resulting GOx(n) derivatives have been purified extensively by dialysis to remove unreacted reagents and by-products of urea. The progress of the reaction has been monitored by agarose gel electrophoresis which indicated a set of GOx(n) derivatives with decreasing negative charge or increasing positive charge, presented below.

2.4.2. ***Agarose gel electrophoresis***: The reaction mixture was analyzed by gel electrophoresis to monitor the progress of the chemical modification reaction (**Figure 1**). GOx is strongly negatively charged at pH 7.0 (-62) and thus, migrated toward the positive electrode in the agarose gel (**Figure 1**, Lane1). Chemically modified GOx-TETA samples were loaded into wells at the center of the gel (white boxes), so that enzyme migration would occur toward the positive or the negative electrode. Modified GOx samples migrated less toward the positive electrode or moved toward the negative electrode (lanes 3-8) depending on the extent of chemical modification, in a systematic manner. Thus, the net negative charge was increased gradually, until charge reversal occurred (lanes 5-8) where the enzyme migrated toward the negative electrode. Variation of TETA and EDC concentrations yielded increasingly charged GOx(n) as a charge ladder. The charge on each of the derivatives was determined relative to that of pristine GOx, under the same conditions of buffer, pH and temperature, by measuring the relative migration distances in the agarose gel. Additional samples were prepared in batches and charges of each sample determined (**Figure 2**) and the error in n reported here is estimated to be ±5 units.

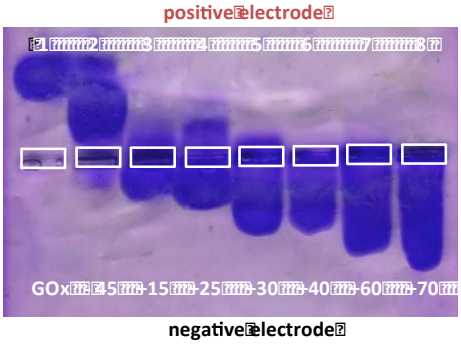

Figure 2.1. Agarose gel of GOx and GOx(n) conjugates at pH 7.0 in 40 mM Tris-acetate. Samples were spotted at the center of the gel and they migrated to the opposite electrode depending on their charge. Net GOx Charge estimated from these elrectrophoretic mobilities are shown at the bottom of the gel.

Two key assumptions were made in the charge estimation of the GOx(n) derivatives: 1. Enzyme size is nearly the same before vs after the chemical modification so that it did not influence enzyme migration distance in the gel, and 2. Charge on the modified enzyme is directly proportional to the distance of its migration under the influence of the applied electric field and there has been no substantial interaction between the enzyme and the agarose matrix. The first assumption is reasonable because TETA length is negligible when compared to the average diameter of GOx (54 Å),[4] and appending these short chains onto the enzyme surface may not alter its diameter to a significant extent. The validity of the second assumption is reasonable because agarose is charge neutral but there could be some H-bonding interaction between the amine functions of the TETA chains on the enzyme and the OH groups of the agarose matrix.[52] Indeed, we suspect that these H-bonding interactions might be responsible for the trailing bands seen in the agarose gels. Therefore, we also tested the estimated charge on one sample with that of the mass spectral data, as described below.

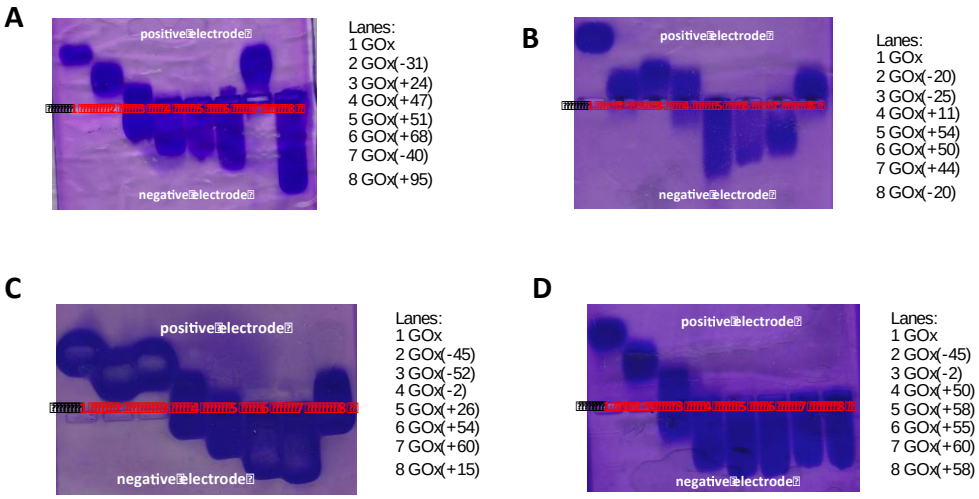

Figure 2.2. Agarose gel of GOx and GOx(n) conjugates at pH 7.0 in 40 mM Tris-acetate buffer. Charge ranges (n) are (-40 - +95), (-25 - +54), (-52 - +60), and (-45 - +60) (A through D respectively). Samples were spotted at the center of the gel and migrated to each electrode depending on the charge. The net charge of each conjugate is shown in parenthesis.

Protein modification was carried out by holding TETA concentration constant (10 mM) and increasing EDC concentration from 10 mM – 30 mM (**Figure 1**, lanes 2 through 7) in 5 mM increments to yield charge values of -45, +15, +25, +30, +40, and +60 for lanes 2 through 7, respectively. Increasing TETA concentration to 20 mM and EDC concentration to 60 mM yielded a charge value of +70 (lane 8). The sample GOx(+70) was examined by mass spectrometry and m/z analysis revealed a peak shift from 142,896.3 Da for pristine GOx to 149,344.3 Da for the modified GOx, indicating a total number of 44 TETA side chains per GOx(n), and a net charge of +75.[53] Since the n value of this sample was determined to be +70 by agarose gel electrophoresis, the MS analysis, therefore, indicated a difference of 5 charge units between the two methodologies. Therefore, the error associated with agarose gel charge determinations throughout this study was reported to be ± 5 charge units.

2.4.3. ***Circular dichroism and enzyme activity studies of GOx(n) derivatives:*** In order to assess the effect of amine modification on enzyme structure, circular dichroism was used to analyze GOx structure retention after amidation and sample purification. The overall spectral shape of modified GOx samples was comparable to the spectral shape of unmodified GOx and this indicates that the structure of modified GOx was retained when compared to pristine GOx. The far UV CD of 1 – 3 μM GOx analyzed in 20 mM PIPES at pH 7 with a path length of 0.05 cm and normalized to molar concentration of the protein, showed peaks corresponding to α-helices (double minima at 210 nm and 220 nm), and β-sheets at 190 nm (**Figure 3A**). The CD spectra of GOx(+45) (red curve) was comparable to that of GOx (blue curve), under the same conditions of path length, buffer, and normalized with respect to enzyme concentration, and all spectra were corrected routinely for any baseline changes. The molar ellipticities of the modified enzymes

(GOx(n)) were less than that of GOx at 210-220 nm region (**Figure 3A**, inset). However, GOx(n) molar ellipticities at the 210-220 minima were within the range of 87% to 96% of unmodified GOx (**Figure 4A**), indicating GOx(n) structure retention comparable to that of GOx.

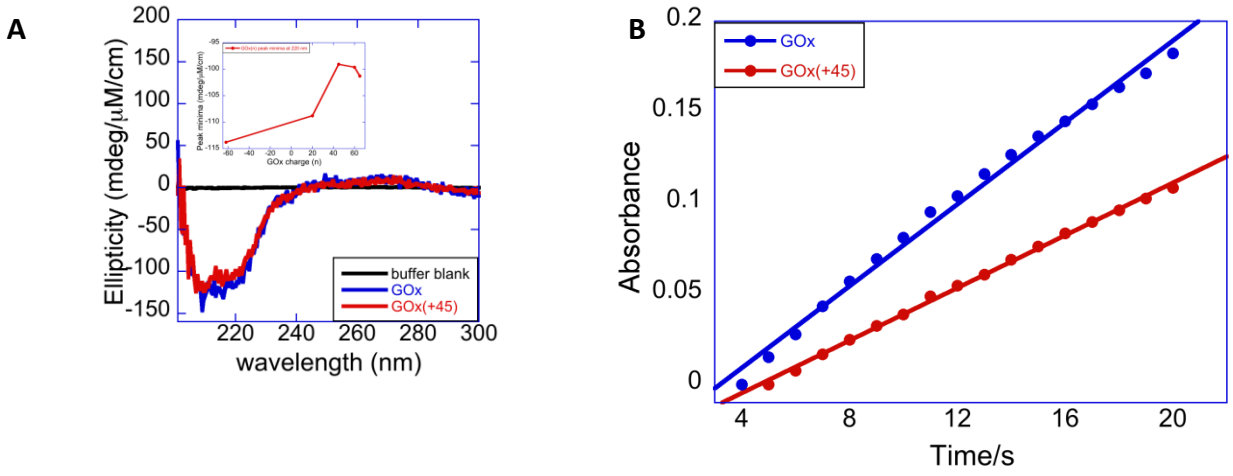

Figure 2.3. Circular dichnroism and activity of GOx(+45). (A) The effect on structure retention due to GOx modification with TETA was assessed for GOx(+45) (red curve). There was no significnant loss in protein structure when compared to pristine GOx (blue curve). GOx(+45) indicated signal intensity comparable to that of GOx(blue curve). (B) Initial activity due to GOx modification. GOx(+45) (red line) showed reduction in initial rate 23% when compared to GOx.

Glucose oxidase activities of GOx(+45) when compared to unmodified GOx (**Figure 3B**) was quantified by minor modification of the standard assay[46] with D-glucose as the substrate and kinetic curves of product formation from GOx(n) have been compared with that of pristine GOx (**Figure 4**). Glucose oxidase reacts with D-glucose to form gluconic acid and GOx coenzyme, flavin adenine dinucleotide (FAD) is reduced during the reaction to form $FADH_2$. In the presence of oxygen, $FADH_2$ is oxidized to yield FAD and peroxide (H_2O_2). Guaiacol oxidation by H_2O_2 is catalyzed by horseradish peroxidase (HRP) to form a colored product that was monitored as a function of time (**Figures 3B and 4B**), at room temperature of 25 ˚C and absorption maximum of 470 nm. Analysis of the first ~20 points (linear portion of the kinetic trace) of GOx(+45) (**Figure 3B**, red line) yielded an initial rate that was reduced by 23% when compared to unmodified GOx (blue line) and an initial rate reduction of 33.5% was observed for GOx(+20) (**Figure 4B**, black line) when compared to unmodified GOx. However, GOx(+60) (**Figure 4B**, orange line) and GOx(+65) (**Figure 4B**, green line) yielded reduced initial rates of 51% and 61% respectively when compared to GOx suggesting that amine conjugation has a negative effect on the GOx active site. This could be due to some loss in the structure around the active site and/or partial blockage of the active site after chemical modification. The slope of the linear portion of a kinetic trace of absorbance vs time was normalized by sample concentration (1 – 3 μM) and the resulting value was used as an estimation of the initial rate. Notably, GOx modification had no effect on structure retention (**Figure 3A**) suggesting that although there was some loss in GOx activity due to modification, GOx structure remained intact. Next we examined the binding of a few GOx(n) derivatives with α-ZrP nanosheets by isothermal titration calorimetry to gain some understanding of how GOx charge influenced the binding thermodynamics.

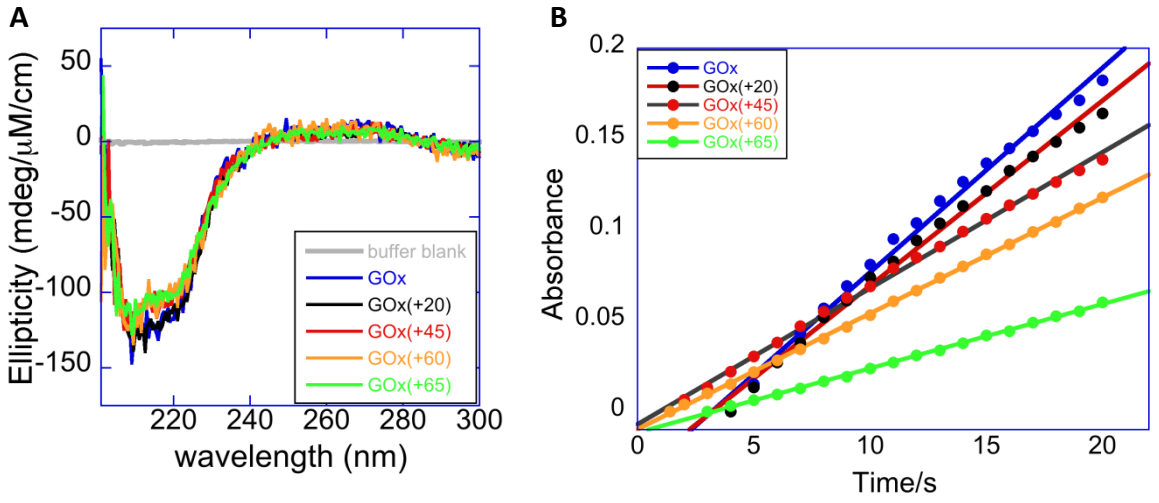

Figure 2.4. Circular dichnroism and activity of GOx(n). (A) The effect on structure retention due to GOx modification with TETA was assessed over a range of GOx(n) charges from +20 to +65. There was no significnant loss in protein structure when compared to pristine GOx (blue curve). GOx(n) for n = +20 (black curve), +45 (red curve), +60 (orange curve), and +65 (green curve) indicated signal intensity comparable to that of GOx(blue curve). (B) Initial activity due to GOx modification. GOx(+20) (red line) and GOx(+45) (black line) showed rections in initial rates by 34% and 23% respectively when compared to GOx. However, GOx(+60) (orange line) and GOx(+65) (green line) yielded initial rates that were less than 50% of GOx initial rate.

2.4.4. ***Isothermal Titration Calorimetry:*** The binding of GOx and three examples of GOx(n) to α-ZrP nanosheets (n = -20, + 25 and +30) was directly monitored by ITC, at 25˚C (20 mM NaPIPES buffer at pH 7.0, **Figure 5**). Addition of a solution of GOx(n) (30 – 100 μM) from the automated syringe to an exfoliated suspension of α-ZrP (6 mM, 20 mM NaPIPES buffer at pH 7.0) in the calorimeter resulted in heat release. For example, 6 mM α-ZrP was titrated with 30 μM GOx(-20) by adding aliquots of 8 μL protein solution to α-ZrP suspension at 300 s intervals for a total of 30 injections and the heat absorbed or released has been recorded. An exothermic response was observed with a plateau (**Figure 5A**, blue lines). The dilution curves, representing the heat absorbed when protein solution in the syringe was injected into the calorimeter cell that was filled with buffer solution instead of α-ZrP solution (**Figure 5A**, 6 red lines) were offset from the titration by 5 μcal/mol for clarity. The dilution data were subtracted from the titration data to obtain the corresponding corrected thermograms (**Figure 5A**, 6 blue lines) that showed a net heat loss during the binding phase (about 2000 s), indicating strongly exothermic binding. The binding of anionic GOx(-20) to the anionic α-ZrP surface can be explained by the ICPB model (**Scheme 2B**) such that cations are sequestered to the binding interface to facilitate charge neutralization and enthalpic binding is driven by this sequestration. The integrated enthalpy data were fitted to a single set of indistinguishable, non-cooperative binding sites model (**Figure 5B** solid curves, equation 1)[36,44] Fits to the data were iterated to minimize chi-square and to optimize agreement between observed and predicted curves. Each fit represents a global minimum that was obtained from multiple fits that were performed with different initial values of K_b, n and ΔH. Standard equations of thermodynamics were used to calculate ΔS and ΔG.

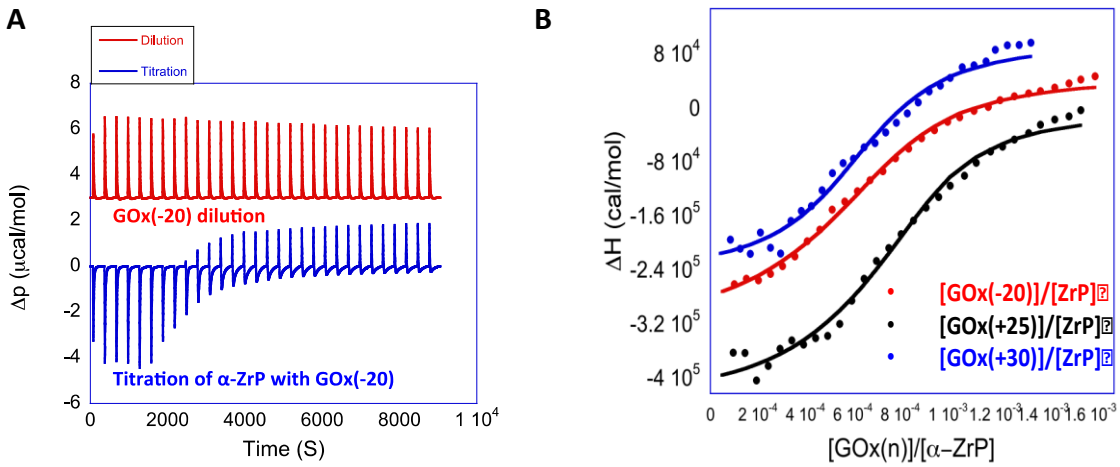

Figure 2.5. Isothermal titration calorimetry data for the titration GOx(n) into α-ZrP, in 20 mM NaPIPES buffer at pH 7.0. (A) The thermogram obtained by the addition of 61 μM GOx(-20) solution to 6 mM α-ZrP (blue curve), and the dilution data (red curve) which is off set from the titration for clarity. (B) Integrated heat as a function of the molar ratio of GOx(-20), GOx(+25), or GOx(+30) to α-ZrP. The red, black, or blue line is the best fit to the data according to the single, identical, non-interacting binding site model. Data are an average of three measurements and the GOx(-20) and G0x(+30) curves have been offset for clarity.

Interaction of GOx(+25) (**Figure 5B**, black curve) or GOx(+30) (red curve) with α-ZrP showed binding similar to that of GOx(-20)/α-ZrP (red curve). The best fit to the data (**Figure 5B, Table 1**) indicated a ΔH of (-371.3 ± 52.8) kcal/mol, a ΔS of (-1.2 ± 0.2) kcal/mol, a binding constant (K_b) of ((2.1 ± 0.6) x 10^6) M^{-1}, and ΔG of (-8.6 ± 1.8) kcal/mol for GOx(-20) and similar values were obtained for GOx(+25) and GOx(+30) (**Figure 5B**, GOx(-20) and GOx(+30) curves have been offset for clarity). The integrated enthalpy change due to each addition of GOx(n) solution to α-ZrP was plotted as a function of the ratio of concentrations of GOx(n) to α-ZrP (**Figure 3B**, dotted curves). Furthermore, The ICPB model suggests that binding of cationic GOx(+25) and GOx(+30) to α-ZrP nanosheets is entropy driven due to cation release (**Scheme 2A**). However, enthalpic binding was observed here suggesting that factors other than charge neutralization and electrostatics are involved. For example, the type of solvent ions and buffering effects add complexity to the enthalpy change associated with protein/ZrP interactions.[36]

Titration of α-ZrP with a solution of pristine GOx, under the same conditions as above (**Figure 6E**) revealed that there was no detectable binding, supporting the hypothesis that GOx conjugation to TETA facilitated enzyme interaction with the nanosheets. A minimum number of TETAs may be required to tether the protein to the negatively charged phosphates on the surface of the α-ZrP nanosheets. This hypothesis is supported by the large increase in the binding constant from 0 M^{-1} (pristine GOx, **Table 1**) to (2.1 x 10^6) M^{-1} for GOx(-20)/α-ZrP.

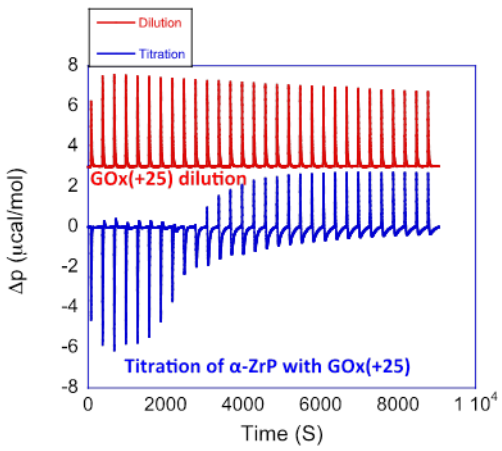
Dilution
Titration
GOx(+25) dilution
Titration of α-ZrP with GOx(+25)
Δp (µcal/mol)
Time (S)

A

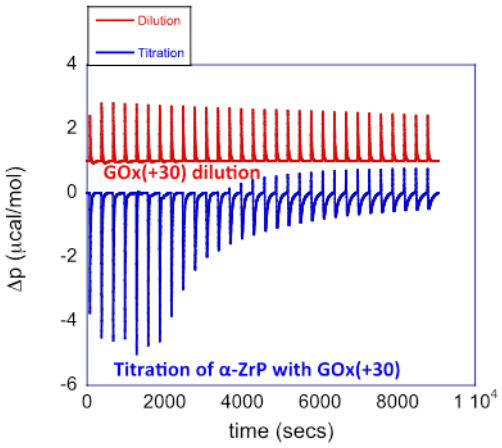
Dilution
Titration
GOx(+30) dilution
Titration of α-ZrP with GOx(+30)
Δp (µcal/mol)
time (secs)

B

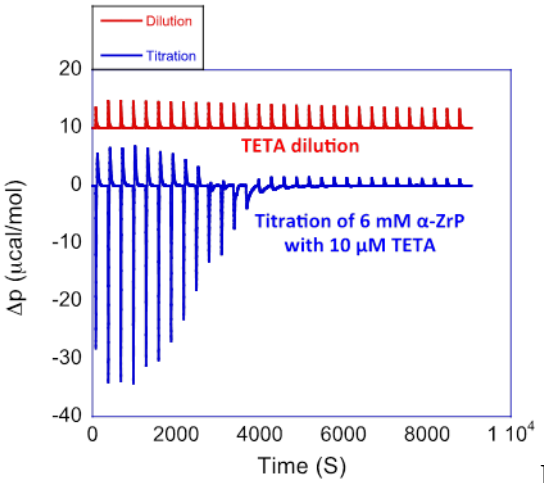
Dilution
Titration
TETA dilution
Titration of 6 mM α-ZrP
with 10 µM TETA
Δp (µcal/mol)
Time (S)

C

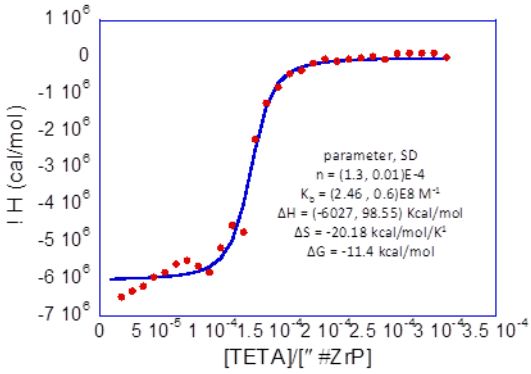
parameter, SD
n = (1.3, 0.01)E-4
K_b = (2.46 , 0.6)E8 M⁻¹
ΔH = (-6027, 98.55) Kcal/mol
ΔS = -20.18 kcal/mol/K¹
ΔG = -11.4 kcal/mol
[TETA]/[" ≠ZrP]

D

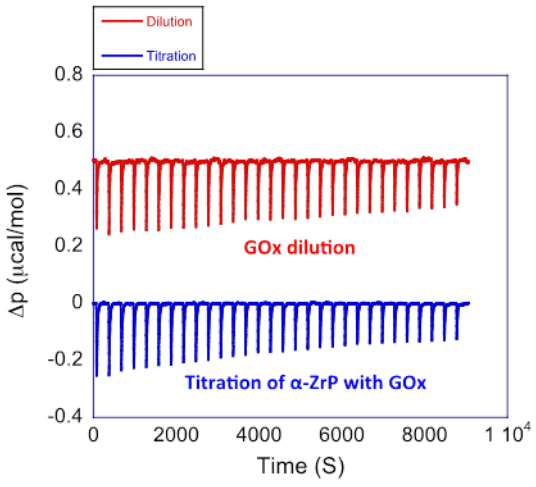
Dilution
Titration
GOx dilution
Titration of α-ZrP with GOx
Δp (µcal/mol)
Time (S)

E

Figure 2.6. Isothermal titration calorimetry data at 25˚C for the addition of 61 μM GOx(25) or GOx(+30) (A, B) to 6 mM α-ZrP in 20 mM NaPIPES buffer at pH 7.0. The dilution thermogram obtained by the addition of protein to buffer solution (red curves) was subtracted from the total thermogram of the addition of protein to α-ZrP in buffer to yield the net GOx(n)/α-ZrP thermograms (blue curves), and the dilution data is off set from the titration thermogram. (C) Dilution thermogram (red curve) and titration thermogram (blue curve) of TETA addition to α-ZrP. (D) Integrated heat as a function of the molar ratio of TETA to α-ZrP. The blue line is the best fit to the data according to the single, identical, non-interacting binding site model. (E) ITC analysis revealed that there was no interaction between pristine GOx and α-ZrP.

Table 2.1. Thermodynamic parameters determined for the binding of GOx(n) to α-ZrP at 25 ˚C in 20 mM NaPIPES buffer at pH 7.0 (first four rows) and for TETA to calf thymus DNA (last row)

GOx(n) charge (± 5)	K_b x 10^b (M^{-1})	TΔS (kcal/mol)	ΔH (kcal/mol)	ΔG (kcal/mol)
GOx (pristine)	0	0	0	0
-20	2.1 ± 0.6	-357.6 ± 59.6	-371.3 ± 52.8	-8.6 ± 1.8
+25	3.8 ± 2.8	-417.2 ± 29.8	-427.2 ± 39.0	-9.0 ± 2.8
+30	3.4 ± 1.1	-268.2 ± 59.6	-277 ± 57.4	-8.9 ± 2.5
TETA	246 ± 60	-6013.6	-6027 ± 98.6	-11.4

Each of the data sets (**Table 1**) represents an average of three separate titrations, thus the error for each parameter is an average of three measurements.

The large favorable enthalpic changes observed in this study were nearly equal and opposite in magnitude to the large unfavorable entropic decreases (**Table 1**). Changes in ΔG due to GOx(n) binding α-ZrP were insignificant because the ΔS and ΔH terms, as a function of charge, nearly cancelled out each other. This kind of balancing has been characterized as enthalpy-entropy compensation and has been widely discussed in enzyme binding to solid surfaces or protein binding to DNA.[54, 55, 56] The robust thermodynamic effect as a result of GOx modification suggests that amines contribute significantly to enthalpy-entropy compensation. In fact, when water molecules bound to aquacobalamin were replaced by amines, enthalpy-entropy compensation was observed.[57] Furthermore, the large magnitude of enthalpic changes observed in this study (ΔH and ΔS in the range of 100s kcal/mol) is probably due to the high affinity of TETA for the α-ZrP nanosheets as observed from the binding data of TETA/α-ZrP (**Table 1**, last row) where a binding constant in the range of 10^8 M^{-1} is reported.

2.4.5. ***Surface Plasmon Resonance:*** In a typical SPR experiment, a gold chip mounted on a prism (**Scheme 4**) generates oscillations of electron density when incident light from the prism is reflected. The resulting plasmons are quasiparticles that create waves above the gold surface such that alteration of the surface refractive index due to association and dissociation of GOx(n) on the α-ZrP coated gold surface can be monitored. A detector develops a SPR response vs time signal based on the angle of light reflected from the prism. A thin film of α-ZrP was spin coated onto the surface of the SPR gold chip before mounting in the flow channel where the enzyme (GOx(n)) sample is introduced via an inlet and excess sample exits via an outlet. A flow rate of 25μL/min was used to flow through appropriate concentrations of GOx(n) in 20 mM PIPES

buffer, pH 7 that interacted with α-ZrP on the surface of the gold chip and created SPR signals. As an example, the increase in signal corresponding to association of increasing concentrations of GOx(+20) (31.25 nM , 62.5 nM, 125 nM, 250 nM, and 500 nM) with the negatively charged α-ZrP solid surface and equilibrium was observed at about 4 to 6 minutes (**Figure 7A**). At this point, the system was switched to buffer (without protein) to trace the dissociation kinetics (data not shown) and a flat line in the reference channel was observed, which confirms that a flow through of PIPES buffer alone did not interact with α-ZrP. The variation of GOx(n) concentration was facilitated by the regeneration of the α-ZrP coated surface with 0.05% sodium hydroxide (NaOH) for 30 s. A similar SPR response to variation of GOx(n) concentration on the α-ZrP coated sensor was observed for values of n = +20 (**Figure 8A**), +45 (**Figure 8B**), +60 (**Figure 8C**), and +65 (**Figure 8D**).

Scheme 2.4. Surface plasmon resonance (SPR) experimental setup showing cationic protein (GOx(n)) binding to exfoliated α-ZrP sensor chip. The GOx(n) solution is flowed over the exfoliated α-ZrP sensor chip using a syringe pump that introduces sample via the inlet. The entire sensor assembly including flow cell and excess sample outlet is mounted on a prism that receives incident light (lamp). Development of The SPR signal (SPR response vs time) by the detector is based on the angle of reflected light.

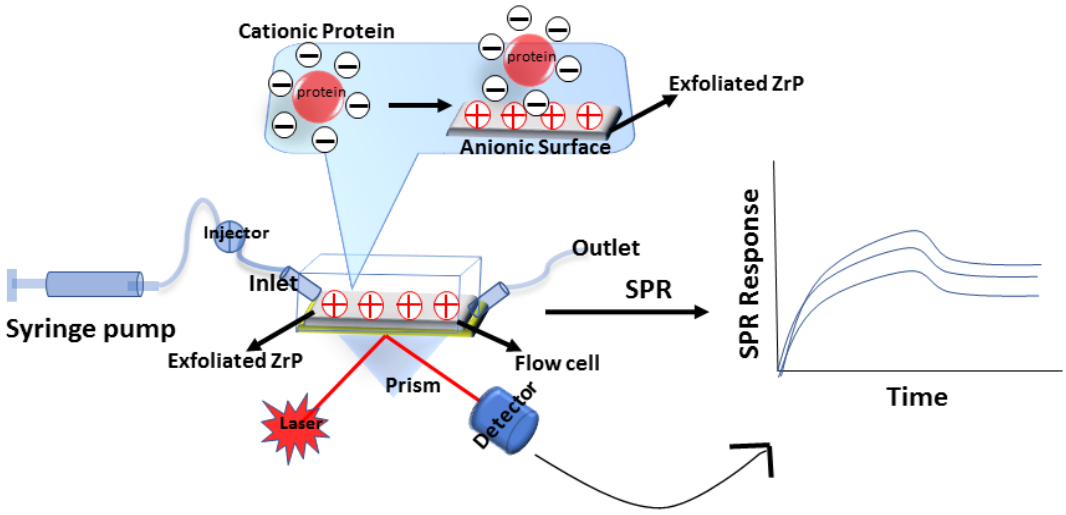

The real time SPR experimental data of GOx(n)/α-ZrP on rates (k_{on}) and off rates (k_{off}) kinetic traces were deconvoluted with a 1:1 equilibrium binding model to yield the affinity constants, on rates, and off rates. The individual rate constants for association (k_{on}), dissociation rate constant (k_{off}), equilibrium dissociation (K_D), and binding constants (K_b) were tabulated in Table 2. The degree of affinity (binding constants, (K_b)) was calculated as a ratio of on to off rate constants.

A plot of equilibrium binding constant (K_b) against various GOx(n) charges (**Figure 7B**) resulted in a significantly linear relationship where n = +20, +30, +45, +60, and +65. ITC determined binding constants for values of n = -62 and n = -20 did not fit the SPR linear correlation plot suggesting a charge threshold at n = +20 where binding increases linearly with increasing values of n. Unmodified GOx did not show any binding with α-ZrP solid surface suggesting that amines facilitate binding of GOx. Furthermore, the SPR binding constants observed here (**Table 2**) are an order of magnitude higher than those reported for ITC measurements (**Table 1**). This suggests a correlative relationship between the value of n (GOx(n) net charge) and binding constant since ITC measurements were in the range of n = -20 to n = +30 and SPR measurements were in the range of n = +20 to n = +65. Together, these data suggests a minimum number of amines required for GOx(n)/α-ZrP association and that at a GOx(n) minimum charge of +20 and beyond a significantly linear relationship is observed between the value of n and GOx(n)/α-ZrP binding constant. Therefore, the role of electrostatics becomes increasingly dominant as the protein charge increases. Scanning electron micrographs (SEM) (scale bar 30 μm) of the α-ZrP sensor chip with one half uncoated (**Figure 7C**) indicated α-ZrP on gold (left) when compared to the bare gold surface (right). The weight percents of Zr, P, and

N were determined to be 15.57, 9.69, and 2.10 wt% respectively, indicating the immobilization of modified GOx on the α-ZrP surface. These measurements were determined from Energy-

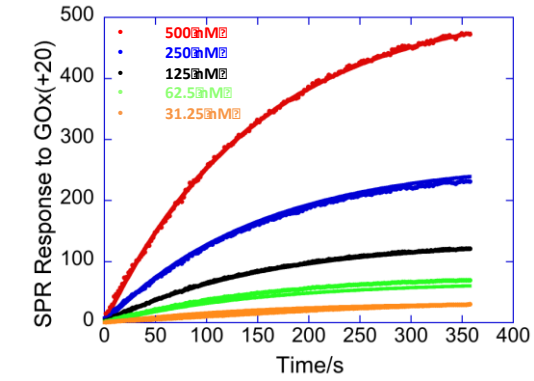

A

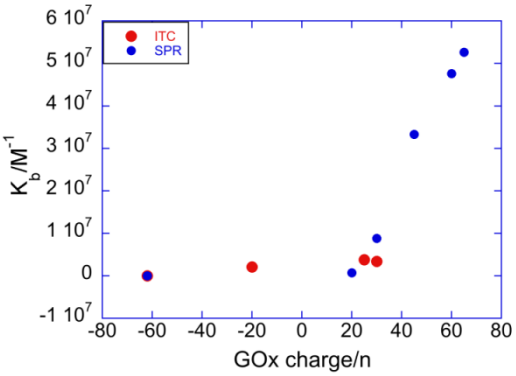

B

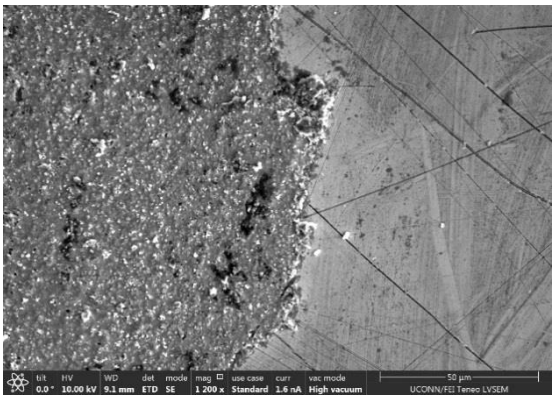

C

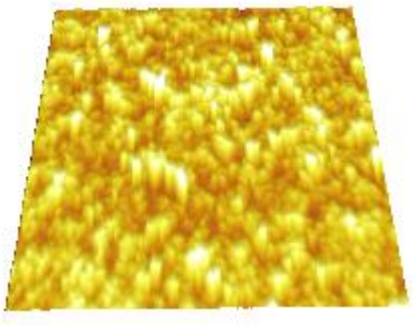

D

Figure 2.7. (A) Association (0–240 s) data for GOx(+20) on α-ZrP sensor chip at 25 µL min^{-1} (dotted line, experimental data; solid line, simulated fit) showing SPR response to increasing GOx(+20 concentrations of 31.25 nM, 62.5 nM, 125 nM, 250 nM, and 500 nM) (B) Correlation plot of GOx(n) charge and binding constant (K_b) was determined by ITC (red dots) and SPR experimental data fitting (blue dots). (C) Scanning electron micrographs (scale bar 30 µm) of α-ZrP sensor chip with one half uncoated. (D) AFM topography of α-ZrP sensor both in 2D and

3D view and the calculated film roughness was 191.22nm (± 47.36).

dispersive X-ray spectroscopy (EDX) analysis (**Figure 8E**) after flowing GOx(+60) on the α-ZrP sensor chip. An Atomic-force microscopy (AFM) image of the α-ZrP coated gold sensor in 3D views (**Figure 7D**) shows the topography that indicates α-ZrP nanoplates bound to the surface of the gold chip and the calculated roughness was estimated to be 191.22 nm (± 47.36).

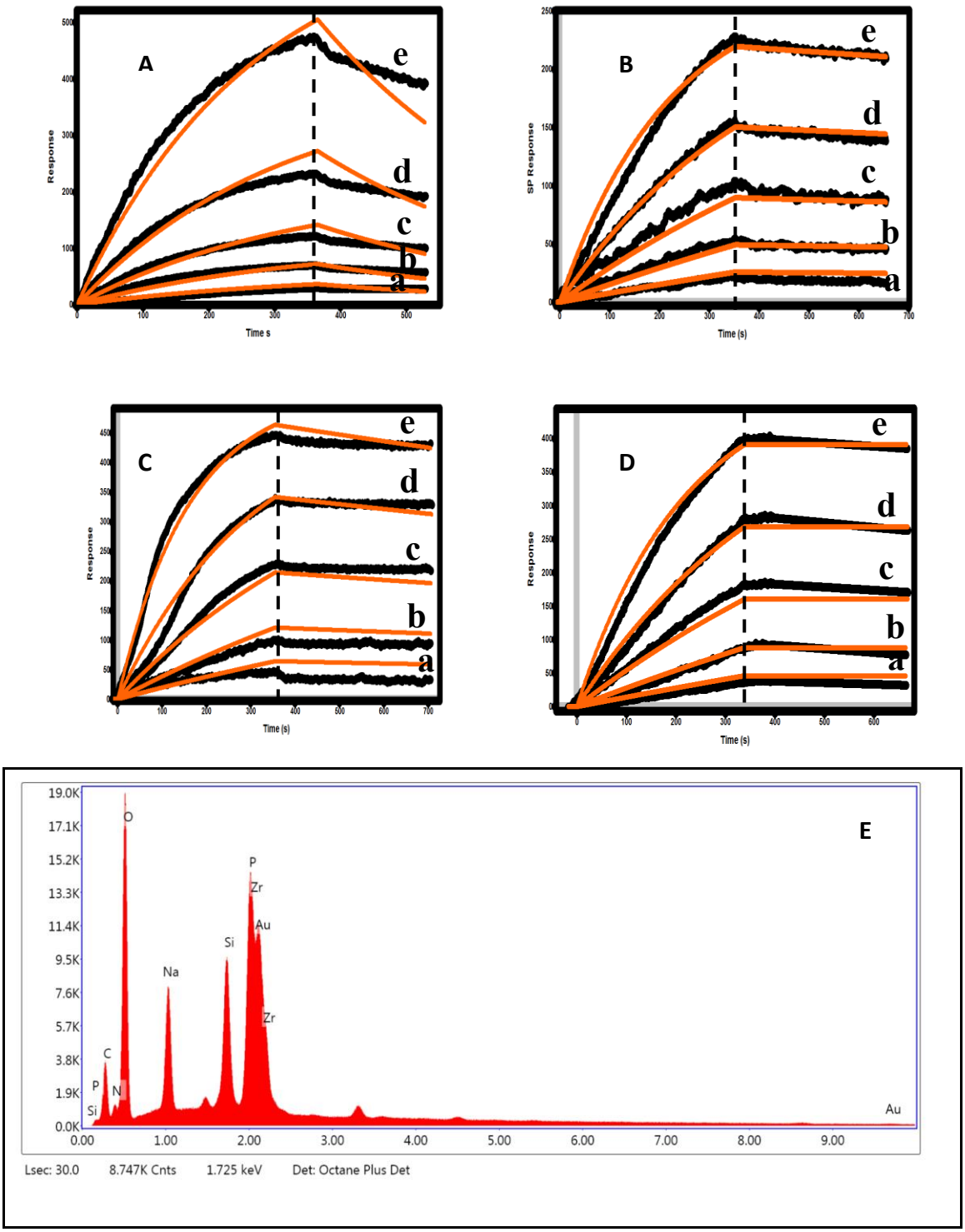

Figure 2.8. GOx(n) SPR binding kinetic data fitting for (A) n = +20, (B) n = +45, (C) n = +60, and (D) n = +65. The vertical dashed line shows the time point where buffer was

switched on. The SPR experimental data (black line), and the simulated fit (red line) for GOx(n) concentrations of a, 31.25 nM; b, 62.5 nM; c, 125 nM; d, 250 nM; and e, 500 nM indicates the increase in SPR response with increasing concentration. (E) EDX analysis after flowing GOx(+60) on the α-ZrP sensor chip measured Zr, P and N content of 15.57, 9.69, and 2.10 wt% respectively, indicating the immobilization of modified GOx on the α-ZrP surface.

Table 2.2.

SPR determined variation of kinetic parameters with GOx charge (n).

GOx charge (n)	k_{on} x 10^{3} ($M^{-1}s^{-1}$)	k_{off} x 10^{-4} (s^{-1})	K_D x 10^{-8} (M)	K_b x 10^{7} (M^{-1})
+20	2.1	27.5	133	0.08
+30	5.1	5.7	11.3	0.88
+45	8.8	2.7	3.0	3.3
+60	11.9	2.5	2.1	4.8
+65	9.0	1.6	1.8	5.6
GOx	0	0	0	0

2.4.6. ***Zeta Potential titrations:*** Zeta potential was used to monitor change in surface potentials as enzyme binding progressed. Zeta potential quantifies the difference in potential between a particle surface and the solvent. According to the proposed ICPB enzyme-binding model (**Scheme 2**), the surface potential of the nanosheets after binding of the enzyme is expected to include the charge contributions due to the uptake or release of counter ions to/from the enzyme-solid interface. Our hypothesis is that when GOx(n) derivatives bind to α-ZrP, the overall surface potential will be affected by four factors: the extent of enzyme binding, enzyme charge, charge on the nanosheets, and the involvement of ions in the binding mechanism to maintain charge-neutrality of the enzyme-ZrP interface. For example, in the case of GOx(-40) binding to α-ZrP, sequestration of cations at the binding

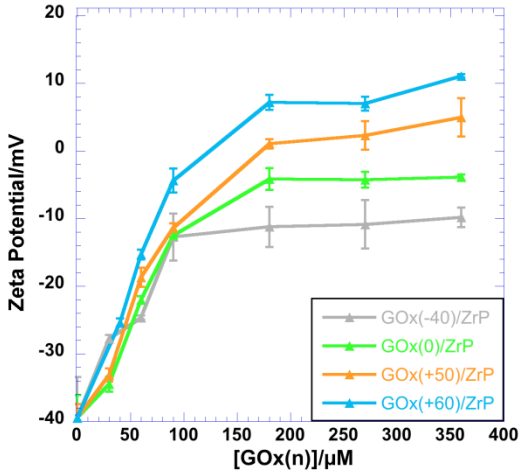

Figure 2.9. Zeta potential titration of α-ZrP (3 mM) with GOx(n) at 25 °C in 20 mM PIPES buffer, pH 7.0. GOx charge (n) was varied from -40 to +60 as marked. In each case, the charge gradually increased from -40 and reached a plateau.

interface (**Scheme 2B**) is expected in order to neutralize the charge buildup and facilitate GOx(-40)/α-ZrP interaction.

Binding of anionic GOx(n) (n < 0) to anionic nanosheets of exfoliated α-ZrP is normally expected to be unfavorable, and carry a net negative charge, but the involvement of cations in the neutralization of the interface between the anionic enzyme and the anionic nanosheet is expected to change the charge balance. Thus, net surface potential observed would be different from the sum of surface potentials of the enzyme and the nanosheets. We expected an increase in charge due to the binding of anionic protein to the anionic nanosheets and this has been the case (**Figure 9**) for n values of -40 (gray curve) and -2 (green curve). When 3 mM α-ZrP was titrated with increasing concentrations of GOx(n), there was an increase in net charge. The net charge increased from -40 to -10 when GOx(-40) was titrated with α-ZrP which clearly demonstrated the sequestration of cations as the enzyme binding progressed, in support of the ICPB mechanism.

Binding of cationic protein to the anionic solid increased the net charge because of charge neutralization of the oppositely charged entities. Plateau was reached after the addition of > 100 μM GOx(n) (**Figure 9**) for n values of -40, 0, +50, and +60 (gray, green, orange, and blue curves respectively). The plateau position increased with increasing enzyme charge, which provided direct evidence for enzyme binding to the nanosheets. Another interesting observation was that the plateaus occurred either below or above neutral charge (0), which suggests that sequestration or release of ions during binding is not complete, and there always is some residual charge. This is entirely consistent with the polyelectrolyte theory where the condensation of counter ions at a charged surface is never complete.[58]

2.4.7. ***Circular Dichroism Studies of GOx(n)/α-ZrP:*** The secondary structure of GOx(n)/α-ZrP biocatalysts were assessed by CD spectroscopy and compared to the CD spectra of pristine GOx using 1 – 3 μM protein analyzed in 20 mM PIPES at pH 7. The spectral shape of the GOx(+45) bound to α-ZrP (GOx(+45)/α-ZrP **Figure 10A**, red curve) was comparable to that of unmodified GOx (**Figure 10A**, blue curve), indicating structure retention of GOx(+45) after its complex formation with α-ZrP. The same trend was observed for all modified enzymes bound to α-ZrP for values of n between +20 and +65 (GOx(n)/α-ZrP **Figure 11A**) However, there was some variability in signal intensity at the 220 nm minimum (**Figure 11B**). While GOx/α-ZrP (brown bar) and GOx(+65)/α-ZrP (green bar) showed

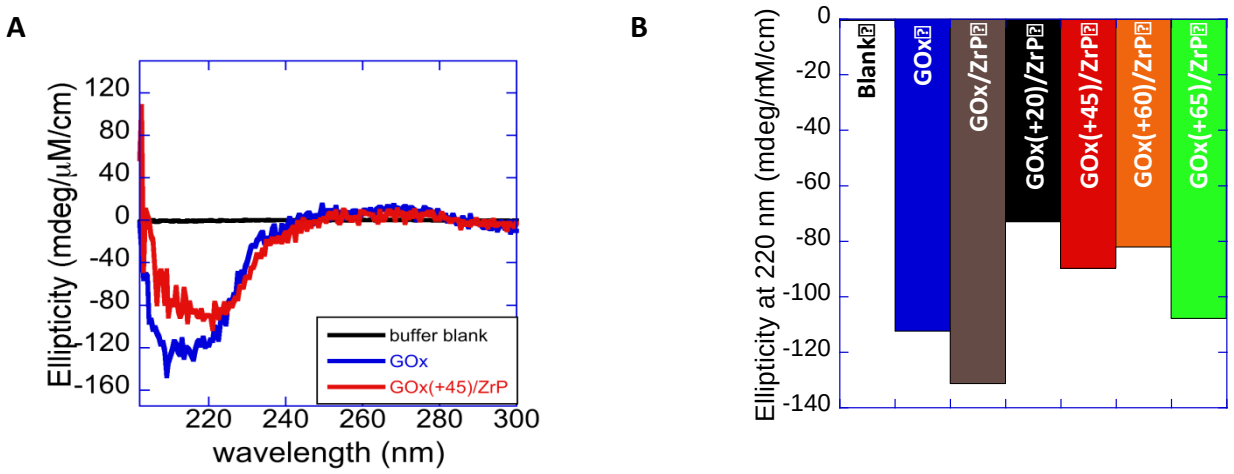

Figure 2.10. Circular dichroism spectra of GOx(n)/α-ZrP when compared to GOx (A) Circular Dichroism spectra of GOx (blue) and GOx(+45)/ZrP (black). GOx α-helical structure is retained after GOx conjugation to TETA and complex formation with α-ZrP to yield GOx(+45)/α-ZrP. (B) Randomness in peak intensity was observed at the 220 nm minimum when compared to GOx (blue bar). GOx/α-ZrP (brown bar) and GOx(+65)/α-ZrP (green bar) showed comparable intensities, but GOx(+20)/α-ZrP (black bar), GOx(+45)/α-ZrP (red bar), and GOx(+60)/α-ZrP (orange bar) showed variably reduced intensities at the 220 minimum when compared to pristine GOx.

comparable intensities to unmodified GOx (blue bar), GOx(+20)/α-ZrP (black bar), GOx(+45)/α-ZrP (red bar), and GOx(+60)/α-ZrP (orange bar) showed reductions at the 220 nm peak minimum by 35%, 20%, and 27% respectively. These reductions were observed to the same degree when compared to either the CD spectra of unmodified GOx or the unbound modified GOx analogs (GOx(n)) suggesting that signal intensity may have vary due to the randomness of amine attachment to the enzyme surface. The electrostatic landscape of a given GOx(n) conjugate may be one of variable charge patches instead of a uniform distribution of charge and this may have variable effects on CD signal intensity.

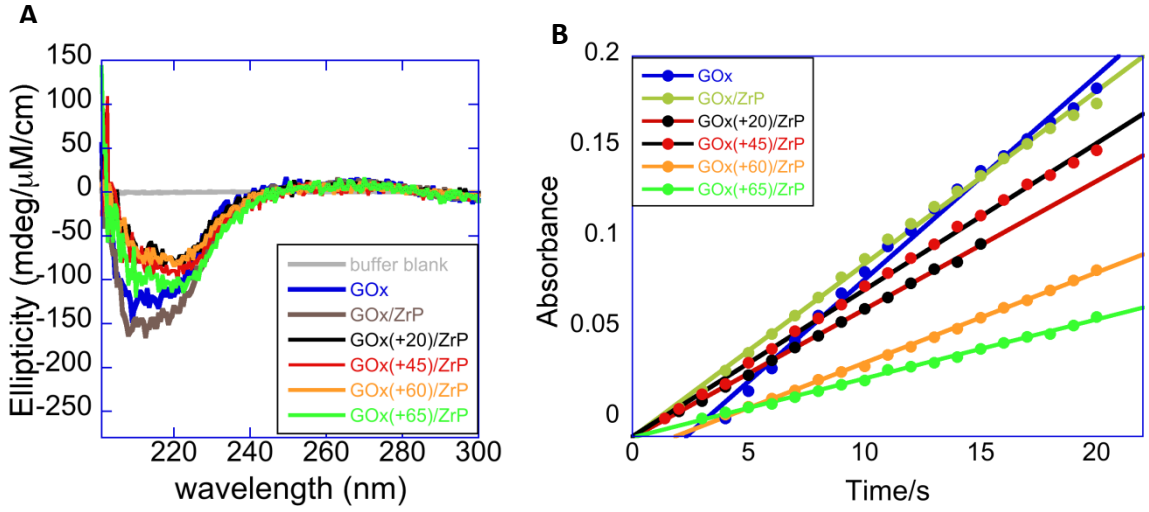
A
150
100
50
0
-50
-100
-150
-200
-250
Ellipticity (mdeg/μM/cm)
220
240
260
280
300
wavelength (nm)
buffer blank
GOx
GOx/ZrP
GOx(+20)/ZrP
GOx(+45)/ZrP
GOx(+60)/ZrP
GOx(+65)/ZrP
B
0.2
0.15
0.1
0.05
0
Absorbance
0
5
10
15
20
Time/s
GOx
GOx/ZrP
GOx(+20)/ZrP
GOx(+45)/ZrP
GOx(+60)/ZrP
GOx(+65)/ZrP

Figure 2.11. Circular dichroism and activity of GOx(n)/α-ZrP. (A) The effect on structure retention due to GOx(n) complex formation with α-ZrP (GOx(n)/α-ZrP) was assessed over a range of GOx(n) charges from +20 to +65. There was no significnant loss in protein structure when compared to pristine GOx (blue curve). However, randomness in peak intensity was observed at the 220 nm minimum when compared to GOx (blue bar). GOx/α-ZrP (brown curve) and GOx(+65)/α-ZrP (green curve) showed comparable intensities, but GOx(+20)/α-ZrP (black curve), GOx(+45)/α-ZrP (red curve), and GOx(+60)/α-ZrP (orange curve) showed variably reduced intensities at the 220 minimum when compared to pristine GOx. (B) Plot of absorbance values showing activity of GOx(n) bound to α-ZrP. Unmodified GOx bound to α-ZrP (blue-gray line) showed initial activity comparable to unbound GOx and the initial activities of bound GOx(n) were comparable to the corresponding unbound GOx(n) although there was variable loss in activity when compared to unmodified GOx. Samples were analyzed in NaPIPES buffer at pH 7.0. A solution of D-glucose (4 μM) was added to a mixture of GOx (1 μM), horseradish peroxidase (HRP, 0.4 μM) in 10 mM NaPIPES buffer pH 7.2 and guaiacol (o-methoxyphenol) (800 μM) dissolved in DI water. Oxidation of the substrate, guaiacol to a dimeric product that has an absorption maximum at 470 nm was monitored as a function of time at room temperature (25 ˚C).

2.4.8. ***Activities of GOx(n)/α-ZrP biocatalysts:*** We tested the effect of binding to α-ZrP on the activities of the GOx(n) analogs and found that activities of the bound enzymes (GOx(n)/α-ZrP, **Figure 12A** even numbered bars) were comparable to activities of the unbound analogs (GOx(n), **Figure 12A** odd numbered bars) under the same conditions of pH, ionic strength, buffer and temperature. This suggests that enzyme/ZrP interaction has no effect on enzyme activity, a promising result for biocatalysis applications.

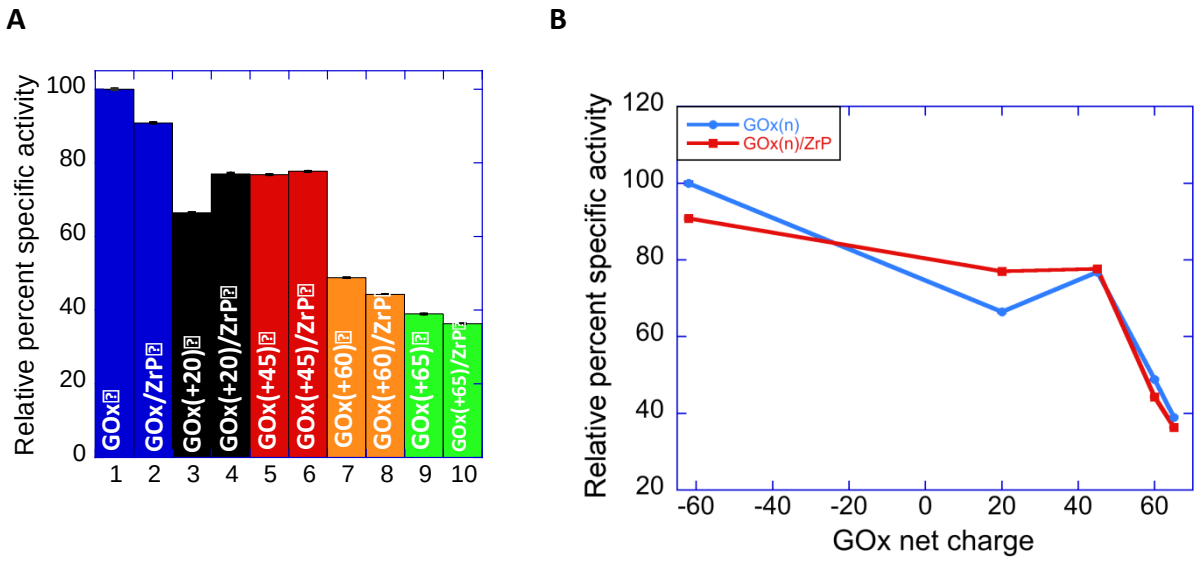

Figure 2.12. Activities of GOx(n) after complex formation with α-ZrP (GOx(n)/α-ZrP). (A) Relative percent specific activities of GOx(+20)/α-ZrP (black bar #4), GOx(+45)/α-ZrP (red bar #6), GOx(+60)/α-ZrP (orange bar #8), and GOx(+65)/α-ZrP (green bar #10) were comparable to those of the corresponding GOx(n) samples (odd numbered bars), under the same conditions of buffer, pH and temperature. However, with respect to unmodified GOx (blue bar #1), there was loss in activity due to chemical modification (odd numbered bars) that resulted in substantial reductions in the case of GOx(+60) and GOx(+65).

However, as discussed earlier, there was some loss in activity: 34% for GOx(+20) (black bar #3) and 23% for GOx(+45) (red bar #5), due to chemical modification. Furthermore, increased amine conjugation to GOx resulted in more than 50% loss in enzyme activity for GOx(+60) (orange bar #7) and GOx(+65) (green bar #9) suggesting that although amine modification is required to facilitate GOx interaction with α-ZrP, the total number of conjugated amines should be minimized to optimize retention of enzyme activity. Furthermore, as a function of net charge (n), the bound enzyme (**Figure 12B** red curve) showed decrease in activity when compared to the unbound enzyme (blue curve). Activity decreased from 91% in the case of the unmodifed enzyme/solid mixture (GOx/α-ZrP) to 77% for GOx(+20) and GOx(+45) bound to α-ZrP (GOx(+20)/α-ZrP and GOx(+45)/α-ZrP). A decrease in activity to less than 50% was observed for $n \geq +60$ suggesting a net protein charge treshold at which enzyme activity can be sustained while increasing amine conjugation. Initial rates and relative percent specific activity were determined from analysis of the linear portion (first 20 s) of kinetic traces of GOx(n)/α-ZrP (**Figure11B**).

2.5. Discussion

Pristine GOx does not bind to exfoliated α-ZrP plates but TETA conjugated to GOx facilitated the binding interaction due to at least two factors: 1. Enhanced favorable charge on the enzyme and 2. Direct interaction of the positively charged TETA side chains with the anionic phosphate lattice. Pristine GOx is negatively charged such that there is enough charge-charge repulsion at the interface with α-ZrP to inhibit any detectable interaction. However, introduction of a minimum number of positively charged amine side chains neutralizes enough negative charge on the GOx surface to drive the binding interaction. Specifically, given that two of the four TETA nitrogens are at optimal pKa for protonation at pH 7 and one of the four is neutralized upon

conjugation, it is expected that a total number of 14 TETA molecules will be attached to GOx to yield the GOx(-20) derivative. Therefore, a minimum of 14 TETA molecules is required to drive GOx(n)/α-ZrP interaction, suggesting that a minimum number of favorable interfacial coulombic contacts are required to overcome unfavorable interfacial charge-charge repulsion. Using similar calculations, a total number of 29 TETA molecules and about 31 TETA molecules will be attached to GOx to yield GOx(+25) and GOx(+30) respectively. However, increasing the number of interfacial coulombic contacts does not result in tighter binding (**Table 1**) suggesting that the increased number of TETA molecules beyond 14 molecules may attach external to the interface, away from the α-ZrP surface. The chemical modification of GOx-TETA derivatives reported here and other protein-TETA derivatives presented before[59,60,61,62,63,64] clearly indicate the potential for the control of enzyme intrinsic properties. Chemical modification of the protein or it's binding to α-ZrP did not affect secondary structure and GOx(n) activity was retained within the range of 66% to 77% when compared to unmodified GOx. However, when excessive modification was carried out, substantial loss in enzyme activity was observed although GOx(n)/α-ZrP complex formation did not affect activity for any value of n. The loss of more than half the activity due to modification in the case of GOx(+60) and GOx(+65) may be due to blockage or modification of the active site.

Binding of the GOx(n) derivatives to anionic α-ZrP has been enthalpy driven with an entropic penalty. Enthalpy driven binding has been observed when negatively charged proteins like hemoglobin or myoglobin interact with the negatively charged α-ZrP surface,[65] and entropy driven binding has been observed when positively charged proteins like lysozyme and cytochrome *c* bind α-ZrP.[66,67] In fact, these studies suggest a linear relationship between the net protein charge and the change in enthalpy (ΔH), with an increased ΔH that is correlative with

increasing protein charge. However, when hemoglobin was conjugated to increasing numbers of TETA side chains, to yield positively charged Hb-TETA derivatives, binding to negatively charged poly(acrylic acid) (PAA) was enthalpy driven, and there was a correlative increase in ΔH with increasing Hb-TETA charge.[68] This suggests a meaningful role for TETA at the binding interface, wherein the introduction of amine side chains is associated with enthalpy driven binding as observed in the studies reported here. This is supported by the decrease in enthalpy driven binding observed when ammonium chloride was conjugated to Hb instead of TETA,[68] and the highly enthalpic binding observed when unconjugated TETA binds α-ZrP nanosheets (**Figure 6 C, D**). Future studies that directly address the role of amines at the protein-solid interface, and the contribution of amines to the ICPB model will add clarity to the understanding of protein-solid binding thermodynamics studied here.

Interestingly, binding based on ITC studies is optimal when GOx charge is approximately +25 and the Gibbs free energy of binding between GOx and α-ZrP increased from 0 kcal/mol in the case of unmodified GOx to (-8.6 ± 1.8) kcal/mol when GOx was modified with TETA (GOx(-20), **Table 1**). When n = -20, binding was enthalpy driven with an entropic penalty and this is in agreement with the proposed ICPB mechanism regarding the binding of unmodified proteins to α-ZrP.[29,30] Binding of anionic enzyme to the anionic surface recruits cations to the interface to neutralize the excess negative charge that would accumulate otherwise. Thus binding is enthalpy driven at an entropic penalty when the cations are sequestered from the solvent. However, this could be a simplistic picture when the enzyme is functionalized with TETA side chains that show high affinities for binding to the anionic α-ZrP nanosheets. In fact, the increased number of TETA side chains adds complexity to the analysis of the binding data for n = +25 and +30 GOx(n) derivatives, discussed below.

The ICPB mechanism predicts that binding of oppositely charged partners releases counterions from both binding surfaces, since each surface functions as a counterion for the other surface. Binding, under these circumstances, would be under entropy control at an enthalpy penalty of removing counter ions from these charged surfaces. Clearly, this is not the case here with n = +25 and +30 and an additional factor dominates the binding thermodynamics. In addition to the factors predicted by the ICPB mechanism, the direct interaction of the TETA side chains with the phosphate lattice influences the binding thermodynamics. The nonlinear relationship between protein surface charge and binding data (**Figure 7B**) further supports this view point and suggests a complex set of additional factors in controlling the interfacial dynamics, but charge dominates, among these interactions. The Gibbs free energy of binding does not vary significantly in this set. Additionally, SPR analysis indicates a linear relationship between protein surface charge and the GOx(n)/α-ZrP binding constant for values of n between +20 and +65 suggesting that electrostatics related to increased number of TETA molecules may play an increasingly dominant role as the value on n increases.

Previously,[59] we reported a binding constant in the order of 10^7 M^{-1} for tetraethylenepentamine (TEPA) modified GOx binding to α-ZrP. This is an order of magnitude higher than the GOx(n)/α-ZrP binding constant observed here from ITC analysis, and the difference is probably due to the increased number of positive charge units per molecule of TEPA when compared to TETA. Furthermore, in this study we report a zero binding constant for GOx/α-ZrP compared to a binding constant in the order of 10^4 in our previous report.[59] This could be because ITC or SPR is not sensitive enough to fit low range binding data. We therefore assumed a binding constant of zero for GOx/α-ZrP, and the increased number of contacts

between GOx and α-ZrP, afforded by chemical modification were enough to drive favorable GOx(n)/α-ZrP interaction.

SPR determined binding constants (K_b) of GOx(n) interaction with α-ZrP are approximately an order of magnitude greater than ITC determined binding constants suggesting that GOx(n)/α-ZrP binding affinity is reduced in solution when compared to GOx(n) immobilized on the solid α-ZrP surface. This suggests that SPR provides a more sensitive platform for the quantitation of protein/α-ZrP binding affinity while ITC provides a comprehensive quantitation of thermodynamic parameters. Therefore, taken together, SPR and ITC studies broaden the range of thermodynamic and kinetic understanding of the GOx(n)/α-ZrP interaction. These comprehensive studies are necessary if the GOx(n)/α-ZrP platform has future applications in drug delivery and release. Additionally, highly sensitive SPR measurements facilitated analysis of low concentration and low volumes of GOx(n). The binding thermodynamics and kinetics reported here suggest the requirement of amine contacts to facilitate GOx(n)/α-ZrP interaction and SPR data indicates a linear relationship between GOx(n) charge and binding affinity for values of n ranging from + 20 to +65 with no association observed between unmodified GOx and α-ZrP (**Figure 5B**). ITC determined GOx(n)/α-ZrP binding constants for n values of -62 (unmodified GOx) and -20 did fit the linear SPR correlation plot. Therefore, taken together, binding constant analysis suggests a GOx(n)/α-ZrP binding threshold of n = +20, at which point the binding constant increases linearly with n. We recently reported a similar step binding function for the interaction of GOx(n) with DNA,[53] where a threshold GOx(n) charge of +30 was required to switch on binding. The difference in this study is that non-linear interaction occurs prior to the step threshold and this could be due to the difference between the rigidity and optimal charge density of the solid α-ZrP surface as opposed

to the flexible comparatively low charge density DNA backbone that may require a larger number of coulombic interfacial contacts for bending and/or wrapping around the protein.

Zirconium or zirconium phosphate based SPR studies have been reported. For example, zirconium phosphonate has been attached to the gold chip for immobilization of lipid bilayers for the biomimetic study of cell membranes,[69] and ZrP coated gold surfaces were used for laccase sensing.[70] Furthermore, phosphate adsorption unto gold has been characterized recently.[71] Taken together, these studies support the idea that ZrP on gold can be used as a SPR platform for enzyme sensing and this technique has been utilized in this study.

Zeta potential studies (**Figure 5**) revealed that at a GOx(n) charge of +50, the net charge of the GOx(+50)/α-ZrP complex is nearly 0 and implies that the enzyme/solid complex has equal numbers of oppositely charged ions, and this is not in contradiction with ICPB mechanism. The charge density due to phosphates per unit area of α-ZrP is known to be 1 charge/25 $Å^{2}$,[2] GOx(+50) binding α-ZrP should therefore result in charge neutrality. Using a sphere to model the glucose oxidase, we estimated that the sphere's cross-section is a reasonable maximum area of contact with a α-ZrP plate. We then calculated this circular area using glucose oxidase monomeric diameter of 55 $Å^{4}$ to be 2375 $Å^{2}$. Using this area, a net charge of +95 is required on glucose oxidase to match the aforementioned α-ZrP charge density. Therefore, the net charge of zero that is observed when GOx(+50) binds α-ZrP occurs due to sequestration of approximately +50 unit charge cations to the binding interface. This is in good agreement with the enthalpy driven binding observed here as a result of sequestration.

Circular dichroism findings reported here (**Figures 3, 4**) indicate structure retention of GOx after chemical modification and binding of the modified GOx(n) derivatives to α-ZrP. However, while the CD intensity of the GOx(+65)/α-ZrP complex was comparable to the

intensity of unmodified GOx, there was a reduction in intensities at the 220 nm minimum over the range of 20% - 35%. This could be due to the randomness in the location of the protein carboxyls that are modified. The protein/ZrP binding interface facilitated by amines that are evenly distributed throughout the protein surface may not affect CD signal intensity when compared to the binding interface facilitated by amines that are attached in charge patches on the surface. Regardless of the variability in intensity, the overall spectral shape of GOx after modification and interaction with α-ZrP was retained comparable to unmodified GOx, suggesting that protein modification and binding to the α-ZrP nanosheets did not affect protein structure.

GOx activity was not affected by interaction of modified enzyme (GOx(n)) with the α-ZrP nanosheets indicating that GOx can be immobilized on ZrP nanosheets for biocatalysis and biomedical device applications while preserving its activity. Novel platforms for the immobilization of GOx are currently being explored.[72] In this study, we have modified GOx to facilitate its binding to α-ZrP and we have quantified the thermodynamics of binding while GOxactivity was unaffected. These data will contribute to the understanding of the underlying mechanisms implicated in GOx immobilization.

2.6. Conclusion

Binding of GOx(n) to α-ZrP is an enthalpy driven process in the range of -277 kcal/mol to -427 kcal/mol with an entropic penalty in the range of -0.9 kcal/mol K to -1.4 kcal/molK. However, binding shows no significant change in Gibbs free energy (-9 kcal/mol) and that is most likely due to the enthalpy-entropy compensation phenomenon. The ΔH values observed here are an order of magnitude higher than those reported for Hb-TETA binding to poly(acrylic acid).[68] This is probably due to the increased amount of surface carboxyls available for conjugation to TETA

in the case of GOx when compared to the Hb surface. The increased dispersion of amines over the GOx surface may account for the decrease in counterion sequestration (overall increase in ΔH from n = -20 to n = +30) as amidation increases. In contrast, conjugated amines may be more concentrated in patches on the Hb surface, leaving large areas exposed to increasingly sequester counterions as amidation increases. SPR studies reveal a linear relationship between net GOx(n) charge and the GOx(n)/α-ZrP binding constant for values of n between +20 and +65 indicating a +20 charge threshold at which electrostatics dominate the binding interface. Thus, the continuous increase in binding energy was not noted in the entire range and the charge hypothesis is incorrect. Initial rates of the enzyme and its structure was not affected by complex formation with α-ZrP indicating that the GOx(n)/α-ZrP system has potential applications in biosensing, biocatalysis, and biomedical devices.

2.7. References

(1) Wang, S. G.; Zhang, Q.; Wang, R.; Yoon, S. F.; Ahn, J.; Yang, D. J.; Tian, J. Z.; Li, J. Q.; Zhou, Q. Multi-walled carbon nanotubes for the immobilization of enzyme in glucose biosensors. *Electrochem. Commun*. **2003**, 5, 800-803.

(2) Phadtare, S.; Kumar, A.; Vinod, V. P.; Dash, C.; Palaskar, D. V.; Rao, M.; Shukla, P. G.; Sivaram, S.; Sastry, M. Direct assembly of gold nanoparticle "shells" on polyurethane microsphere "cores" and their application as enzyme immobilization templates. *Chem. Mater*. **2003**, 15, 1944-1949.

(3) Zimmermann, S.; Fienbork, D.; Flounders, A. W.; Liepmann, D. In-device enzyme immobilization: wafer-level fabrication of an integrated glucose sensor. *Sensors and Actuators B: Chemical* **2004**, 99, 163-173.

(4) Kumar, C. V.; Chaudhari, A. Proteins immobilized at the galleries of layered α-Zirconium phosphate: Structure and activity studies. *J. Am. Chem. Soc*. **2000**, 122, 830-837.

(5) Bellezza, F.; Cipiciani, A.; Costantino, U.; Negozio, M. E., Zirconium phosphate and modified zirconium phosphates as supports of lipase. Preparation of the composites and activity of the supported enzyme. *Langmuir* **2002,** *18* (23), 8737-8742.

(6) Díaz, A.; David, A.; Pérez, R.; González, M. L.; Báez, A.; Wark, S. E.; Zhang, P.; Clearfield, A.; Colón, J. L., Nanoencapsulation of insulin into zirconium phosphate for oral delivery applications. *Biomacromolecules* **2010,** *11* (9), 2465-2470.

(7) Xu, S.; Whitin, J. C.; Yu, T. T.-S.; Zhou, H.; Sun, D.; Sue, H.-J.; Zou, H.; Cohen, H. J.; Zare, R. N., Capture of phosphopeptides using α-zirconium phosphate nanoplatelets. *Anal. Chem.* **2008,** *80* (14), 5542-5549.

(8) Foulds, N. C.; Lowe, C. R., Immobilization of glucose oxidase in ferrocene-modified pyrrole polymers. *Anal. Chem.* **1988,** *60* (22), 2473-2478.

(9) Malitesta, C.; Palmisano, F.; Torsi, L.; Zambonin, P. G., Glucose fast-response amperometric sensor based on glucose oxidase immobilized in an electropolymerized poly (o-phenylenediamine) film. *Anal. Chem.* **1990,** *62* (24), 2735-2740.

(10) Zhang, Q.; Wu, S.; Zhang, L.; Lu, J.; Verproot, F.; Liu, Y.; Xing, Z.; Li, J.; Song, X.-M., Fabrication of polymeric ionic liquid/graphene nanocomposite for glucose oxidase immobilization and direct electrochemistry. *Biosens. Bioelectron*. **2011,** *26* (5), 2632-2637.

(11) Fang, L.; Liu, B.; Liu, L.; Li, Y.; Huang, K.; Zhang, Q., Direct electrochemistry of glucose oxidase immobilized on Au nanoparticles-functionalized 3D hierarchically ZnO nanostructures and its application to bioelectrochemical glucose sensor. *Sensors and Actuators B: Chemical* **2016,** *222*, 1096-1102.

(12) Willner, I.; Katz, E.; Patolsky, F.; Bückmann, A. F. J. Biofuel cell based on glucose oxidase and microperoxidase-11 monolayer-functionalized electrodes. *Chem. Soc., Perkin Trans. 2* **1998**, 8, 1817-1822.

(13) Mano, N.; Mao, F.; Heller, A. A miniature biofuel cell operating in a physiological buffer. *J. Am. Chem. Soc*. **2002**, 124, 12962-12963.

(14) Fortier, G.; Brassard, E.; Belanger, D. Optimization of a polypyrrole glucose oxidase biosensor. *Biosens. Bioelectron*. **1990**, 5, 473-490.

(15) Gregg, B. A.; Heller, A. Cross-linked redox gels containing glucose oxidase for amperometric biosensor applications. *Anal. Chem.* **1990**, 62, 258-263.

(16) Kang, X.; Mai, Z.; Zou, X.; Cai, P.; Mo, J. A novel glucose biosensor based on immobilization of glucose oxidase in chitosan on a glassy carbon electrode modified with gold-platinum alloy nanoparticles/multiwall carbon nanotubes. *Anal. Biochem.* **2007**, 369, 71.

(17) Shan, C.; Yang, H.; Song, J.; Han, D.; Ivaska, A.; Niu, L. Direct electrochemistry of glucose oxidase and biosensing for glucose based on graphene. *Anal. Chem.* **2009**, 81, 2378-2382.

(18) Gibson, Q. H.; Swoboda, B. E. P.; Massey, V. Kinetics and mechanism of action of glucose oxidase. *J. Biol. Chem.* **1964**, 239, 3927-3934.

(19) Wohlfahrt, G.; Trivić, S.; Zeremski, J.; Peričin, D.; Leskovac, V. The chemical mechanism of action of glucose oxidase from Aspergillus niger. *Mol. Cell. Biochem.* **2004**, 260, 69-83.

(20) Fischel-Ghodsian, F.; Brown, L.; Mathiowitz, E.; Brandenburg, D.; Langer, R. Enzymatically controlled drug delivery. *Proc. Natl. Acad. Sci. U.S.A.* **1988**, 85, 2403-2406.

(21) Chen, M.; Huang, C.; He, C.; Zhu, W.; Xu, Y.; Lu, Y. Glucose-Responsive Controlled Release System Using Glucose Oxidase-Gated Mesoporous Silica Nanocontainers. *Chem. Commun*. **2012**, 48, 9522-9524.

(22) Wang, J. Electrochemical glucose biosensors. *Chem. Rev*. **2008**, 108, 814-825.

(23) Kalita, H.; Kumar, B. P.; Konar, S.; Tantubay, S.; Mahto, M. K.; Mandal, M.; Pathak, A., Sonochemically synthesized biocompatible zirconium phosphate nanoparticles for pH sensitive drug delivery application. *Materials Science and Engineering: C* **2016,** *60*, 84-91.

(24) Kan, Y.; Clearfield, A., Zirconium Phosphate Supported MOF Nanoplatelets. *Inorg. Chem.* **2016**, 55, 5634-5639.

(25) Silbernagel, R.; Martin, C. H.; Clearfield, A., Zirconium (IV) Phosphonate–Phosphates as Efficient Ion-Exchange Materials. *Inorg. Chem.* **2016,** *55* (4), 1651-1656.

(26) Alberti, G.; Casciola, M.; Capitani, D.; Donnadio, A.; Narducci, R.; Pica, M.; Sganappa, M., Novel Nafion–zirconium phosphate nanocomposite membranes with enhanced stability of proton conductivity at medium temperature and high relative humidity. *Electrochim. Acta* **2007,** *52* (28), 8125-8132.

(27) Liu, L.-M.; Wen , J.; Liu, L.; He, D.; Kuang, R.-y.; Shi, T., A mediator-free glucose biosensor based on glucose oxidase/chitosan/α-zirconium phosphate ternary biocomposite. *Anal. Biochem.* **2014,** *445*, 24-29.

(28) Deshapriya, I. K.; Kim, C. S.; Novak, M. J.; Kumar, C. V., Biofunctionalization of α-zirconium phosphate nanosheets: toward rational control of enzyme loading, affinities, activities and structure retention. *ACS applied materials & interfaces* **2014,** *6* (12), 9643-9653.

(29) Duff Jr, M. R.; Kumar, C. V. Molecular Signatures of Enzyme-Solid Interactions: Thermodynamics of Protein Binding to α-Zr(IV) Phosphate Nanoplates. *J. Phys. Chem. B* **2009**, 113, 15083-15089.

(30) Duff Jr, M. R.; Kumar, C. V. Protein-Solid Interactions: Important Role of Solvent, Ions, Temperature, and Buffer in Protein Binding to α-Zr(IV) Phosphate. *Langmuir* **2009**, 25, 12635-12643.

(31) Ding, Y.; Jones, D. J.; Maireles-Torres, P.; Roziere, J. Two-dimensional nanocomposites: alternating inorganic-organic polymer layers in zirconium phosphate. *Chem. Mater*. **1995**, 7, 562-571.

(32) Pattammattel, A.; Deshapriya, I. K.; Chowdhury, R.; Kumar, C. V. Metal-enzyme frameworks: Role of metal ions in promoting enzyme self-assembly on α-Zirconium(IV) phosphate nanoplates. *Langmuir* **2013**, 29, 2971-2981.

(33) Pattammattel, A.; Puglia, M.; Chakraborty, S.; Deshapriya, I. K.; Dutta, P. K.; Kumar, C. V., Tuning the activities and structures of enzymes bound to graphene oxide with a protein glue. *Langmuir* **2013,** *29* (50), 15643-15654.

(34) Clearfield, A.; Stynes, J. A. The preparation of crystalline zirconium phosphate and some observations on its ion exchange behaviour. *J. Inorg. Nucl. Chem.* **1964**, 26, 117-129.

(35) Keller, S. W.; Kim, H.-N.; Mallouk, T. E., Layer-by-Layer Assembly of intercalation compounds and heterostructures on surfaces: Toward molecular" beaker" epitaxy. *J. Am. Chem. Soc*. **1994,** *116* (19), 8817-8818.

(36) Deshapriya, I. K.; Kumar, C. V., Nanobio Interfaces: Charge control of enzyme/inorganic interfaces for advanced biocatalysis. *Langmuir* **2013,** *29* (46), 14001-14016.

(37) Hoare, D. G.; Koshland, D. E. A method for the quantitative modification and estimation of carboxylic acid groups in proteins. *J. Biol. Chem.* **1967**, 242, 2447-2453.

(38) Sparks, D. L.; Phillips, M., Quantitative measurement of lipoprotein surface charge by agarose gel electrophoresis. *J. Lipid Res.* **1992,** *33* (1), 123-130.

(39) Pazur, J. H.; Kleppe, K., The Oxidation of Glucose and Related Compounds by Glucose Oxidase from Aspergillus niger*. *Biochemistry* **1964,** *3* (4), 578-583.

(40) Hodak, J.; Etchenique, R.; Calvo, E. J.; Singhal, K.; Bartlett, P. N., Layer-by-layer self-assembly of glucose oxidase with a poly (allylamine) ferrocene redox mediator. *Langmuir* **1997,** *13* (10), 2708-2716.

(41) Jelesarov, I.; Bosshard, H. R., Isothermal titration calorimetry and differential scanning calorimetry as complementary tools to investigate the energetics of biomolecular recognition. *Journal of molecular recognition* **1999,** *12* (1), 3-18.

(42) Sturtevant, J. M., Biochemical applications of differential scanning calorimetry. *Annu. Rev. Phys. Chem.* **1987,** *38* (1), 463-488.

(43) Breslauer, K. J.; Freire, E.; Straume, M., [28] Calorimetry: A tool for DNA and ligand—DNA studies. *Methods Enzymol.* **1992,** *211*, 533-567.

(44) McGhee, J. D.; von Hippel, P. H., Theoretical aspects of DNA-protein interactions: co-operative and non-co-operative binding of large ligands to a one-dimensional homogeneous lattice. *J. Mol. Biol.* **1974,** *86* (2), 469-489.

(45) Scales, P. J.; Grieser, F.; Healy, T. W.; White, L. R.; Chan, D. Y. C. Electrokinetics of the silica-solution interface: a flat plate streaming potential study. *Langmuir* **1992**, 8, 965-974.

(46) Sierra, J. F.; Galban, J.; Castillo, J. R. Determination of glucose in blood based on the intrinsic fluorescence of glucose oxidase. *Anal. Chem.* **1997**, 69, 1471-1476.

(47) Gratzer, W.; Cowburn, D., Optical activity of biopolymers. *Nature* **1969**, 222, 426 – 431.

(48) Fasman, G. D., *Circular dichroism and the conformational analysis of biomolecules*. Springer Science & Business Media: 2013.

(49) Kumar, C. V.; McLendon, G. L., Nanoencapsulation of cytochrome c and horseradish peroxidase at the galleries of α-zirconium phosphate. *Chem. Mater.* **1997,** *9* (3), 863-870.

(50) MacLachlan, D. J.; Morgan, K. R., Phosphorus-31 solid-state NMR studies of the structure of amine-intercalated. alpha.-zirconium phosphate. 2. Titration of. alpha.-zirconium phosphate with n-propylamine and n-butylamine. *J. Phys. Chem.* **1992,** *96* (8), 3458-3464.

(51) Nishimura, M.; Hayashi, M.; Hayakawa, K.; Miyazaki, M., Ion Chromatographic Study of Sulfate-Complexes in Aqueous Solution. *Anal. Sci.* **1994,** *10*, 321.

(52) Mehrotra, S.; Lynam, D.; Maloney, R.; Pawelec, K. M.; Tuszynski, M. H.; Lee, I.; Chan, C.; Sakamoto, J., Time Controlled Protein Release from Layer-by-Layer Assembled Multilayer Functionalized Agarose Hydrogels. *Adv. Funct. Mater.* **2010,** *20* (2), 247-258.

(53) Baveghems, C. L.; Pattammattel, A.; Kumar, C. V., Designer Histone Complexes: Controlling Protein-DNA Interactions With Protein Charge as 'All-Or-None'Digital Switch. *J. Phys. Chem. B* **2016**. **DOI:** 10.1021/acs.jpcb.6b08651

(54) Lumry, R.; Rajender, S. Enthalpy-Entropy compensation phenomena in water solutions of proteins and small molecules: a ubiquitous properly of water. *Biopolymers* **1970**, 9, 1125-1227.

(55) Liu, L.; Yang, C.; Guo, Q.-X. A study on the enthalpy-entropy compensation in protein unfolding. *Biophys. Chem.* **2000**, 84, 239-251.

(56) Tzeng, S.-R.; Kalodimos, C. G. Dynamic activation of an allosteric regulatory protein. *Nature* **2009,** 462, 368-372.

(57) Marques, H. M.; Bradley, J. C.; Campbell, L. A., Ligand substitution reactions of aquacobalamin: evidence for a dissociative interchange mechanism. *J. Chem. Soc., Dalton Trans.* **1992,** (13), 2019-2027.

(58) Manning, G. S., Limiting laws and counterion condensation in polyelectrolyte solutions I. Colligative properties. *The J. chem. Phys.* **1969,** *51* (3), 924-933.

(59) Chowdhury, R.; Stromer, B.; Pokharel, B.; Kumar, C. V., Control of Enzyme-Solid Interactions via Chemical Modification. *Langmuir* **2012,** *28* (32), 11881-11889.

(60) van Kasteren, S. I.; Kramer, H. B.; Jensen, H. H.; Campbell, S. J.; Kirkpatrick, J.; Oldham, N. J.; Anthony, D. C.; Davis, B. G., Expanding the diversity of chemical protein modification allows post-translational mimicry. *Nature* **2007,** *446* (7139), 1105-1109.

(61) Spicer, C. D.; Davis, B. G., Selective chemical protein modification. *Nature communications* **2014,** *5*:4740, 1-14.

(62) Boutureira, O.; Bernardes, G. a. J., Advances in chemical protein modification. *Chem. Rev.* **2015,** *115* (5), 2174-2195.

(63) Krall, N.; da Cruz, F. P.; Boutureira, O.; Bernardes, G. J., Site-selective protein-modification chemistry for basic biology and drug development. *Nature chemistry* **2016,** *8* (2), 103-113.

(64) Gunnoo, S. B.; Madder, A., Chemical Protein Modification through Cysteine. *ChemBioChem* **2016,** *17* (7), 529-553.

(65) Chaudhari, A.; Thota, J.; Kumar, C., Binding and cleavage studies of two proteins intercalated at the galleries of α-zirconium phosphate. *Microporous Mesoporous Mater.* **2004,** *75* (3), 281-291.

(66) Duff Jr, M. R.; Kumar, C. V., Protein-Solid Interactions: Important Role of Solvent, Ions, Temperature, and Buffer in Protein Binding to α-Zr(IV) Phosphate. *Langmuir* **2009,** *25* (21), 12635-12643.

(67) Duff Jr, M. R.; Kumar, C. V., Molecular Signatures of Enzyme-Solid Interactions: Thermodynamics of Protein Binding to α-Zr(IV) Phosphate Nanoplates. *The Journal of Physical Chemistry B* **2009,** *113* (45), 15083-15089.

(68) Thilakarathne, V. K.; Briand, V. A.; Kasi, R. M.; Kumar, C. V., Tuning Hemoglobin-Poly (acrylic acid) Interactions by Controlled Chemical Modification with Triethylenetetramine. *The Journal of Physical Chemistry B* **2012,** *116* (42), 12783-12792.

(69) Fabre, R. M.; Talham, D. R., Stable supported lipid bilayers on zirconium phosphonate surfaces. *Langmuir* **2009,** *25* (21), 12644-12652.

(70) Mazur, M.; Krysiński, P.; Michota-Kamińska, A.; Bukowska, J.; Rogalski, J.; Blanchard, G., Immobilization of laccase on gold, silver and indium tin oxide by zirconium–phosphonate–carboxylate (ZPC) coordination chemistry. *Bioelectrochemistry* **2007,** *71* (1), 15-22.

(71) Yaguchi, M.; Uchida, T.; Motobayashi, K.; Osawa, M., Speciation of Adsorbed Phosphate at Gold Electrodes: A Combined Surface-Enhanced Infrared Absorption Spectroscopy and DFT Study. **2016**, *7*, 3097-3102.

(72) Haghighi, N.; Hallaj, R.; Salimi, A., Immobilization of glucose oxidase onto a novel platform based on modified TiO2 and graphene oxide, direct electrochemistry, catalytic and photocatalytic activity. *Materials Science and Engineering: C.* **2017**, *73*, 417-424.

Chapter 3: Biodegradable Light Harvesting Antennas for Solar Cell Applications

3.1. Abstract

Artificial antenna complexes built via self-assembly are reported here, which indicated excellent energy transfer efficiency, macroscopic organization, unprecedented high thermal stability and ease of formation. Our system consists of four fluorescent donor-acceptor dyes, double-helical DNA and cationized bovine serum albumin, all self-assembled on cover glass slips to form functional materials. These captured radiation in the range of 330-590 nm, and excitation of any of the donor dyes resulted in efficient emission from the terminal acceptor. Excitation spectra provided unequivocal proof of energy transfer via jumper dyes, and transfer was interrupted when one of the jumper dyes is omitted, another direct evidence for cascade energy transfer. In the case of five dye systems, the radiation range was extended (330-620 nm). The entire assembly indicated unusually high thermal stability and continued to function efficiently even after exposure to 80 ˚C for >169 days, an important consideration for field applications. Furthermore, the BSA/DNA matrix was substituted by sucrose or glucose systems, both of which demonstrated light harvesting. However, phosphoric acid swollen cellulose (PASC) or carboxymethylcellulose (CMC) did not harvest light when used as matrices. These unusually stable, high efficiency, multi-chromophoric, artificial antennas are the first of their kind to demonstrate self-assembled 4-dye energy cascade, converting blue photons to red photons.

3.2. Introduction

Solar energy is being touted as a long term, sustainable, green energy source.[1,2] Natural photosynthetic systems use a set of pigments which are non-covalently bound to well-organized,

self-assembled protein complexes and harvest light over a broad wavelength window.[3] Building efficient artificial analogues of such systems continues to be a fundamental challenge, particularly when examined through the lens of solar cell applications.[4] For example, the majority are solution-based systems requiring complex synthesis and extensive purification. Additionally, efficiency of energy transfer is often low. Finally, their stability over extended periods of time and their functionality in solid state has not been demonstrated which are probably just as important for practical solar applications. Most solar cells have poor efficiency in the UV region and these high-energy photons are also responsible for the eventual degradation of its components, ultimately leading to the failure of the cell. Conversion of these UV photons to the corresponding longer wavelength photons, or downshifting, is one strategy that is expected to improve overall cell performance and longevity. Therefore, a light-harvesting device that converts UV or blue photons to red photons and operates in the solid phase will be attractive.[5] Another important consideration is the environmental burden of the current solar cell components, and there is great need to reduce this burden for large-scale production of solar energy worldwide.

Inspired by nature, we designed artificial antenna complexes consisting of multiple donor-acceptor fluorescent dyes that self-assemble while using readily bio-degradable components (**Scheme 1**). Our hypothesis is that individually-wrapped, densely packed donor-acceptor dyes could favor efficient Förster resonance energy transfer (FRET) but such dense packing must also avoid direct dye-dye contacts to suppress energy-wasting bimolecular quenching processes.[6] These opposing requirements can be met by embedding the dyes in the protein-DNA matrix. Additionally, to demonstrate the versatility of this approach, we tested

other biological matrices as a comparison to protein-DNA and these showed comparable light harvesting.

Another important consideration is finding alternatives to covalent chemistry that is often used for the construction of the antenna complexes. While there are many elegant examples of covalent coupling of dyes to form antenna complexes,[7] such approaches can be challenging and very expensive. Therefore, we sought out a self-assembly approach which is rugged and simple, but effective in achieving dense packing of multiple chromophores. To the best of our knowledge, efficient and highly stable energy cascade antenna films that are self-assembled from biological components have not been reported to date. Our design is rational, modular, robust, and functional in the solid state, while its synthesis can be readily scaled-up using abundant, renewable, non-toxic, environmentally benign, and inexpensive components.

The chemical novelty of the current system is that highly organized protein-DNA matrix provides discrete, single-occupancy binding sites for jumper dyes such that the dyes are packed densely to promote FRET while inhibiting the excimer/exciplex formation (**Scheme 1**). This strategy is in contrast to dyes packed in polymer films, covalently attached to DNA strands, or embedded in other media where the dye-dye interactions can quench excitation propagation and compete with energy transfer.[8] This is important because the antennas that are obtained via covalently conjugation methods might not function well in the solid phase due to inappropriate positioning of the donor acceptor dyes in the solid matrix where energy wasting excimer/exciplex formation can occur upon film formation. Dense population of the binding sites in the current system also assures that there would be one or more acceptors for a given donor

Scheme 3.1. Artificial antenna complexes constructed from donors, acceptors, cationized BSA (cBSA), and DNA.

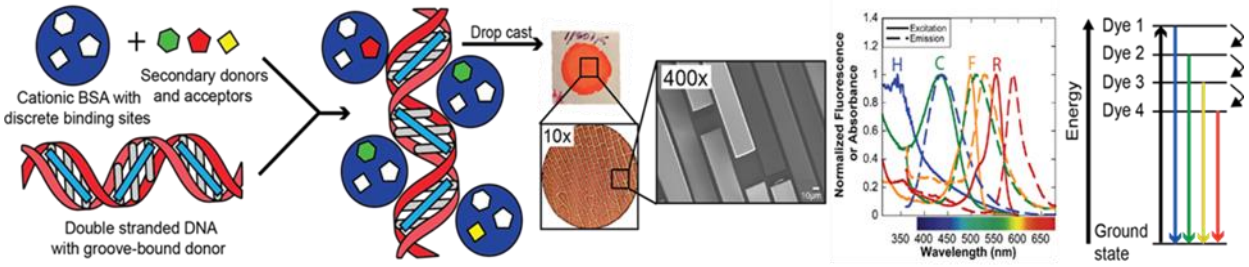

within the Förster volume for efficient FRET while avoiding undesirable energy wasting processes.

3.3. Materials and Methods

Bovine serum albumin (BSA) was purchased from Equitech-Bio, Inc (Texas) and salmon sperm DNA sodium salt was purchased from Amresco (Ohio). Hoechst 33258 (H) and Fluorescein (F) were purchased from Sigma (Milwaukee, Wisconsin). Coumarin 540A (C) was purchased from Exciton Chemical Co. Inc., (Ohio) and Rhodamine B (R) was purchased from Eastman Kodak Company (Rochester, NY). 1-Ethyl-3-(3-dimethylaminopropyl)carbodiimide (EDC) was purchased from TCI America (Portland, OR).Glass cover slips of 22 mm x 22 mm were purchased from Fisher Scientific (Atlanta, GA).

3.3.1. ***Chemical modification of BSA:*** BSA (1 g) was dissolved in 4 mL deionized water (DI) and stirred with 5 mL of 0.5 M triethylenetetramine (TETA) dissolved in DI and the pH adjusted to 5.0 using concentrated hydrochloric acid. After stirring for 30 min, 1 mL of 250 mM 1-ethyl-3-(3-dimethylaminopropyl)carbodiimide (EDC) dissolved in DI was added to give final concentration of 25 mM EDC. The reaction mixture was stirred for additional 4 h at room temperature and unreacted EDC, TETA, and byproducts were removed by dialysis in 25k MWCO membrane from Spectrum Laboratories, Inc. (Rancho Dominguez, CA) against 10 mM phosphate buffer, pH 7.2. The cationized BSA (cBSA) sample was then concentrated via centrifugation using Amicon tubes (25,000 MW cut off) from Millipore Inc. (Bedford, MA) until final concentration reached 1.5 mM- 2 mM. The chemical modification of BSA was confirmed by agarose gel electrophoresis.

3.3.2. ***Fabrication of thin films using drop-casting method:*** Rhodamine B (R) in DI (2.5 mM), Fluorescein (F) (10 mM) in DI and Coumarin 540A (C) (25 mM) in dimethylforaamide (DMF)

were added in that order to 2 mM cBSA and 10 mM phosphate buffer pH 7 and mixed well in a microcentrifuge tube. In the case of the five dyes systems 5 mM of 5-Carboxy-X-Rhodamine (ROX) was used. DNA/Hoechst 33258 solution was prepared by adding Hoechst 33258 (H) (5 mM) in DI to 5 mM DNA (by base pairs) solution 10 mM phosphate buffer pH 7 in a second microcentrifuge tube. cBSA/C/F/R solution and DNA/H solutions were combined together and mixed well. No precipitates formed during these manipulations. Final concentrations of each component in the solution were 300 μM cBSA, 800μM DNA, 50 μM H, 250 μM C, 100 μM F, and 40 μM R. The above complex (500 μl) was drop-cast on the surface of 22 mm x 22 mm glass coverslip and allowed to air-dry overnight.

3.3.3. ***Absorption and steady state fluorescence measurements:*** Absorption spectra of films on glass cover slips were collected using HP 8453 diode array spectrophotometer from Agilent Technologies (Mendon, MA). Steady state fluorescence spectra were collected using home-built fluorescence spectrophotometer using SLM-Aminco optics at 67.5° incidence angle. The instrument is routinely wavelength calibrated prior to each experiment. Front phase accessory, and slit widths set to 4 mm were used to collect emission and excitation spectra of the films whose thickness was less than 100 μm. During absorbance and steady state fluorescence experiments, glass cover slips were oriented in such a way that the same area is exposed for both absorbance and fluorescence measurements. Samples were moved around and rotated to check for uniformity, and several vertical orientations at fixed incidence angle were used to obtain averaged values.

3.3.4. ***Perrin plots and estimation of the Förster radii:*** The total volume of the film was calculated using total mass of each of the components and their densities. Dye concentrations

ranged from 2.5 mM – 7.7 mM for different dyes, and cBSA concentration was 18.5 mM. These values were used to calculate quenching radii, using Perrin equation:

$$\ln \Phi_0/\Phi = VN[Q]$$

where Φ_0 and Φ are the quantum yields for donor emission in the absence and presence of acceptor, V is the volume of the quenching sphere; N is the Avogadro's number and [Q] is the concentration of the acceptor.

For example, the Forster radius of Fluorescein (F) and Rhodamine B (R) was determined by systematically varying R film phase concentration from 0 to ~10 mM and recording the emission spectra. Perrin plot was constructed by plotting $\ln \Phi_0/\Phi$ vs [R]. From the slopes of the plots, quenching volumes were extracted and quenching radii determined. Similarly, other quenching radii were obtained.

3.3.5. ***High temperature stability:*** Protein/DNA/dye films were incubated at 80-85 ˚C and the fluorescence spectra collected at intervals for a total of 169 days. Films were allowed to cool for 2-3 hours at room temperature before spectra were recorded. Three separate samples were used to estimate errors for each data point. Measurements of emission and excitation were recorded at three separate orientations by rotating samples. Measurements were highly reproducible and the error bars were determined. A solution of R (4 μM) in phosphate buffer (350 nm excitation and 590 nm monitoring) was used as the standard for normalizing the day-to-day data.

3.4. Results

3.4.1. ***Preparation of antenna films:*** A set of four dyes was chosen here, such that the emission spectrum of one donor dye had a significant overlap with the absorption spectrum of its corresponding acceptor, so that each of the pairs could undergo FRET. We chose Hoechst 33258 (H) as the highest energy donor, Coumarin 540A (C), which served as an acceptor for

H,Fluorescein (F), which served as an acceptor for C, and Rhodamine B (R), which served as an acceptor for F (**Scheme 1**). The emission spectra of donors have significant overlaps with the absorption spectra of the corresponding acceptors (**Scheme 1**), and these pairs are known to undergo efficient FRET.[9,10] DNA and bovine serum albumin (BSA) are excellent hosts for a number of dyes.[11] H binds to DNA (K_b=1x10^6 M^{-1}) but not to BSA.[12] C, F and R bind to BSA. Cationization of BSA promoted its binding to anionic DNA. Upon mixing, these six distinct components spontaneously form functional, ordered, self-assembled solid state films. Aqueous buffered solutions of cBSA, R, F, C, salmon sperm DNA, and H were mixed together and drop casted onto glass substrates and air-dried. Even though the dyes had only moderate affinity to their corresponding binding sites in the solution phase, dye binding in the solid state improved substantially because of the increased concentrations of both the dyes (2.5–8 mM dye) as well as their host materials (18-50 mM) in the films when compared to their corresponding solution concentrations which were in the micromolar range. Optical and electron microscopy of the DNA/BSA/dye films indicated nearly perfect grid patterns (**Scheme 1**), where the assemblies were highly ordered on millimeter to micrometer length scales. Neither DNA nor cBSA alone formed such ordered assemblies.

3.4.2. ***Confirmation of FRET:*** The absorption spectra of the dyes bound to the protein-DNA assemblies in the solution phase (**Figure 1A**) and the emission spectra of the individual dyes embedded in the protein-DNA films (350 nm excitation, **Figure** 1B) did not indicate dye

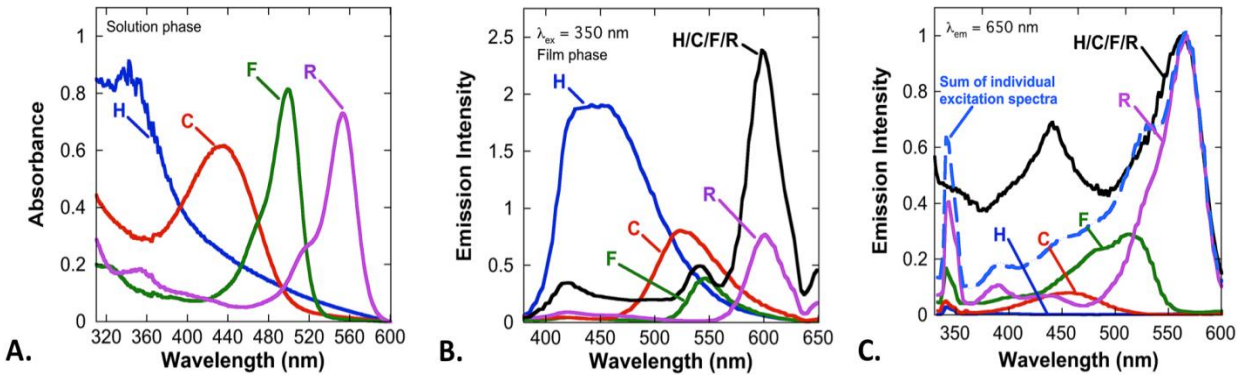

Figure 3.1. (A) Absorbance spectra of Hoechst 33258 (H), Coumarin 540A (C), Fluorescein (F), and Rhodamine B (R) in solution with cBSA and DNA ([cBSA] = 300 μM, [DNA] = 800 μM base pairs, [H] = 50 μM, [C] = 125 μM, [F] = 100 μM, [R] = 40 μM). (B) Emission spectra (350 nm excitation) of individual dyes and 4-dye protein/DNA assembly (black line) in the film state (film concentrations, when present, [H] = 3.1 mM, [C] = 7.7 mM, [F] = 6.2 mM, [R] = 2.5 mM, [cBSA] = 18.5 mM, [DNA] = 49.2 mM base pairs). (C) Excitation spectra (650 nm monitoring) of individual dyes and the 4-dye protein/DNA assembly (black line) in film phase.

aggregation. Excitation energy cascade from H to R was examined by recording emission spectra of the assemblies by exciting at 350 nm, where H absorbs predominantly (**Fig. 1A**). Intense emission from R was noted at 590 nm (**Fig. 1B,** black line), and there was a ~2.4-fold increase in R emission from the composite film when compared to direct excitation of R/DNA/cBSA film (**Fig. 1B**, purple line). Enhanced emission from R in the antenna complex was due to light absorption by H at 350 nm, followed by energy transfer via the jumper dyes to R. Energy cascade from H to R via the jumper dyes was tested by recording the emission spectra (excitation at 350 nm) of a series of samples where one particular jumper dye was omitted at a given time (**Figure 2**). When R was omitted, for example, intense emission was noted from F. Omission of F led to increased emission of C, as transfer to R was interrupted by the absence of the jumper dye F. When C was omitted, emission from H increased because there was little or no excitation transfer to F or R without the jumper dye C. In every one of these cases, energy transfer from H to R was interrupted when a particular jumper dye was missing. Additionally, emission from the intermediate acceptor appeared when the sequence was broken, which was consistent with energy cascade transfer from H to C to F to R.

The energy cascade was confirmed in another set of experiments where a series of excitation spectra (**Figure 1C**) were recorded by monitoring R emission at 650 nm. If cascade transfer was operational, then the excitation spectrum of the 4 dye/protein/DNA film when monitored at R emission wavelengths should show excitation peaks corresponding to each dye that directly or indirectly transfers energy to R. The excitation spectrum of the composite film (**Figure 1C**, black line) indicated energy transfer from each of these dyes. For comparison, the excitation spectrum of each individual dye bound to the protein/DNA complex is shown (Fig. 1C**,** as marked), as well as the sum of the individual dye spectra (**Figure 1C**, blue dashed line).

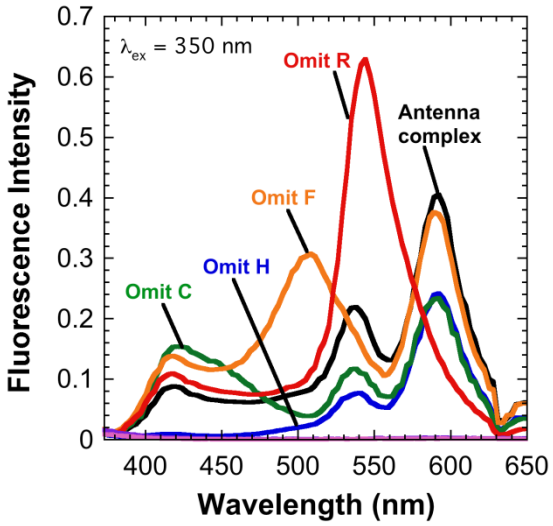

Figure 3.2. Fluorescence spectra of antennae complex (black) with all four dyes/DNA/protein, and those of the films with one of the four dyes omitted each time. Omitted dye: H (blue) C (green), F (yellow) and R (red).

Regions where the summed spectrum is well below the observed excitation spectrum of the 4 dye-antenna (360-500 nm) indicate efficient energy transfer to R.

3.4.3. ***FRET efficiency studies:*** The energy transfer efficiency of the antenna was optimized by adjusting individual dye concentrations. The concentration of a given dye was varied while fixing the concentrations of cBSA, DNA, and all other dyes. Each of these films was excited at 350 nm, and the emission from R at 650 nm was monitored. The intensity of emission at 650 nm was plotted as a function of a specific dye concentration (**Figure 3A**), while all other concentrations were kept constant. The overall energy transfer efficiency depended on the highest energy donor concentration which clearly indicated donor-donor and donor-acceptor FRET. In solution, bimolecular energy transfer depends only on the acceptor concentration since the concentration of donor excited states is too small under the excitation conditions in the fluorimeter. Donor-concentration dependence on FRET was attributed to donor-to-donor energy transfer.[13]

Calculating the efficiency (E) of energy transfer can be difficult, particularly in systems with more than one donor-acceptor pair. As such, many methods of calculation have been reported, which makes comparison of the performance of our system with the others quite difficult. Examples of such systems from the literature include tobacco mosaic virus coat protein,[14] DNA bundles,[15] DNA-lipid complexes,[16] DNA/protein complexes,[17] DNA origami structures,[18] and DNA photonic wires.[19,20] In the case of tobacco mosaic virus coat protein-3 dye system was given the efficiency as the ratio of donor absorbance to donor excitation of ~0.90.[14] In the case of DNA-based antenna system, the efficiency was estimated as that of donor quenching (E= ~0.90).[15] The

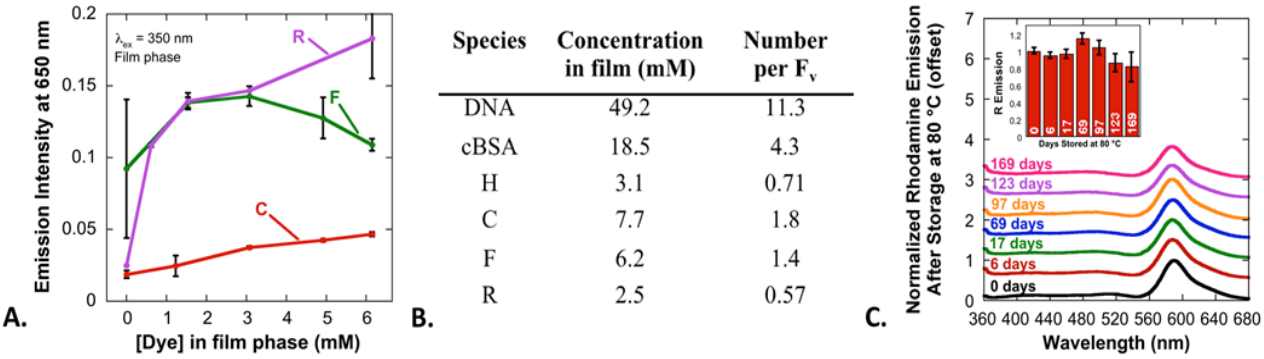

Species	Concentration in film (mM)	Number per F_v
DNA	49.2	11.3
cBSA	18.5	4.3
H	3.1	0.71
C	7.7	1.8
F	6.2	1.4
R	2.5	0.57

Figure 3.3. (A) Plots of R emission intensity at 650 nm (350 nm excitation) as a function of C (red line), F (green line) or R (purple line) concentration while the other concentrations have been fixed (when present) at 49.2 mM DNA, 18.5 mM cBSA, 3.1 mM H, 7.7 mM C, 6.2 mM F and 2.5 mM R. (B) Table of dye concentrations in the film and the corresponding occupancy numbers per average Förster volume (F_v, 6.6×10^5 Å^3). (C) Extraordinary thermal stability of artificial antenna complex. Emission spectra (λ_{ex} = 350 nm) were monitored as a function of time stored at 80 °C. (Inset) Intensity of R emission at 590 nm as a function of time stored at 80 °C.

quenching efficiency of the DNA photonic wire containing four dyes and a luminescent terbium complex was reported to be 0.22±0.06.[20] The efficiency of DNA-porphyrin system, in another study, was reported to be 0.55 from Förster theory.[16] The efficiency of the DNA origami-4 dye system was reported as the ratio of photons-in to photons-out (E=0.36±0.17).[18] Finally, the efficiency of the DNA based photonic wire with 4 dyes loaded on quantum dots was reported to have an overall efficiency of 0.01-0.08.[19]

The performance of our antenna system was evaluated by calculating the overall efficiency (E) using the following expression:

$$E = \frac{I_{F,AD} - I_{F,A}}{I_{F,A}}\left(\frac{1 - 10^{-A_A}}{1 - 10^{-A_D}}\right)$$

where $I_{F,AD}$ and $I_{F,A}$ were the emission intensities of the acceptor (R) at 590 nm when excited at 350 nm in the presence of the donor (H) and in the absence of the donor, respectively.; A_A was the absorbance at 350 nm of the acceptor (R), and A_D was the absorbance at 350 nm of all the donors. Two boundary conditions were satisfied by the above equation. First, if there was no energy transfer from the donor excited states to A, the value of E must be 0. Second, if the efficiency is 100%, then E must be 1, and both equations are simultaneously satisfied by the equation. Because the final films were not optically dilute, the absorbance values of the samples were obtained in the solution phase, assuming that the molar absorptivity did not change when the dye transitioned from solution phase to film phase. The efficiency calculated above is for the overall cascade transfer from donor excited states to R via the intervening jumper dyes, and hence it is a product of the efficiencies of all the intervening steps from excitation to emission. The

overall efficiency obtained from the above analysis of our system was 0.23, and similar analysis on the other system reported could not be done due to lack of published data. To the best of our knowledge, our value is comparable to or better than 0.01-0.36 reported for other 4 dye systems.[18-20] Such efficiencies are expected for multi-step FRET processes where each step is less than 100% efficiency, because the overall efficiency is related to the product of the efficiencies of the individual steps. In the DNA photonic wire system containing a luminescent terbium complex and four dyes reported by Massey et al., for example, individual FRET events between constituent chromophores were up to ~80% efficient, but the step-wise nature of the overall process resulted in an efficiency of 0.22±0.06.[20] Individual steps could be less than 100% efficient when the excitation of the system is quenched by non-radiative pathways or by emission from an intermediary jumped dye. Emission from intermediary dyes was observed in our DNA/cBSA/four dye system, as demonstrated by the peaks at ~420 nm and ~540 nm (Fig. 1B, black line), which correspond to H and F, respectively. Additionally, broad emission was observed between 420 nm and 540 nm. When compared to the emission spectra films containing DNA, cBSA, and individual dyes, this provided insight into the overall efficiency of the system.

3.4.4. ***Calculation of Photon Transfer Factor:*** We also examined another important parameter which is useful for applications in the solar cells. Silicon solar cells, for example, are more efficient in the red regions of the solar spectrum than the blue region, and one hypothesis is that the conversion of the blue photons to the red could improve cell performance. Therefore, we calculated the conversion of the high energy blue photons (350 nm) to red (590 nm) photons by comparing the emission of the antenna with all the 4 dyes at 590 nm (**Figure 1B**, black line, 350

nm excitation) with that of the film consisting of only R (2.5 mM) (**Figure 1B**, purple line, 350 nm excitation). The emission intensity at 590 nm by the antenna was greater by a factor (photon transfer factor) of ~2.4 due to the energy transfer from the 3-additional dyes present in the film. Thus, the blue-to-red conversion efficiency is also an important characteristic of the current antenna which might be useful for solar cell applications. Similar parameters for other systems are not available for comparison but we speculate that this kind of blue-to-red conversion will be of high practical importance.

3.4.5. ***Role of Matrix Components***: The roles of DNA and cBSA in the energy cascade mechanism were examined in a number of control experiments. When cBSA was omitted, there was no energy transfer from H to R (**Figure 4A**). Similarly, films made from the four dyes without any DNA and cBSA did not produce any emission. Because the dyes were known to form excitation quenching aggregates, the lack of emission from films containing DNA/four dyes and four dyes alone provided good evidence that the cBSA matrix helped to prevent aggregation of the dyes. The charge-conducting properties of DNA could be useful for device fabrication in future studies, where DNA could replace conducting polymers, and hence, we had to test if the antenna would function in the absence of DNA. To our surprise, FRET was noted in cBSA + 4 dye films in the absence of DNA (**Figure 4B**), which demonstrated the importance of the protein scaffold in segregating the dyes and positioning them correctly for FRET and the presence of DNA did not inhibit FRET in any manner. Additionally, the presence of DNA increased the variety of binding sites available for the self-assembly of a further variety of chromophores, if necessary.

Inspired by the effective highly efficient light harvesting observed from the biodegradable BSA/DNA matrix, we decided to substitute BSA/DNA with other biodegradable

matrices. Energy transfer was observed using a sucrose/4 dyes or glucose/4 dyes antenna (**Figure 5A** red curve and blue curve respectively). However, no energy transfer was observed when phosphoric acid swollen cellulose (PASC) (green curve) or carboxymethyl cellulose (CMT) (black curve) was used as a matrix suggesting that minimum binding affinities within specific Forster radii are required to facilitate the FRET needed for cascade energy transfer that drives efficient light harvesting. The corresponding excitation spectra (**Figure 5B**) corresponding to the emission spectra shown in **Figure 5A** confirmed energy transfer.

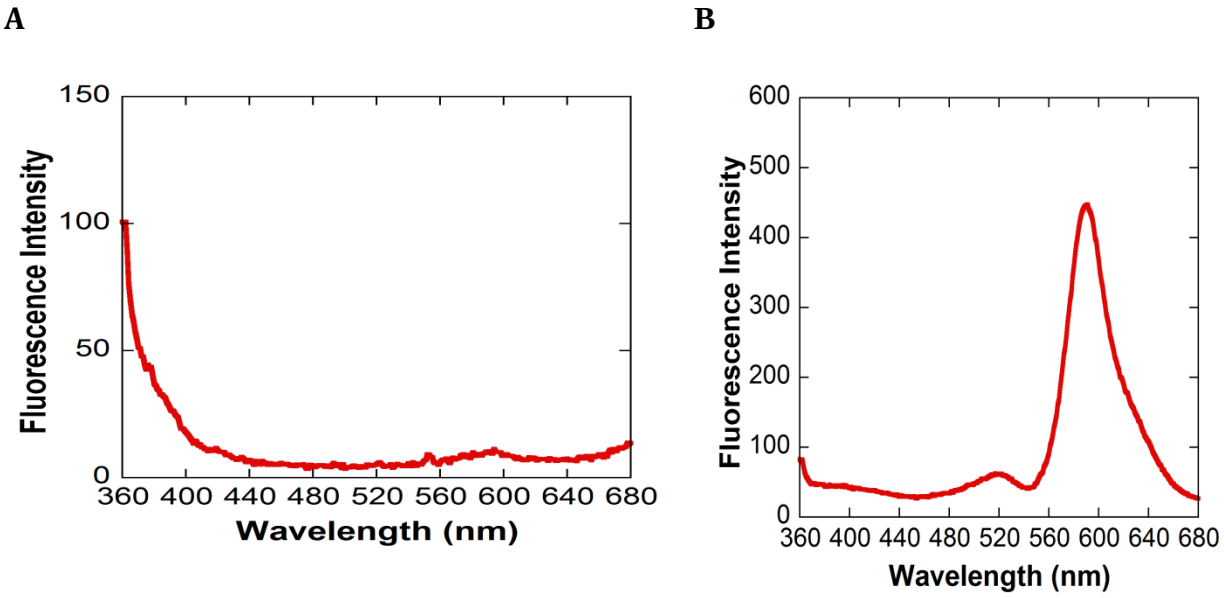

Figure 3.4. The importance of DNA and CBSA. (A) Emission spectrum of DNA + H + C + F + R without cBSA. The sample was excited at 350 nm and emission monitored from 460 to 680 nm. No energy transfer is observed in these films without cBSA. (B) Emission spectrum of 4-dyes embedded in cBSA film.

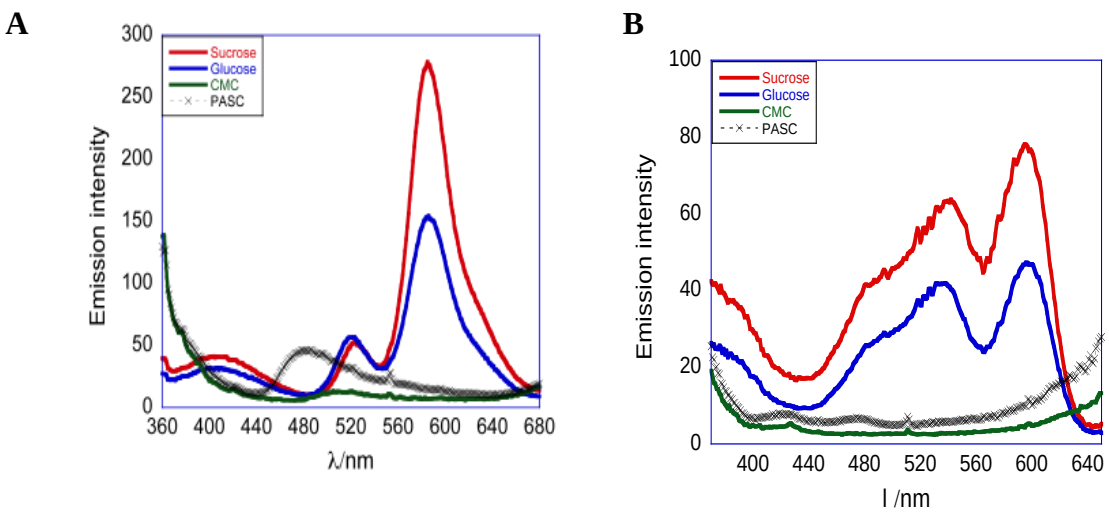

Figure 3.5. Comparison of biodegradable matrices tested in this study. (A) Emission spectra of Sucrose/4 dyes (red curve) showed light harvesting with a higher number of photons transferred when compared to glucose/4 dyes (blue curve). However, CMC/4 dyes (green curve) or PASC/4 dyes (black curve) did not transfer photons. (B) Excitation spectra corresponding to emission spectra in A.

3.4.6. ***Determination of Förster radii:*** To further characterize the energy transfer, the Foster radii for the donor-acceptor pairs embedded in the protein/DNA films were obtained from the Perrin equation ($\Phi=\Phi_0 e^{-VN[Q]}$), where Φ_0 and Φ are the quantum yields for donor emission in the absence and presence of acceptor, respectively, N is the Avogadro number, V is the Förster volume, and [Q] is the acceptor concentration. According to this model, the donor emission is quenched only when an acceptor is present within the Förster volume. Emission spectra were collected as a function of acceptor concentration (350 nm excitation) at fixed donor concentration in the protein/DNA films. The slope of the plot of $\ln(\Phi_0/\Phi)$ vs. [R] gave us an estimate of the Förster radius. Thus, the Förster radii for F-R, F-C and C-H pairs were found to be 58(±1), 45(±2), and 60(±2) Å, respectively. Taken together, the data clearly demonstrated energy cascade in the self-assembly.

The above observations can be readily explained in terms of the number densities of acceptors present within the Förster volume. For maximum efficiency, each Förster volume element containing a donor molecule should also have at least one acceptor. As a first approximation, the total volume of the solid film was calculated to be equal to the sum of the volumes of all the dry components; dyes, DNA, cBSA, and buffer. The occupancy number of each kind of dye molecule within the average Förster volume was calculated to be 0.71 for H, 1.8 for C, 1.4 for F, and 0.57 for R, corresponding to 1.55

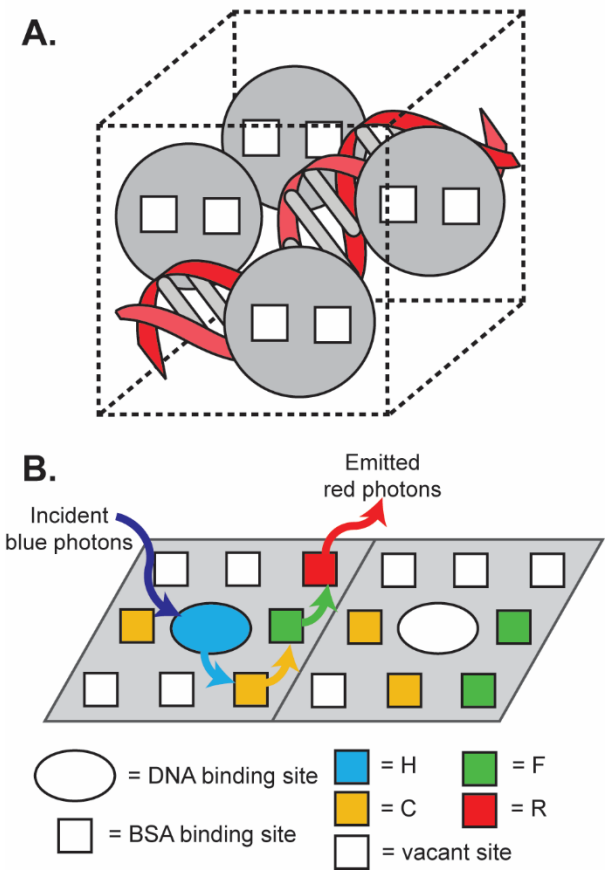

Scheme 3.2. A. Theoretical packing of DNA and BSA in one average Förster volume ($6.6x10^5$ $Å^3$), demonstrating dye binding sites (1 per DNA minor groove and 2 per BSA). B. 2D representation of the DNA/BSA film, where each square represents one average Förster volume. Any single cell contains 0.71 Hoechst 33258 (H), 1.8 Coumarin 540A (C), 1.4 fluorescein (F), 0.57 Rhodamine B (R), 11.3 base pairs of DNA, and 4.3 BSA. Conversion of incident blue photons to red photons via cascade energy transfer (indicated by curved arrows) only occurs in cells which contain at least one of each of the four dyes (right cell).

mM H, 3.85 mM C, 3.1 mM F, 1.25 mM R, 49.2 mM DNA and 18.5 mM cBSA (**Figure 2B**). Thus, the dye occupancies within the quenching cells were in the range of 0.57 to 1.8, with an average occupancy >1, which supported the above observations of efficient FRET in the supramolecular films. There was good probability that at least each of the quenching cells would have at least one donor or one acceptor dye (**Scheme 2**) and that the occupancy of the primary donor H, is higher than the acceptor molecules, except R. While this does not ensure simultaneous residency of both a donor and an acceptor within the same quenching cell, it enhances the chances for such an arrangement.

3.4.7. ***Thermal stability:*** Since the practical utility of any solar device would require high thermal stability over a long time, we examined the stabilities of these protein/DNA/dye films and monitored their emission after heating to elevated temperatures. Using 80-85˚C as a benchmark for the thermal stability of a solar device in the field, we examined FRET as a function of heating at this temperature in ambient air. After specific time intervals, samples were cooled to room temperature for 3 h, emission/excitation spectra were collected (**Figure 2C**), and the samples were returned to the oven. The emission intensities and excitation spectra showed little to no change over 0-169 days, and only small decreases were noted after 169 days. This extraordinary thermal stability coupled with high efficiency of FRET is novel.

3.4.8. ***Antenna Photostability:*** Efficient energy transfer from light harvesting is important for solar cell applications since red light is an efficient catalyst of solar powered cells. The ability to harvest most of the white light as demonstrated here is a key step towards highly efficient and increased output of solar cells. In this work, we have shown light harvesting due to excitation at 350 nm that is emitted at 590 nm due to the cascade effect among dyes positioned within the appropriate Forster radii. However, a major concern in the solar cell industry is the long-term

photostability against exposure to sunlight. We tested the photostability of our antenna complex by exposure to white light in a photo reactor in the absence of oxygen to minimize dye degradation due to reactive oxygen species (ROS). The glass films containing dropcasted samples were mounted inside a photo reactor tube (**Figure 6A**) and the entire assembly (reactor tube plus sample) was exposed to white light in a photo reactor (**Figure 6B**). Inside the photo tube, dry ice emission of CO_2 was used to purge oxygen from the system. Excess oxygen was collected in a balloon attached to the top of the photo tube.

Four antenna systems were irradiated over a two-day period and the emission maximum of each of the four dyes were recorded at various time points (**Figure 7**). The emission maximum at a given time as a ratio of initial emission intensity (I/I_0) was plotted against irradiation time. BSA-TETA/DNA/4 dyes (**Figure 7A**), BSA/4 dyes (**Figure 7B**), and BSA-TETA/4 dyes (**Figure 7C**) antennas were irradiated. Rapid degradation of a control sample (BSA-TETA/DNA/Rh, **Figure 7D**) indicated Rh as the most vulnerable chromophore in the four dyes cascade system. While Hoechst (440 nm) and coumarin (480 nm) emission increased slightly and stabilized, showing no degradation due to white light exposure over a period of more than 48 h, fluorescein (520 nm) emission remained the same or decreased slightly in the case of the BSA/4 dyes systems. However, rhodamine B (590 nm) emission degraded continuously over the 48 h irradiation period, reaching its half-life before the end of the period. This suggests that of the four dyes, rhodamine B was the most vulnerable to irradiation due to its position in the cascade as the terminal acceptor. The buildup of photons at the terminal acceptor probably drives comparatively rapid degradation. In fact, antenna photostability may improve if a non-emitting acceptor like TiO_2 is conveniently positioned to accept photons from the terminal acceptor.

A **B**

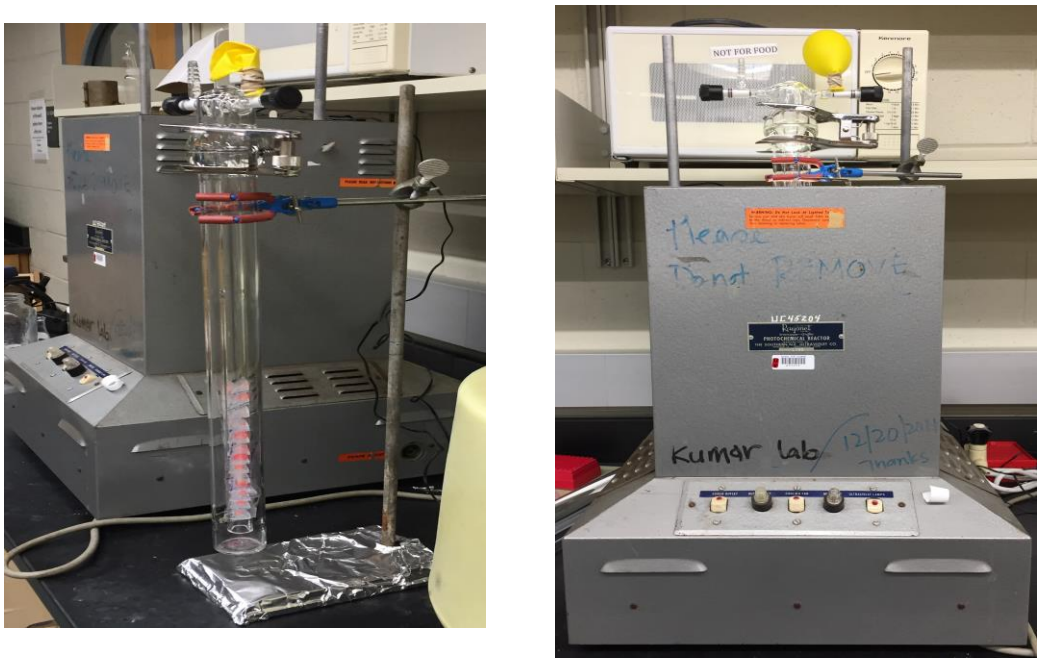

Figure 3.6. White light irradiation setup. (A) Samples dropcasted on a glass slide are mounted inside a photoreactor tube. (B) Photoreactor tube with samples is placed inside the photoreactor for exposure to white light. A balloon is used to collect excess CO_2 gas emitted from dry ice inside the photo tube.

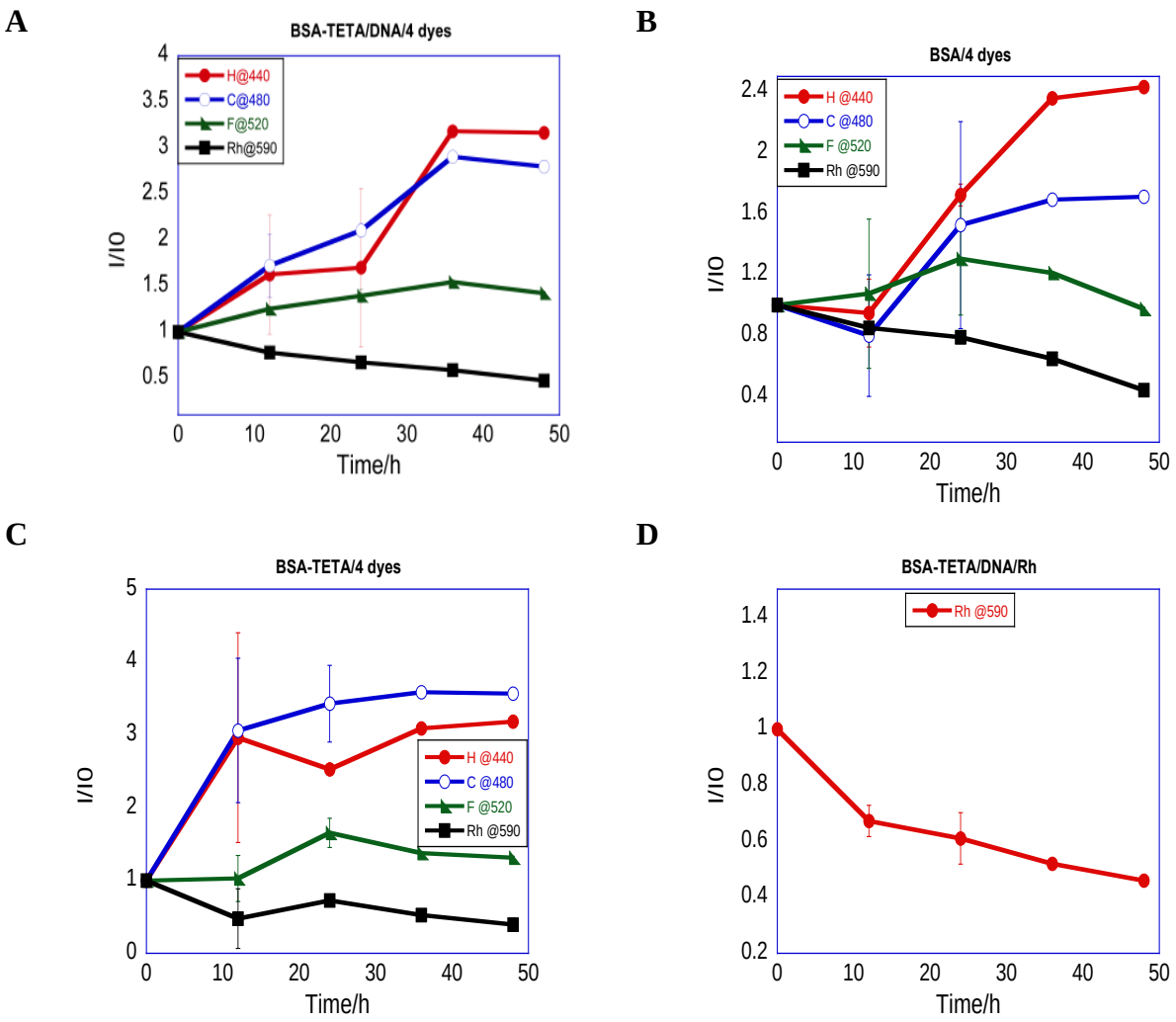

Figure 3.7. Photostability of antenna systems. Emission intensity after (I) as a ratio of before (I0) exposure to white light monitored over 48 h. (A) BSA-TETA/DNA/4 dyes, (B) BSA/4 dyes, (C) BSA-TETA/4 dyes, and (D) BSA-TETA/DNA/Rh upon exposure to white light. Rhodamine B, the terminal acceptor was identified as the most vulnerable to white light exposure.

3.5. Discussion

A biodegradable antenna system consisting of BSA, DNA, and four dyes is reported here. Each dye's binding constant and concentration is optimized such that maximum photon transfer in a cascade manner is achieved. While coumarin, fluorescein, and rhodamine associate with BSA binding pockets, Hoechst binds DNA. Together, the BSA/DNA matrix provides a scaffold that facilitates cascade energy transfer when the dyes are assembled within a specific Forster radius. Furthermore, the variety of binding pockets on BSA and DNA potentially increases the variety and combination of dyes that can be used as part of the cascade system.

The antennas are prepared in solution before dropcasting on a glass slide for overnight drying. Energy transfer was not observed in solution, suggesting that high concentrations of the chromophores and matrix afforded by evaporation of the solvent are required for the appropriate matrix scaffolding and optimal Forster radius among the dyes. In fact, experiments where the matrix and dye concentrations are varied demonstrate that energy transfer is reduced as matrix or dye concentration decreases.

A cascade light harvesting system was synthesized in this work via self-assembly on a biodegradable matrix. Hoechst was used as the primary donor dye such that excitation of the cascade occurred at 350 nm. Photons were then shuttled from dye to dye whereas the donor dye emission excited the acceptor dye throughout a four dye system with the terminal acceptor, rhodamine B that emitted at 590 nm. A 2.4 fold photon gain was calculated by measuring the difference between normalized emission intensity of the 4 dye antenna and the terminal acceptor, rhodamine B alone imbedded in the BSA/DNA matrix. This is an improvement on the number of photons transferred by a silicon solar cell where the range between excitation and emission is

comparatively narrow. Furthermore, cascade energy transfer was demonstrated by sequentially omitting each of the intermediary jumper dyes. Emission from the terminal acceptor was significantly reduced if a single dye was omitted. These findings could enhance our understanding of light harvesting and lay the groundwork for enhanced power output from silicon solar cells. For example, silicon cells can be coated with an antenna complex for the enhancement of light harvesting.

The matrix was carefully chosen in this system to be low coast, biodegradable, and possess binding pockets for a wide variety of dyes. The role of each matrix component was demonstrated by exclusion of each component from the antenna system. No emission was observed from dyes self-assembled on DNA alone (**Figure 4A**). However, to our surprise, emission was observed from a BSA/4 dyes system, indicating that BSA has the appropriate number of binding pockets required to accommodate the four dyes in the required Forster radius. BSA and DNA together, increase the number and variety of chromophores that can potentially drive light harvesting.

In order to develop an antenna system suitable for solar cell applications, long-term photostability is of utmost importance. As a result the photostability of our antenna systems were tested by exposure to white light (**Figure 7**). Comparison of normalized emission intensity before and after exposure to white light revealed that the antenna photostability was highly dependent on the photostability of the terminal acceptor, rhodamine B. Most antennas analyzed showed stabilized or a slight increase in emission intensity at the emission maxima of the primary donor dye, Hoechst and each of the intermediate dyes, coumarin and fluorescein. This suggests that the increased number of photons shuttled to the terminal acceptor induced degradation. The half-life observed for most antennas was within 48 h, therefore much

improvement is needed. A non-emitting acceptor that can be coupled to rhodamine B emission would probably accept enough electrons from rhodamine B that the terminal acceptor is not overwhelmed by the cascade effect. Materials like TiO_2 with band gaps compatible with rhodamine B would be optimal for "draining" the terminal acceptor during the operation and functioning of the antenna. This "draining" effect should increase antenna half-life to the point where the terminal acceptor emission, like the other three dyes, stabilizes over time.

3.6. Conclusion

Antenna systems possessing biodegradable matrices that provide scaffolding for cascade energy transfer among four dyes were developed here. While BSA/DNA, BSA alone, glucose, and sucrose were excellent scaffolds for the self-assembly of highly efficient antennas, no emission was observed from antennas self-assembled using DNA alone, PASC, or CMC. This emphasizes the importance of the appropriate Forster radii, dye concentrations, and scaffolding/dye affinity. Although a 2.4 fold photon gain was calculated and the terminal acceptor emits at optimal wavelength to catalyze solar cells, antenna half-life was within 48 h. This rapid degradation was investigated by analysis of emission at each dye's peak maximum before and after exposure to white light. The terminal acceptor was found to be the most vulnerable as it degraded rapidly over the 48 h time period while the donor and intermediate dyes either stabilized or increased slightly. Future studies that address this problem may include a non-emitting acceptor in the antenna self-assembly. The ideal material will accept electrons from the terminal acceptor, thus delaying degradation and increasing half-life.

3.7. References

(1) Lewis, N. S., Toward cost-effective solar energy use. *Science,* **2007**, 315, 798-801.

(2) Lewis, N. S.; Nocera, D. G., Powering the planet: Chemical challenges in solar energy utilization. *Proc. Natl. Acad. Sci. USA.*, **2006**, 103, 15729-15735.

(3) McDermott, G.; Prince, S.; Freer, A., Hawathornthwaite-Lawless, A. M.; Papiz, R. J.; N. Isaacs, W., Crystal structure of an integral membrane light-harvesting complex from photosynthetic bacteria. *Nature*, **1995**, 374, 517–521.

(4) Odobel, F.; Pellegrim, Y.; Warnan, J., Bio-inspired artificial light-harvesting antennas for enhancement of solar energy capture in dye-sensitized solar cells. *Energy Environ. Sci.*, **2013**, 6, 2041-2052.

(5) Strumpel, C.; McCann, M.; Beaucarne, G.; Arkhipov, V.; Slaoui, A.; Svrcek, V.; del Canizo, C. D.; Tobias, I., Modifying the solar spectrum to enhance silicon solar cell efficiency—An overview of available materials. *Sol. Energy Mater. and Solar Cells*, **2007**, 91, 238-249.

(6) Turro, N. J. *Modern Molecular Photochemistry*, Benjamin/Cummings: Menlo Park. CA. **1978**, pp 296.

(7) Andersson, L. O.; Rehnström, A.; Eaker, D. L., *Eur. J. Biochem.*, **1971**, 20, 371-380.

(8) Prasad, S.; Ibnaouf, K. H.; AlSalhi, M. S.; Masilamani, V., Laser from the dimer state of a conjugated polymer (PFO) in solution. *Polymer*, **2014**, 55, 727-732.

(9) Posokhov, Y. O.; Merzlyakov, M.; Hristova, K.; Ladokhin, A. S., A simple "proximity" correction for Förster resonance energy transfer efficiency determination in membranes using lifetime measurements. *Anal. Biochem.*, **2008**, 380, 134–136.

(10) Johansson, E.; Choi, E.; Angelos, S.; Liong, M.; Zink, J. I., Light-activated functional mesostructured silica. *J. Sol-Gel. Sci. Tech*. **2008**, 46, 313–322.

(11) Kumar, C. V.; Duff, M. R., Towards building artificial light harvesting complexes: enhanced singlet–singlet energy transfer between donor and acceptor pairs bound to albumins. *J. Photoch. Photobio. Sci*., **2008**, 7, 1522-30.

(12) Pjura, P. E.; Grzeskowiak, K.; Dickerson, R. E., Binding of Hoechst 33258 to the minor groove of B-DNA. *J.Mol.Biol*, **1987**, 197, 257-271.

(13) Kumar, C. V.; Chaudhari, A.; Rosenthal, G. L., Enhanced energy transfer between aromatic chromophores bound to hydrophobically modified layered zirconium phosphate suspensions. J. Am. Chem. Soc. **1994**, 116, 403-404.

(14) Miller, R. A.; Presley, A. D.; Francis, M. B., Self-assembling light-harvesting systems from synthetically modified tobacco mosaic virus coat proteins., *J. Am. Chem. Soc*., **2007**, 129, 3104–3109.

(15) Dutta, P. K.; Varghese, R.; Nangreave, J.; Lin, S.; Yan, H.; Liu, Y., DNA-directed artificial light-harvesting antenna. J. Am. Chem. Soc., **2011**, 133, 11985–11993.

(16) Woller, J. G.; Hannestad, J. K.; Albinsson, B., Self-assembled nanoscale DNA–porphyrin complex for artificial light harvesting. *J. Am. Chem. Soc.*, **2013**, 135, 2759-2768.

(17) Kumar, C. V.; Duff, M. R., DNA-based supramolecular artificial light harvesting complexes. *J. Am. Chem. Soc*., **2009**, 131, 16024-16026.

(18) Stein, I. H.; Steinhauer, C.; Tinnefeld, P., Single-molecule four-color FRET visualizes energy-transfer paths on DNA origami. *J. Am. Chem. Soc*. **2011**, 133, 4193–4195.

(19) Spillmann, C. M.; Ancona, M. G.; Buckhout-White, S.; Algar, W. R.; Stewart, M. H.; Susumu, K.; Huston, A. L.; Ellen.; Goldman, R.; Medintz, I. L. Achieving effective terminal exciton delivery in quantum dot antenna-sensitized multistep DNA photonic wires *ACS Nano*, **2013**, 7, 7101-7118.

(20) Massey, M.; Ancona, M. G.; Medintz, I. L.; Algar, W. R., Time-Gated DNA Photonic Wires with Förster Resonance Energy Transfer Cascades Initiated by a Luminescent Terbium Donor. *ACS Photonics*, **2015**, 2, 639-652.

Chapter 4: Biodegradable Exfoliation of Zirconium Phosphate with Proteins for Potential Biomedical Applications

4.1. Abstract

Biodegradable exfoliation of zirconium phosphate (α-$Zr(HPO_4)_2$) is reported here. Bovine serum albumin (BSA) was used to exfoliate α-$Zr(HPO_4)_2$ (α-ZrP) and the exfoliation was more than 80% complete in 100 mins as characterized by Xray diffraction (XRD). Exfoliation was carried out in water, at room temperature by shear force using a homogenizer at a 12000 rpm. The reduction in intensity of XRD d spacing peak of 7.5 Å that characterizes unexfoliated α-ZrP was used to estimate the degree of exfoliation. Other proteins, including lysozyme, β-lactoglobulin, ovalbumin, and hemoglobin also exfoliated α-ZrP, with the highest degree of exfoliation observed using ovalbumin. When compared to the typical chemical exfoliation of α-ZrP using tetrabutylammonium hydroxide (TBA), the proteins used in this study exfoliated to a larger extent. To the best of our knowledge, this is the first biodegradable exfoliation of α-ZrP with potential applications in the biomedical device and drug delivery industries.

4.2. Introduction

Alpha zirconium phosphate (α-$Zr(HPO_4)_2$) has been prepared for a wide variety of applications. Chemical separation of the stacked layers (exfoliation) has been carried out using butylamine hydrochloride.[1,2] A more typical approach has been to exfoliate α-$Zr(HPO_4)_2$ (α-ZrP) with tetra-n-butylammonium hydroxide (TBA) for various studies including enzyme stabilization,[3] the role of solvent ions in protein-solid interactions,[4] and the thermodynamics of protein-solid interactions.[5] Furthermore, the mechanisms of amine intercalation into α-ZrP have

been elucidated by variation of its crystallinity[6] and aspect ratio.[7] Additionally, the use of α-ZrP in biomedical applications as a solid for immobilization of enzymes has led to the development of glucose sensors[8] and drug delivery.[9]

Protein intercalation into the galleries of α-ZrP after TBA exfoliation presents a promising platform for biomedical applications. Mechanisms of TBA exfoliation have been investigated,[10] and mechanisms of protein binding α-ZrP following TBA exfoliation have been proposed.[11] These studies support the idea of α-ZrP as a biological matrix for drug delivery, gene delivery, biosensing, biofuel cells, and other biomedical devices. In fact, ZrP has been incorporated as a key component of biofuel cells,[12,13] and α-ZrP as a drug delivery vehicle has been reported.[14,15] However, a non-toxic, biodegradable method for the exfoliation of α-ZrP, an important step towards the intercalation of drugs, has not been investigated.

Previously, BSA has been used to exfoliate layered materials,[16,17] therefore we hypothesized that charge-charge repulsion between the negatively charged BSA surface[18] and the α-ZrP phosphate backbone should drive exfoliation when combined with the interlayer stress induced by shearing. In this work, we show that bovine serum albumin (BSA) exfoliates α-ZrP in the absence of TBA (**Scheme 1**). We use shearing forces induced by a homogenizer, together with BSA to physically separate the stacked α-ZrP plates. BSA binding ensures that α-ZrP

Scheme 4.1. Exfoliation of α-ZrP (gray stack) is achieved by shearing a solution of 20 mg/mL α-ZrP and 3 mg/mL BSA in DI water at 12000 rpm for at least 20 mins, pausing every 10 mins to ensure maintenance of room temperature. A homogenizer is used for shearing in a total volume of at least 15 mLs in a 50 mL tube. The mixture is allowed to precipitate overnight and an aliquot of the supernatant containing the exfoliated α-ZrP nanosheets (gray squares) is dropcast unto a glass slide and allowed to dry overnight. Characterization using XRD determines the degree of crystallinity and the distance between layers. Stacked XRD has a characteristic peak at $2\theta = 11.8$ which, by using Bragg's law, is equivalent to a distance of 7.5 Å between layers. After 100 mins of exfoliation this peak intensity decreases significantly, indicating the increased interlayer distance that results from exfoliation.

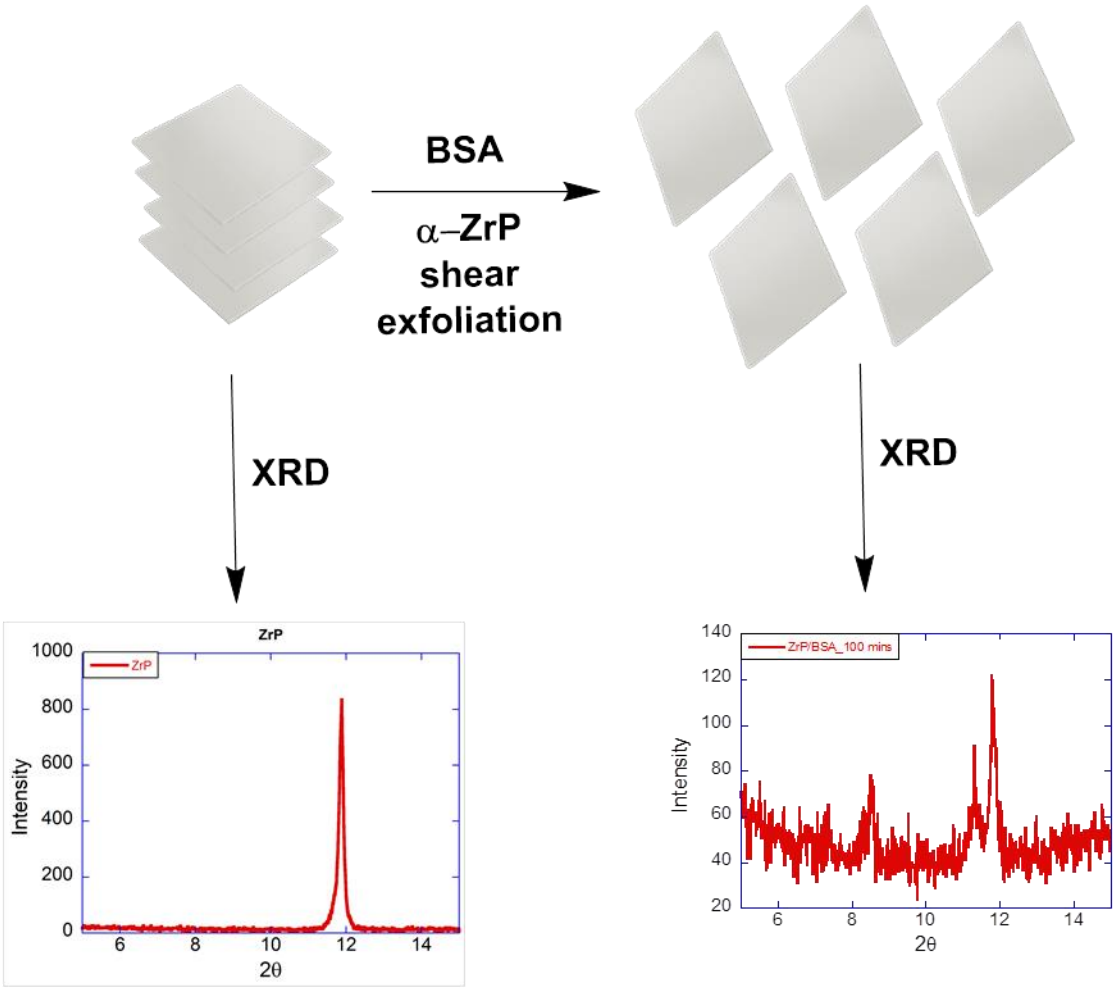
BSA
α–ZrP
shear
exfoliation
XRD
XRD
ZrP
ZrP
Intensity
2θ
ZrP/BSA_100 mins
Intensity
2θ

remains exfoliated and provides binding pockets that can potentially enhance immobilization of a wide variety of drugs on the α-ZrP surface. Xray diffraction (XRD) data was used to characterize the increase in interlayer distance due to exfoliation from 7.5 Å that is the known spacing for stacked unexfoliated α-ZrP.[3] Disappearance of the 7.5 Å XRD peak was used as a benchmark for characterizing exfoliation and increased exfoliation was observed using the shearing BSA method when compared to chemical exfoliation with TBA. To our knowledge, this is the first report of protein exfoliation of α-ZrP without the use of toxic chemicals and this presents a promising solution to α-ZrP as a biomedical matrix for drug delivery and biofuel cells.

4.3. Materials and Methods

4.3.1. ***Materials:*** BSA and hemoglobin were purchased from Equitech-Bio Inc. (Kerrville, TX). Glucose oxidase, ovalbumin, lysozyme, and β-Lactoglobulin were purchased from Sigma-Aldrich (St. Louis, MO). All proteins were used without further purification.

4.3.2. ***Synthesis of α-ZrP:*** The synthesis was carried out by following a method reported previously.[19] Briefly, 9 M phosphoric acid was heated to 90 ºC, and a solution of 10.1 g of $ZrOCl_2$ (0.031 mol, 10 mL of water) was added over a period of 1 h and allowed to reflux for 24 h. The reaction mixture was filtered, washed with water to remove excess acid, and then washed with acetone. The solid was dried at 60 ºC overnight and characterized by powder X-ray diffraction (XRD) which matched with the literature report.

4.3.3. ***Exfoliation of α-ZrP:*** Exfoliation experiments were carried out by shearing 20 mg/mL α-ZrP and 3 mg/mL BSA in DI in a 50 mL tube using a homogenizer. Shearing was paused every 10 mins to maintain room temperature in the sample tube. Aliquots of the sample were taken every 10 mins to monitor the progress of exfoliation. Samples were refrigerated at 4°C overnight

to precipitate unexfoliated α-ZrP. A 300 μL aliquot of the supernatant was dropcast on a 22 mm x 22 mm cover slip and dried overnight under a fume hood. XRD analysis of the dropcasted sample was used to estimate the degree of α-ZrP exfoliation.

4.3.4. ***XRD Analysis:*** A Scintag model 2000 diffractometer with nickel filtered Cukr radiation was used for analysis of samples dropcasted on 22 mm x 22 mm cover slips. The scan range was $2\theta = 5° - 15°$ at a scan rate of 2°/min. Bragg's equation was used to calculate the d spacing.

4.4. Results

A rapid low cost method for the exfoliation of α-ZrP using proteins is described here. TBA has been used extensively to chemically exfoliate α-ZrP. However. α-ZrP has been explored as a drug delivery vehicle and an integral component of biomedical devices. Therefore there is great need for a biodegradable method to exfoliate α-ZrP. We systematically examined the effect of exfoliation shear time, total volume, protein concentration, and protein type on the degree of α-ZrP exfoliation.

Exfoliation of 20 mg/mL α-ZrP (DI water) in a 3 mg/mL protein solution (DI water) was carried out using shear force by a homogenizer at 12000 rpm. Shearing was paused for five minutes every fifteen minutes to maintain room temperature and avoid overheating. Samples were refrigerated at 4°C overnight to allow unexfoliated α-ZrP to precipitate. An aliquot of the exfoliated α-ZrP in solution was dropcast on a glass slide and allowed to dry overnight under a fume hood. The degree of exfoliation was characterized by XRD.

4.4.1. ***Effect of Exfoliation Shear Time****:* In order to optimize the total shear time required to exfoliate α-ZrP, a BSA/α-ZrP suspension was sheared for a total time of 100 mins, removing an aliquot for XRD analysis every 10 mins. The XRD peak intensity at a d spacing of 7.5 Å that characterizes unexfoliated α-ZrP was used to estimate the degree of exfoliation

Of note is that this method of estimating exfoliation is very preliminary. Internal standards like unexfoliated α-ZrP and MoS_2 are currently being tested. These will be added to the sample at a fixed concentration prior to dropcast and the resulting peak intensity will be used to normalize the reduced intensity of the unexfoliated α-ZrP peak.

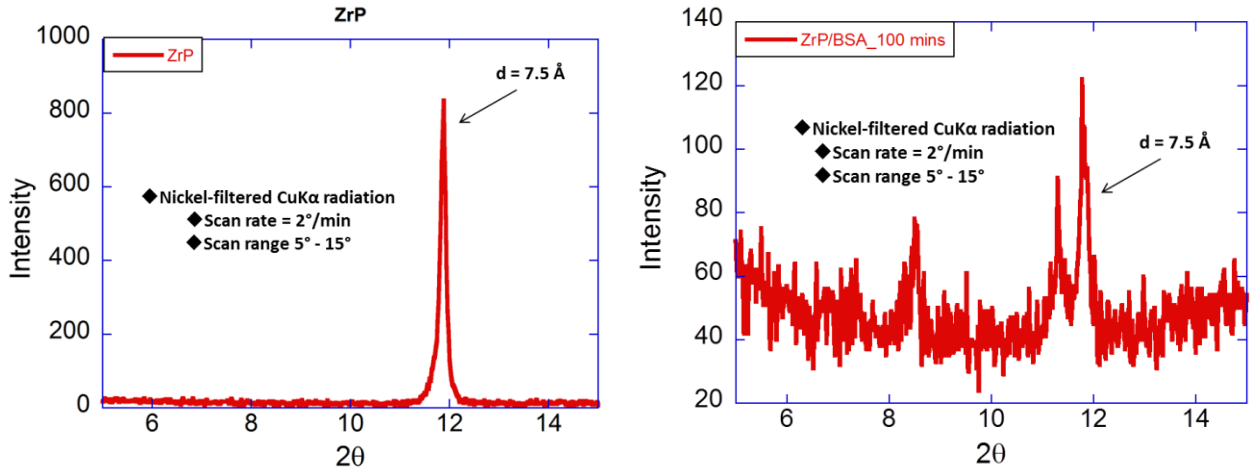

Figure 4.1. XRD characterization of α-ZrP exfoliation. (A) The characteristic peak for stacked α-ZrP is observed at 2θ = 11.8 and conversion by Bragg's equation yields in interlayer spacing (d) of 7.5 Å. The scan range is 5° - 15° at a scan rate of 2°/min using Ni-filtered Cukα radiation. (B) The conditions described in (A) are used to scan an exfoliated sample and the reduced 7.5 Å peak intensity is characteristic of increased interlayer distance due to exfoliation.

At the 60 mins time point, exfoliation had progressed significantly when compared to an unexfoliated sample (**Figure 1A**) and continued shearing beyond 60 mins increased the degree of exfoliation. In fact, at the 100 mins time point (**Figure 1B**) background noise becomes very dominant as the 7.5 Å peak approaches baseline. Exfoliation shear time was therefore optimized at a minimum of 100 mins.

4.4.2. ***Effect of exfoliation volume***: Sample volume may affect shear forces and the energy levels implicated in separating the α-ZrP nanosheets. At a fixed exfoliation time of 20 mins, a 5 mLs (**Figure 2A**) sample volume was compared to a 20 mLs sample volume (**Figure 2B**), revealing that exfoliation progressed further when the volume was 20 mLs. This suggests that the forces dissipated through the larger volume are of optimal magnitude to lower the free energy barrier of α-ZrP nanosheet separation.

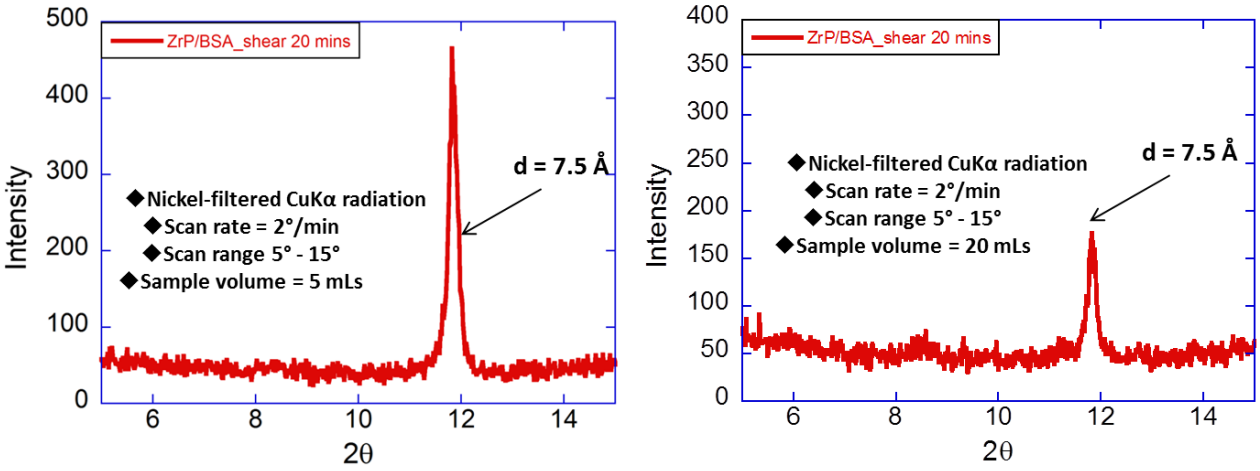

A **B**

Figure 4.2. Effect of sample volume on shear exfoliation of α-ZrP. (A) When temperature, shear time, and speed are held constant a lower degree of exfoliation, as characterized by the characteristic 7.5 Å peak intensity, is observed in a total volume of 5 mLs when compared to (B), a total volume of 20 mLs.

4.4.3. ***Effect of Protein Concentration***: Next we investigated the role of BSA concentration on α-ZrP exfoliation. We hypothesized that the degree of exfoliation should increase with increasing protein concentration given that increased d spacing between the layers is required for exfoliation. Therefore, the increased concentration of protein per unit area of α-ZrP should increase layer separation. With exfoliation time fixed at 20 mins, analysis of the effect of increased BSA concentration on the degree of exfoliation yielded an optimal BSA concentration of 5 mg/mL. BSA concentration was increased over the range from 0.5 mg/mL to 15 mg/mL and BSA percent bound was estimated by measuring its absorbance at 280 nm before exfoliation when compared to absorbance of BSA in solution after shearing and overnight precipitation (**Figure 3A**). The BSA extinction coefficient used to calculate percent bound was 43,824 M^{-1} cm^{-1}. This method assumes that the protein associates exclusively with the exfoliated α-ZrP in solution (supernatant) after precipitation such that the difference in BSA concentration in solution before and after exfoliation was used to calculate percent BSA bound.

The degree of exfoliation was also estimated using XRD by determining the 7.5 Å peak intensity after exfoliation with each of the differentially concentrated BSA suspensions. This analysis suggested increased exfoliation over the range of 3 mg/mL to 15 mg/mL (**Figure 3B**). Minimal exfoliation was observed with 1 mg/mL or 2 mg/mL BSA but 0.5 mg/mL BSA exfoliated to approximately the same degree as 10 mg/mL. However, without an internal standard to normalize peak intensity these findings are very preliminary and the use of an internal standard in the future will clarify these observations.

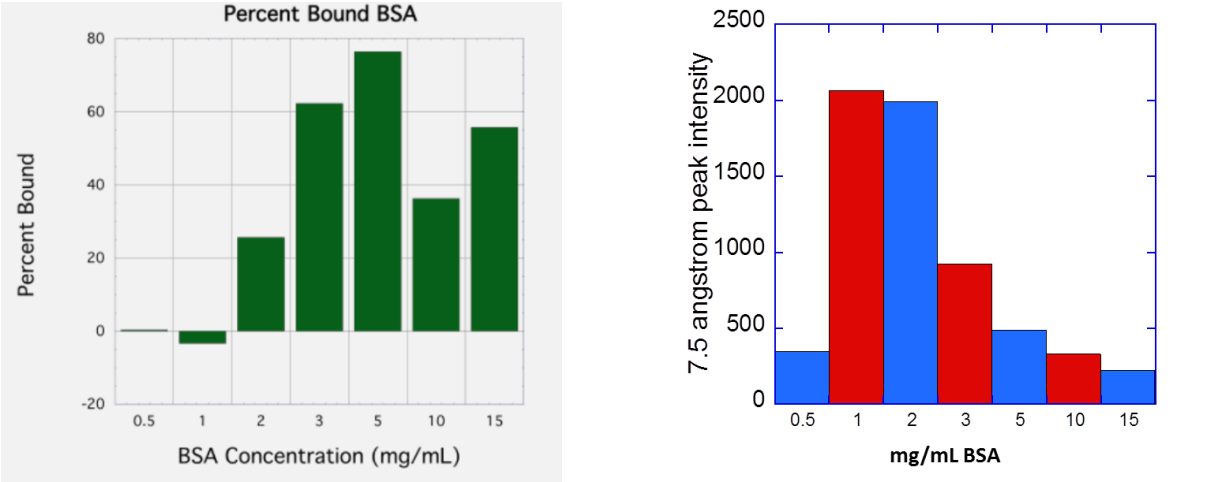

A **B**

Figure 4.3. Effect of BSA concentration on α-ZrP exfoliation. (A) Percent BSA bound to the α-ZrP surface was used to estimate the degree of exfoliation assuming that BSA bound to the exfoliated nanosheets remained in solution after overnight precipitation. BSA absorbance was estimated using a UV/Vis spectrometer at $\lambda = 280$ nm and extinction coefficient = 43,824 M^{-1} cm^{-1}. The difference in BSA concentration in solution, due to variation of mg/mL BSA (green bars) used to exfoliate, before and after exfoliation and overnight precipitation was used to calculate percent BSA bound to α-ZrP. (B) A second method to estimate the degree of exfoliation was by comparing intensities of the characteristic XRD peak at 7.5 Å due to variation of the BSA concentration used to exfoliate (red and blue bars) α-ZrP assuming that reduction in peak intensity was correlative with the degree of exfoliation.

4.4.4. ***Effect of Protein Type***: When speed of rotation, temperature, pH, volume, protein concentration of 3 mg/mL, and shear time of 20 mins were held constant the effect of protein type on the degree of exfoliation was analyzed using ovalbumin (Oval), glucose oxidase (GOx), β-Lactoglobulin (b Lact), BSA, hemoglobin (Hb), and lysozyme (Lys). Analysis of the XRD peak intensity at 7.5 Å revealed that ovalbumin exfoliated α-ZrP to the highest degree (**Figure 4A**), followed by GOx. In fact, ovalbumin exfoliated more than twice as much α-ZrP as either b Lact, BSA, or Hb, and six times as much as Lys. Preliminarily, there appears to be a correlation between protein Isoelectric point (pI) and the degree of α-ZrP exfoliation (**Figure 4B**) suggesting the importance of protein surface charge on layer separation. These findings will be explored in further detail using an internal standard that normalizes peak intensity.

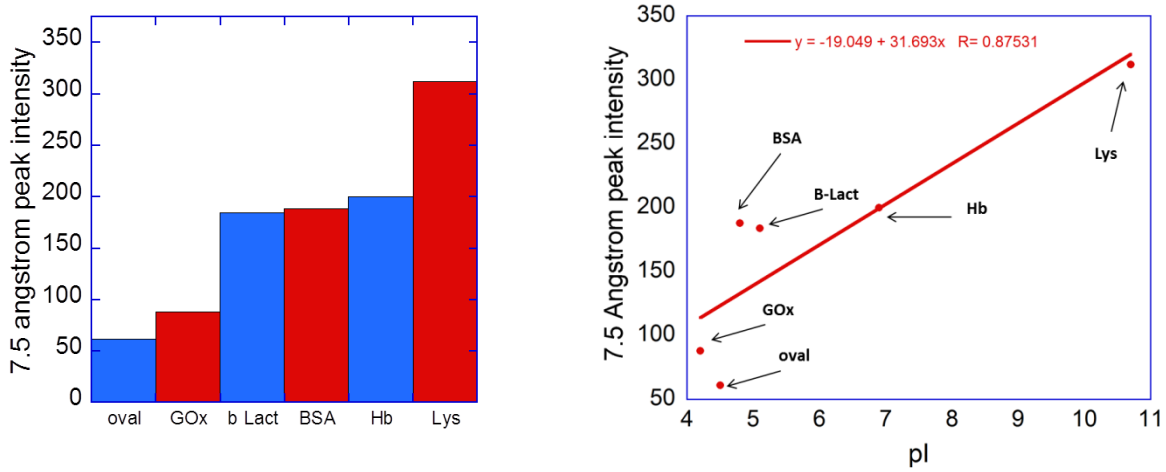

A **B**

Figure 4.4. Effect of variation of protein type on α-ZrP exfoliation. Proteins used in this study were ovalbumin (oval), glucose oxidase (GOx), β-Lactoglobulin (b Lact), bovine serum albumin (BSA), hemoglobin (Hb), and lysozyme (Lys). (A) Using the reduced intensity of the 7.5 Å peak as an indicator of increased degree of exfoliation, ovalbumin exfoliated α-ZrP to the highest degree and lysozyme the least. (B) Preliminary results suggest a correlation between the degree of exfoliation and the isoelectric point (pI) of the protein yielding an R value of 0.87531.

4.5. Discussion

The biodegradable exfoliation of α-ZrP using proteins was preliminarily demonstrated here. These findings present a promising alternative to chemical exfoliation using TBA and other harsh compounds. The findings here, suggest potentially promising applications for α-ZrP in biomedicine in the fields of drug delivery and biomedical devices.

The total shear time influenced the degree of exfoliation as evidenced by the overall increase in exfoliation as shear time increased. It is conceivable that as shear time is extended a larger concentration of protein per unit area of α-ZrP occupies the inter layer space, and this in turn, increases the forces exerted on the layers to drive them apart. Also, increased shear time allows for an increase in the sum magnitude of the interlayer forces, thus increasing the irreversible layer separation required for complete exfoliation. However, it may become increasingly difficult to maintain a given temperature as shear time increases such that the introduction of an ice bath may be required. Also, protein structure may be difficult to retain at extended shear times. These problems will be investigated in the future but these preliminary experiments indicate almost complete (approximately 80%) exfoliation in 100 mins. Furthermore, α-ZrP was exfoliated to higher degree when compared to chemical exfoliation using TBA.

Exfoliation volume played a key role in the optimization of this method. Although a wider range of volumes should be tested in the future, the two volumes tested here (5 mLs and 20 mLs) indicate that the shear forces required for α-ZrP layer separation are optimal at 20 mLs. Optimization of volume is probably based on homogenizer probe diameter, probe length, rotational speed, and size and shape of the container. These are all factors that affect the

protein/α-ZrP interactions that influence the forces exerted by the protein between layers to force them apart.

The degree of exfoliation increased with increasing protein concentration. An optimal concentration for exfoliation in the range of 3 mg/mL to 15 mg/mL BSA was observed, with 5 mg/mL being optimal if the degree of exfoliation was calculated based on percent protein bound. When the degree of exfoliation was estimated based on the reduced intensity of the characteristic 7.5 Å peak, 15 mg/mL BSA was found to be optimal. This discrepancy could be due to the assumption that the percent protein bound is equivalent to the protein used in solution for exfoliation during shearing. However, some protein may precipitate with the unexfoliated α-ZrP overnight and the absorbance of protein bound to α-ZrP may be distorted by the presence of α-ZrP. Furthermore, the protein used for exfoliation may be bound or free in solution and these factors could complicate an accurate calculation of the degree of α-ZrP exfoliation. Future studies that explore and address these discrepancies will improve our understanding of exfoliation efficiency and the factors implicated in efficiency calculations.

4.6. Conclusion

Zirconium phosphate is one of several layered materials currently being explored for their applications as key components of drug delivery and enzyme immobilization devices. However, current methods that rely on the chemical exfoliation of α-ZrP are not biocompatible. This work demonstrates biodegradable exfoliation of α-ZrP using proteins. In fact, the degree of exfoliation achieved here is higher than the degree of exfoliation observed as a result of chemical exfoliation. Future work will explore the use of an internal standard to normalize the XRD data used here to characterize the degree of exfoliation. Also, calculation of exfoliation efficiency and

supporting characterization techniques like transmission electron microscopy (TEM), scanning electron microscopy (SEM), and zeta potential will add clarity to these findings.

4.7. References

(1) Kumar, C. V.; Asuncion, E. H.; Rosenthall, G., Static pyrene excimer formation at hydrophobic zirconium phosphate surfaces: The salt effect. *Microporous Mater.* **1993,** *1*, 299-308.

(2) Kumar, C.; Chaudhari, A.; Rosenthal, G., Enhanced energy transfer between aromatic chromophores bound to hydrophobically modified layered zirconium phosphate suspensions. *J. Am. Chem. Soc.* **1994,** *116*, 403-404.

(3) Kumar, C.; Chaudhari, A., High temperature peroxidase activities of HRP and hemoglobin in the galleries of layered Zr (IV) phosphate. *Chem. Commun.* **2002,** 20, 2382-2383.

(4) Duff Jr, M. R.; Kumar, C. V. Protein-Solid Interactions: Important Role of Solvent, Ions, Temperature, and Buffer in Protein Binding to α-Zr(IV) Phosphate. *Langmuir* **2009**, 25, 12635-12643.

(5) Duff Jr, M. R.; Kumar, C. V., Molecular Signatures of Enzyme-Solid Interactions: Thermodynamics of Protein Binding to α-Zr(IV) Phosphate Nanoplates. *The Journal of Physical Chemistry B* **2009,** *113*, 15083-15089.

(6) Sun, L.; Boo, W. J.; Browning, R. L.; Sue, H.-J.; Clearfield, A., Effect of crystallinity on the intercalation of monoamine in α-zirconium phosphate layer structure. *Chem. Mater.* **2005,** *17*, 5606-5609.

(7) Sun, L.; Boo, W. J.; Sun, D.; Clearfield, A.; Sue, H.-J., Preparation of exfoliated epoxy/α-zirconium phosphate nanocomposites containing high aspect ratio nanoplatelets. *Chem. Mater.* **2007,** *19*, 1749-1754.

(8) Liu, L.-M.; Wen , J.; Liu, L.; He, D.; Kuang, R.-y.; Shi, T., A mediator-free glucose biosensor based on glucose oxidase/chitosan/α-zirconium phosphate ternary biocomposite. *Anal. Biochem.* **2014,** *445*, 24-29.

(9) Kalita, H.; Kumar, B. P.; Konar, S.; Tantubay, S.; Mahto, M. K.; Mandal, M.; Pathak, A., Sonochemically synthesized biocompatible zirconium phosphate nanoparticles for pH sensitive drug delivery application. *Mater. Sci. Eng., C* **2016,** *60*, 84-91.

(10) Kaschak, D. M.; Johnson, S. A.; Hooks, D. E.; Kim, H.-N.; Ward, M. D.; Mallouk, T. E., Chemistry on the edge: A microscopic analysis of the intercalation, exfoliation, edge functionalization, and monolayer surface tiling reactions of α-zirconium phosphate. *J. Am. Chem. Soc.* **1998,** *120*, 10887-10894.

(11) Kumar, C. V.; McLendon, G. L., Nanoencapsulation of cytochrome c and horseradish peroxidase at the galleries of α-zirconium phosphate. *Chem. Mater.* **1997,** *9*, 863-870.

(12) Malinauskas, A.; Ruzgas, T.; Gorton, L., Electrocatalytic oxidation of coenzyme NADH at carbon paste electrodes, modified with zirconium phosphate and some redox mediators. *J. Colloid Interface Sci.* **2000,** *224*, 325-332.

(13) Munteanu, F. D.; Kubota, L. T.; Gorton, L., Effect of pH on the catalytic electrooxidation of NADH using different two-electron mediators immobilised on zirconium phosphate. *J. Electroanal. Chem.* **2001,** *509*, 2-10.

(14) Díaz, A.; David, A.; Pérez, R.; González, M. L.; Báez, A.; Wark, S. E.; Zhang, P.; Clearfield, A.; Colón, J. L., Nanoencapsulation of insulin into zirconium phosphate for oral delivery applications. *Biomacromolecules* **2010,** *11*, 2465-2470.

(15) Díaz, A.; Saxena, V.; González, J.; David, A.; Casañas, B.; Carpenter, C.; Batteas, J. D.; Colón, J. L.; Clearfield, A.; Hussain, M. D., Zirconium phosphate nano-platelets: a novel platform for drug delivery in cancer therapy. *Chem. Commun*. **2012,** *48* , 1754-1756.

(16) Pattammattel, A.; Kumar, C. V., Kitchen chemistry 101: Multigram production of high quality biographene in a blender with edible proteins. *Adv. Funct. Mater*. **2015,** *25* , 7088-7098.

(17) Guan, G.; Zhang, S.; Liu, S.; Cai, Y.; Low, M.; Teng, C. P.; Phang, I. Y.; Cheng, Y.; Duei, K. L.; Srinivasan, B. M., Protein induces layer-by-layer exfoliation of transition metal dichalcogenides. *J. Am. Chem. Soc*. **2015,** *137*, 6152-6155.

(18) van Eijndhoven, R. H.; Saksena, S.; Zydney, A. L., Protein fractionation using electrostatic interactions in membranel filtration. *Biotechnol. Bioeng*. **1995,** *48*, 406-414.

(19) Clearfield, A.; Stynes, J. A. The preparation of crystalline zirconium phosphate and some observations on its ion exchange behaviour. *J. Inorg. Nucl. Chem.* **1964**, 26, 117-129.